
Doctoral Dissertations

Student Theses and Dissertations

Fall 2021

Semi-empirical modeling of liquid carbon's containerless solidification

Philip C. Chrostoski

Follow this and additional works at: https://scholarsmine.mst.edu/doctoral_dissertations



Part of the [Materials Science and Engineering Commons](#), and the [Physics Commons](#)

Department: Physics

Recommended Citation

Chrostoski, Philip C., "Semi-empirical modeling of liquid carbon's containerless solidification" (2021).
Doctoral Dissertations. 3051.

https://scholarsmine.mst.edu/doctoral_dissertations/3051

This thesis is brought to you by Scholars' Mine, a service of the Missouri S&T Library and Learning Resources. This work is protected by U. S. Copyright Law. Unauthorized use including reproduction for redistribution requires the permission of the copyright holder. For more information, please contact scholarsmine@mst.edu.

SEMI-EMPIRICAL MODELING OF LIQUID CARBON'S CONTAINERLESS
SOLIDIFICATION

by

PHILIP C. CHROSTOSKI

A DISSERTATION

Presented to the Faculty of the Graduate School of the
MISSOURI UNIVERSITY OF SCIENCE AND TECHNOLOGY

AND

UNIVERSITY OF MISSOURI – ST. LOUIS

In Partial Fulfillment of the Requirements for the Degree

DOCTOR OF PHILOSOPHY

in

PHYSICS

2021

Approved by:

Philip Fraundorf, Advisor
Julia E. Medvedeva, Co-Advisor
Eric H. Majzoub
Deborah H. Santamore
Alexey Yamilov

© 2021

Philip C. Chrostoski

All Rights Reserved

PUBLICATION DISSERTATION OPTION

A portion of this dissertation has been prepared in publication format. The formatting of these sections will follow that of this dissertation. The overall text has not been changed from the original publication. References cited in these publications will appear at the end of these sections. Paper I has been published in a scientific journal.

Paper I, Pages: 55-67, “The Rates of Unlayered Graphene Formation in a Supercooled Carbon Melt at Low Pressure”, P. Chrostoski, C. Silva, P. Fraundorf, *MRS Advances* **2021**, 6, 713-717.

ABSTRACT

Elemental carbon has important structural diversity, ranging from nanotubes through graphite to diamond. Previous studies of micron-size core/rim carbon spheres extracted from primitive meteorites suggest they formed around such stars via the solidification of condensed carbon-vapor droplets, followed by gas-to-solid carbon coating to form the graphite rims. Similar core/rim particles result from the slow cooling of carbon vapor in the lab. The long-range carbon bond-order potential was used to computationally study liquid-like carbon in (1.8 g/cm^3) periodic boundary (tiled-cube supercell) and containerless (isolated cluster) settings. Relaxations via conjugate-gradient and simulated-annealing nucleation and growth simulations using molecular dynamics were done to study nucleation seed formation, structural coordination, and the latent heat of fusion. Atomistic results, which agree with independent DFT studies, show an energy preference for pentagon nucleation seeds, sp and sp² coordination, and a bond defining gap in nearest neighbor histograms. Latent heat of fusion values of $1.015 \pm 0.078 \text{ eV/atom}$ ($1.178 \pm 0.053 \text{ eV/atom}$ at fixed pressure) were determined which agree with values previously determined by separate experimental and computational studies. Analytical models of nucleation and growth derived from classical nucleation theory links the onset of solidification to the interface/bulk energy ratio, predict cluster size distributions, and suggest a role for saturation during slow (e.g. stellar atmosphere) cooling. The low-pressure analytical model predictions for graphene sheet density and mass weighted average are supported by experimental observations of pre-solar and lab-grown specimens.

ACKNOWLEDGMENTS

I would first like to thank my undergraduate professors and graduate professors for their teachings and advise during my many years of schooling. Without the great background obtained from SIU-E and DSU, I would not have the insight and intuition that I do today. I also want to thank Missouri S&T and UMSL for allowing me to finish my doctoral studies in their prestigious physics program and for access to The Foundry supercomputer to conduct the complex simulations.

I would like to give a big thank you, and acknowledgement to both my Master and Doctoral research advisers, Dr. Deborah Santamore and Dr. Philip Fraundorf. The work done under the mentorship of both advisors has given me amazing inspiration and motivation to continue to grow and learn as a physicist. I know the work done and skill gained while working with each of them will help me become a prominent member of the physics community. I also would like to thank the rest of my doctoral committee Dr. Eric Majzoub, Dr. Julia E. Medvedeva, and Dr. Alexey Yamilov for taking the time to be a part of my committee and the helpful advice and scientific insights.

I would also like to thank the Missouri NASA Space Grant Consortium for funding a large portion of this work. I cannot go without thanking my research colleagues during my graduate school career for their stimulating conversations. I last want to thank my friends, family, in-laws, and especially my loving wife for their ongoing support during my studies in graduate school.

TABLE OF CONTENTS

	Page
PUBLICATION DISSERTATION OPTION.....	iii
ABSTRACT.....	iv
ACKNOWLEDGMENTS	v
LIST OF ILLUSTRATIONS.....	x
LIST OF TABLES	xii
 SECTION	
1. INTRODUCTION	1
1.1. INTEREST IN ELEMENTAL CARBON.....	1
1.2. CARBON ALLOTROPES.....	2
1.3. PRESOLAR GRAINS.....	10
1.4. NUCLEATION AND SOLIDIFICATION.....	14
1.4.1. Nucleation.....	14
1.4.2. Solidification.....	16
1.5. SEMI-EMPIRICAL INTERATOMIC POTENTIALS.....	17
1.5.1. Interatomic Potentials.....	18
1.5.2. Tersoff Potential for Carbon.....	20
1.6. MOLECULAR DYNAMICS.....	24
1.6.1. Microcanonical Ensemble.....	25
1.6.2. Canonical Ensemble.....	25

1.6.3. Isothermal-Isobaric Ensemble.....	26
1.6.4. Generalized Ensemble.....	26
1.6.5. Molecular Dynamics Applications.....	27
1.7. OUTLINE OF WORK.....	27
2. TILED-CUBE ZERO KELVIN LOOP COUNTING AND COORDINATION STATISTICS	29
2.1. TILED-CUBE MODEL.....	29
2.1.1. LCBOP/EDIP Carbon Potentials.....	29
2.1.2. LAMMPS Simulation Setup.....	32
2.2. RESULTS AND DISCUSSION.....	33
2.3. CONCLUSION.....	37
3. ISOLATED CLUSTER ZERO KELVIN ATOMISTIC STUDIES.....	39
3.1. ISOLATED CLUSTER MODEL.....	39
3.1.1. Isolated Cluster Simulation Setup.....	39
3.1.2. Space Filling Models.....	40
3.1.3. Debye Scattering Profiles.....	41
3.2. RESULTS AND DISCUSSION.....	42
3.3. CONCLUSION.....	52
PAPER	
I. THE RATES OF UNLAYERED GRAPHENE FORMATION IN A SUPERCOOLED CARBON MELT AT LOW PRESSURE.....	55
ABSTRACT.....	55
1. INTRODUCTION.....	56

2. COMPUTATIONAL METHODS.....	57
3. RESULTS.....	60
4. DISCUSSION.....	64
5. CONCLUSION.....	65
ACKNOWLEDGEMENT.....	66
REFERENCES.....	66

SECTION

4. TEMPERATURE ANNEALS OF LIQUID CARBON.....	68
4.1. HEAT TREATMENT MODEL.....	68
4.1.1. Molecular Dynamics Thermostats.....	68
4.1.2. Molecular Dynamics Barostat.....	73
4.1.3. LAMMPS Heat Treatment Setup.....	76
4.2. RESULTS AND DISCUSSION.....	75
4.3. CONCLUSION.....	82
5. ANALYTICAL MODELING OF LIQUID CARBON 2D NUCLEATION AND SOLIDIFICATION.....	85
5.1. NUCLEATION MODEL.....	85
5.2. GROWTH MODEL.....	94
5.3. RESULTS AND DISCUSSION.....	97
5.3.1. Supercooling Thresholds.....	97
5.3.2. Solidification Rates.....	98
5.3.3. Graphene Sheet Size and Number Density.....	99

5.3.4. Saturation Effect on Slow Cooling.....104

5.4. CONCLUSION.....106

6. CONCLUSIONS.....110

BIBLIOGRAPHY.....119

VITA.....129

LIST OF ILLUSTRATIONS

Figure	Page
SECTION	
1.1. Carbon Allotrope Structures.	3
1.2. Carbon Phase Diagram.....	6
1.3. Updated Carbon Phase Diagram.....	7
1.4. Nanoscale Carbon Phase Diagram.....	8
1.5. Log-Log Nanoscale Carbon Phase Diagram.....	9
1.6. Murchison Meteorite.....	10
1.7. TEM Imaging of Carbonaceous Pre-solar Grain.....	13
1.8. Carbon Mass Density Versus Interatom Spacing.....	13
2.1. Composite Tiled-Cube Nearest Neighbor Histograms.....	37
3.1. Isolated Cluster Nearest Neighbor Histograms.....	45
3.2. Debye Scattering Profiles.....	51
PAPER	
1. Zeroth-Order Nucleation at Different Temperatures.....	61
2. Zeroth-Order Solidification Times as a Function of Temperature.....	62
3. Atomistic 2D Graphene Sheet Atoms as a Function of Temperature.....	63
SECTION	
4.1. 3D and 2D 100-Atom Liquid with 42-Atom Graphene Sheet Embedded.....	74
4.2. VMD of 3D Final Positions after 20ns Heat Treatment at 2800K.....	76

4.3. VMD of 2D Final Positions after 20ns Heat Treatment at 3800K.....	77
4.4. 2500 K Heat Treatment Energy vs. Time.....	78
4.5. Latent Heat of Fusion vs. Temperature for Different Pressure Cases.....	80
4.6. A Carbon Atom Through Time.....	80
5.1. 3D Cluster Free Energy vs. Cluster Radius.....	87
5.2. 2D Cluster Free Energy vs. Cluster Radius.....	91
5.3. AGB Star Temperature vs. Time for a Growing Carbon Grain.....	94
5.4. Growth Rate Temperature Dependence.....	96
5.5. Nucleation Rate Temperature Dependence.....	99
5.6. Effective Graphene Sheet Density vs. Mass Weighted Average Sheet Size.....	101
5.7. Graphene Sheet Density vs. Mass Weighted Average with Determined ΔH_f	103
5.8. Saturation End-Point Statistics.....	105
5.9. Analytical Density vs. Mass Weighted Average with Saturation.....	106

LIST OF TABLES

Table	Page
SECTION	
2.1. LCBOP/EDIP Loop Formation Statistics.....	35
2.2. LCBOP/EDIP Coordination Number Statistics.....	35
3.1. LCBOP Isolated Cluster Loop Formation Statistics.....	43
3.2. LCBOP Isolated Cluster Coordination Number Statistics.....	44
3.3. Isolated Cluster Space Filling Model Output.....	47
3.4. Isolated Cluster Preferred Density Statistics.....	47
3.5. Isolated Cluster Grain Size Statistics.....	50
4.1. Coordination Statistics and Binding Energies After Heat Treatment.....	81

1. INTRODUCTION

1.1. INTEREST IN ELEMENTAL CARBON

Carbon's structural diversity is one aspect that makes it interesting to study in many different fields. It has intriguing solid-state forms ranging from amorphous phases to graphite and diamond. Liquid carbon is thought to comprise of roughly 17% of Uranus and Neptune's total planetary mass [1]. A metallic liquid phase could exist within the deep interiors of both planets [2]. These metallic liquid phases could be the catalyst that leads to those planets' high magnetic moments. Difficulties arise experimentally in the formation of liquid carbon due to the high temperature and pressure levels needed. Requirements such as high pulsed laser heating of diamond-like carbon or graphite along with immediately measuring the rapidly expanding and boiling liquid phase are not trivial for experiment [3, 4, 5]. After cooling to ambient temperatures, a wide variety of structures have been reported to form; nanoclusters of diamond and graphite [4], carbyne chains [5], and novel superdense phases [6].

Pre-solar specimens extracted from meteorites have recently inspired some interesting results on the condensation of liquid carbon at low pressure, as well as its subsequent solidification. Submicron graphite-coated spheres containing unlayered graphene have been observed via transmission electron microscopy imaging and diffraction [7]. Electron phase contrast imaging of edge-on sheets has moreover suggested the presence of faceted penta-cones. This, and subsequent laboratory synthesis work, suggest that carbon vapor at low pressure condenses first as liquid droplets which, if cooled slowly, form unlayered graphene sheets in an otherwise disordered matrix. It also suggests

that pentagonal loops may play a role in the nucleation of those graphene sheets, raising the questions such as: What loops are more likely to form during the solidification of liquid carbon? And how does the nucleation of a supercooled low pressure carbon work? Before we can answer these questions, we need to first understand the different carbon allotropes and the pre-solar grains they can come from. As well as the theory and different methods that can be used to study these phenomena.

1.2. CARBON ALLOTROPES

There are eight well known and highly studied allotropes of carbon. Six of which can be seen in Figure 1.1. When carbon atoms are under standard temperature and pressure conditions, it has an interesting preference to have each atom bond to three nearest neighboring atoms 120 degrees apart. These bonds form sp^2 hybridization hexagonal sheets making up what is known as graphite. The three carbon atoms form strong covalent bonds with lengths of 1.42 Å. A weak Van der Waals attraction to the layer above and below stays stable with an interplanar spacing of 3.35 Å. With only three of the four bonding sites occupied, the fourth electron can migrate freely giving graphite a high electrical conductivity. Phonons will propagate quickly along the tightly bound planes but are slower to travel from one plane to another making the acoustic and thermal properties of graphite highly anisotropic giving graphite a high thermal conductivity and stability. These properties allow for widespread use as electrodes and refractories in high temperature material processing applications.

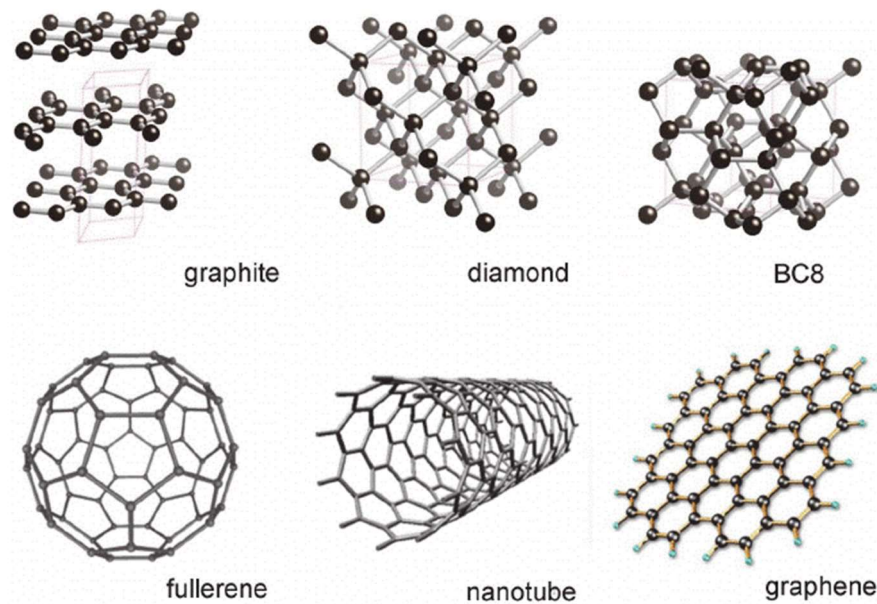


Figure 1.1. Carbon Allotropes Structures [8] (Orgav *et al.*).

For carbon under high pressures, each atom will bond to four other atoms forming a sp^3 hybridization carbon diamond cubic cell. This diamond cubic crystal structure will have a repeating pattern of 8 atoms. The crystal lattice of the diamonds forms a face-centered cubic which packs the atoms as tightly together as possible. The tight packing makes the diamond lattice very rigid due to strong covalent bonding between the atoms. Research had found that with this structure came the highest thermal conductivity for any bulk material above 100 Kelvin (K) [9].

When the diamond cubic cell has a hexagonal lattice, it is called lonsdaleite. This hexagonal diamond structure was first discovered in the Canyon Diablo meteorite of 1967 [10]. The lonsdaleite forms from graphite transforming into diamond but keeping the hexagonal symmetry when uniaxial pressure is applied to liquid carbon during its solidification [11]. Recent studies have predicted that lonsdaleite exhibits many excellent

mechanical properties better than diamond that can be used in areas of high-pressure research and applications [12]. On the other hand, nanodiamonds found in variety of extraterrestrial materials [13] or produced in the lab of type type Ia,b can have different impurities, such as nitrogen, within its bulk. The nitrogen impurities can replace a carbon atom within the diamond lattice forming nitrogen vacancy (NV) center point defects which have many interesting quantum mechanical properties. The stability of these quantum mechanical properties at room temperature and higher make them promising candidates for room temperature quantum sensing and computing devices [14-16].

One structure that was posited for many years, but not detected in nature [17] and outer space [18] after accidental synthesis [19], consists of a carbon molecule whose single or double bonds form a closed or partially closed mesh known as a fullerene. The discovery of the fullerene was able to expand the known allotropes of carbon from the limited amount graphite, diamond, and amorphous carbon (soot and charcoal). Fullerenes can take up different shapes such as hollow spheres, ellipsoids, tubes, and many others. The hollow tube is better referred as the carbon nanotube which is a hot topic due to being able to exhibit high electrical conductivity, exceptional tensile strength, high thermal conductivity, and some can even be great semiconductors.

An extreme member of the fullerene family will have the mesh flattened out with hexagonal rings making up a singular layer of graphite or better known as graphene [20, 21]. Graphene is part of a wide-reaching materials research topic which is currently rising in popularity known as a 2-dimensional material. Each carbon atom is connected to three nearest neighbors and form a sigma bond. The sigma bond is the strongest type of chemical covalent bond formed by head on overlapping between atomic orbitals. One electron is

contributed to the conduction band for the whole sheet. The conduction bands of graphene make it a semimetal with unusual electronic properties such as charge carriers in graphene show linear, rather than quadratic, dependence of energy on momentum, and field-effect transistors with graphene can be made that show bipolar conduction [20, 22].

One carbon structure that's stability has been a discussion of debate is a chemical structure that repeats as a chain of carbon atoms known as carbyne. The long chains of sp-hybridized carbon atoms are joined by alternating single and triple bonds or by consecutive double bonds as a one-dimensional structure. Carbyne has been detected naturally in interstellar dust and meteorites [23]. Studies have reported a long chain up to 44 carbon atoms synthesized experimentally in the lab [24] as well as synthesis in lab and from computational methods [25, 26]. These studies are showing carbyne to be a prominent structure in the liquid phase of carbon.

The different allotropes of carbon are stable or meta-stable depending on their current phase. The phase diagram in Figure 1.2 gives us the breakdown of the stable and meta-stable phases. Temperature values need to be greater than 4600 K at normal atmospheric pressures for carbon to be vapor and at high pressures for carbon to be liquid. These are extreme states making graphite and diamond the most common solid-state form of carbon as well as the most common form in general. As carbon heats up at standard pressures, its most direct conversion is from the solid phase to the vapor phase and vice versa when cooling down at standard pressures. Having the pressure be in the range of 0.1 to 0.01 Gpa during the cooling or heating process will have carbon enter a meta stable liquid phase during the conversion from vapor to solid or vice versa. The meta-stable liquid phase tends to have a short lifetime. The coexistence of all three phases is known as the

triple point, which appears at temperatures around 4600 K and roughly 0.01 Gpa. The nature of carbon allows for interesting supercooling phenomena. Studies into carbon's crystallization temperature have shown that it could have a supercooling threshold below 30% of the melting temperature [27].

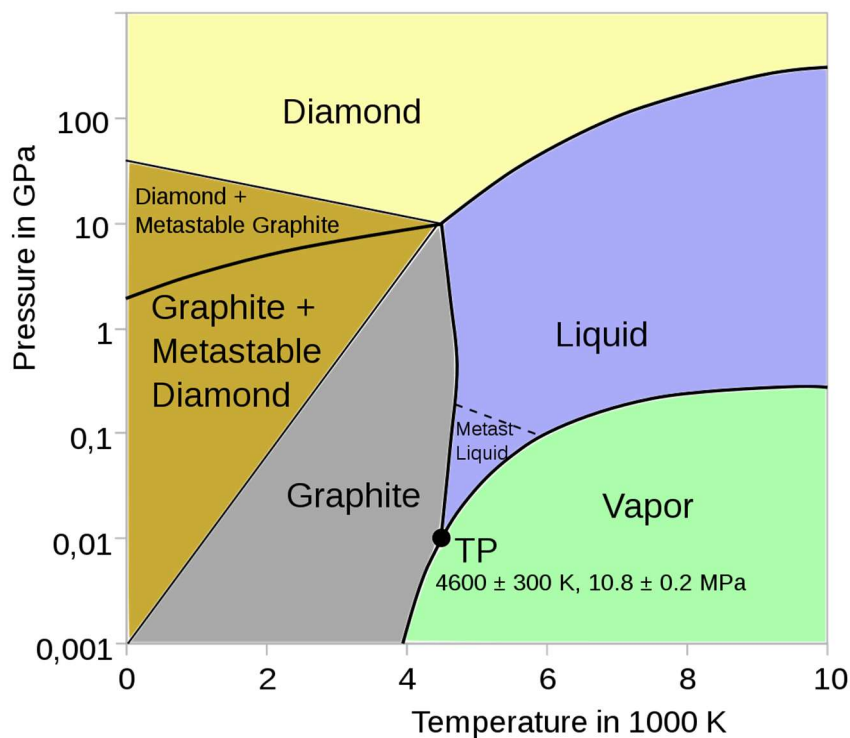


Figure 1.2. Carbon Phase Diagram [27].

Carbon's liquid phase has been a difficult phase to study and has sparked the interest of many scientists. Figure 1.3 shows a detailed modern understanding of the carbon phase diagram. Clear changes to the shape of the graphite melting curve have been predicted. At a temperature of 4800 K and pressure of 5 Gpa, the graphite melt line shows an inflection point and the slope of line can be represented by the Clapeyron equation,

$$\frac{dP}{dT_m} = \frac{\Delta S_m}{\Delta V_m}. \quad (1.1)$$

Here P is the pressure, T_m is the melting temperature, ΔS_m is the entropy change, and ΔV_m is the volume change. The previous studies suggested that the slope of the line changes in the presence of the inflection point at 4800 K under high pressure [28, 29].

The slope of the graphite melting line at low pressure is positive indicating the volume change should also be positive which points to the liquid being less dense than graphite. At higher pressures, the sign of the slope of the graphite melting line flips to negative because of the volume change is negative suggesting that the liquid is much denser than graphite. This would allow the liquid phase to go through a first-order liquid-liquid phase transition (LLPT) from a low density to a higher density [30-32]. This phase change would most likely happen in tetrahedral liquids [33-39]. The structures of the two liquid phases is important for the transition and has inspired the work here as well as other researchers to determine ways of studying this structure. This will be discussed more in depth in later sections.

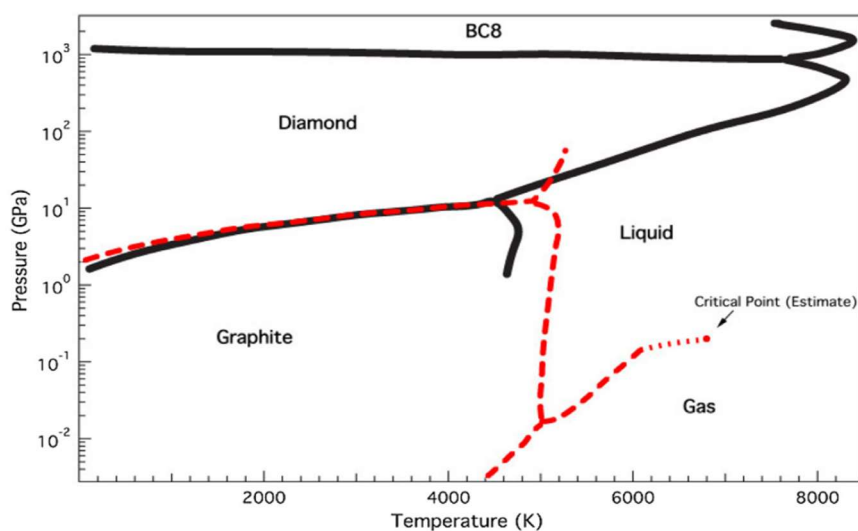


Figure 1.3. Updated Carbon Phase Diagram.

The phase diagrams of Figures 1.2 and 1.3 were studied by looking at micron scales and larger. Work looking at the nanometer scales to determine the particle cluster size effect on carbon phase diagram showed some possible changes to the carbon phase diagram [40]. Figure 1.4 shows smaller sized carbon clusters in a containerless setting at low pressures can be stable as a liquid well below the usual triple point for carbon. The nanoscale phase diagram shows that as the cluster sizes decrease, nano-diamonds are the stable phase even at low temp and pressures.

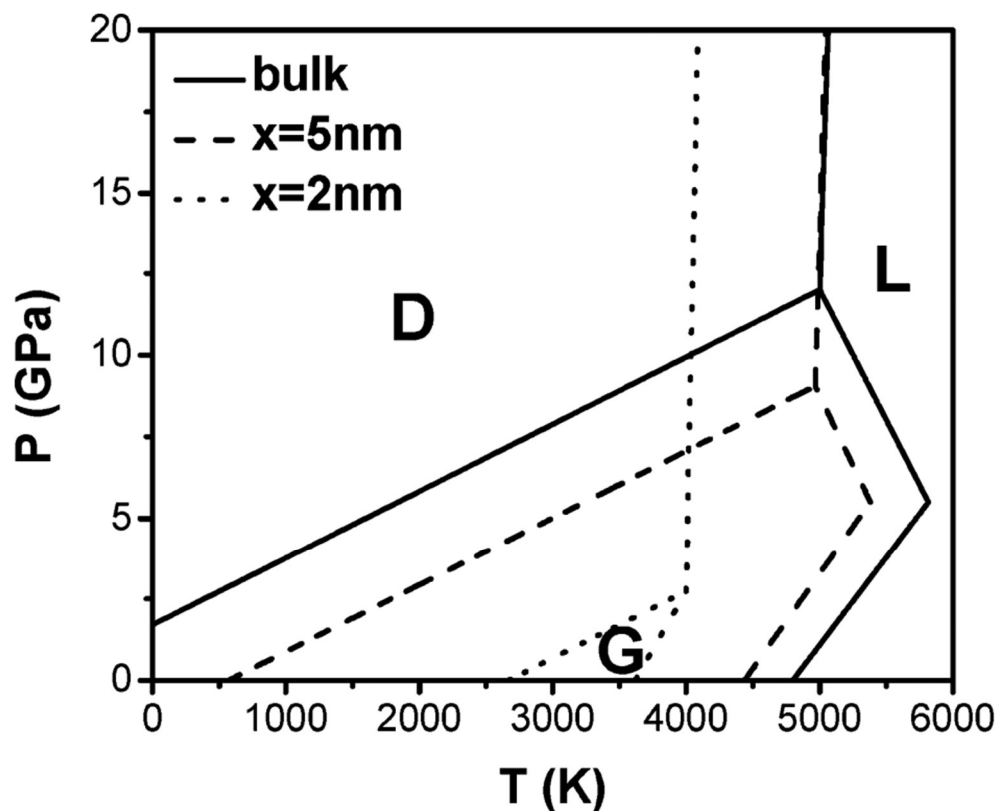


Figure 1.4. Nanoscale Carbon Phase Diagram. T-P phase diagram for bulk and nanocrystalline clusters of diamond. The areas are marked D = diamond, G = graphite, and L = liquid. The solid line denotes the bulk, the dashed is for 5 nm diameter clusters, and the dotted is for 2 clusters [40].

An extension of the phase diagram to show the vapor curve can be seen in Figure 1.5. The figure characterizes the bulk phase (solid line), the 2 nm cluster size carbon (dot-dashed line) and adds the vapor phase curve (red-dashed line) [41]. Denoting the points of $\frac{1}{2}$ and $\frac{2}{3}$ of carbon melting temperature shows the carbon vapor can condense as a stable liquid during the cooling process before solidification at low pressures. Experimental studies using laser ablation in liquid showed synthesis of nano diamonds from graphite under water confinement [42]. It was proposed that nano diamonds solidified from a supercooled liquid carbon state.

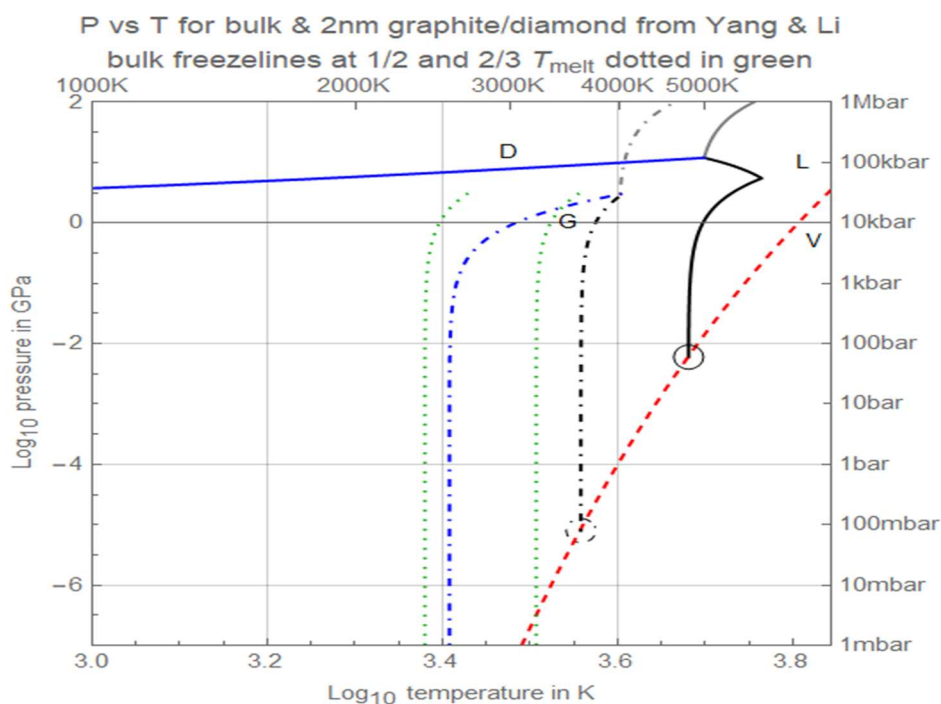


Figure 1.5. Log-Log Nanoscale Carbon Phase Diagram. P vs. T composite of the carbon phase diagram size effects (bulk solid, 2nm dot-dashed), combined with a carbon vapor pressure curve (dashed). D stands for diamond, G for graphite, L for liquid carbon, and V for carbon vapor, with color blue for the D-G transition, grey for the D-L transition, and black for the G-L transition. On heating carbon at low pressure sublimates before melting to the right of the red dashed line, even though on cooling the vapor may still condense as “supercooled” liquid before solidification at temperatures near those dotted green lines.

1.3. PRE-SOLAR GRAINS

Studies into carbon have been done widely on laboratory synthesized or naturally occurring forms of carbon. Another method for studying carbon can be by extracting the carbon from extraterrestrial materials [43]. Extraterrestrial materials are celestial objects which are sub categorized for the purpose of study on earth as cosmic dust, pre-solar grains, moon rocks and meteorites. A particular meteorite shown in Figure 1.6 was found in 1969 and named 'Murchison'. Scientists were able to extract silicon-carbide and date the meteorite at roughly 7 billion years old making it the oldest known material on earth [44].



Figure 1.6. Murchison Meteorite. Landed in Australia in 1969.

Pre-solar grains are some of the most interesting out of the different types of extraterrestrial materials as they are the most primitive minerals in solar system. The

formation of these grains occur flow out from red giant star atmospheres or during supernovae. The process of the pre-solar grain formation can be described as follows. The dust particles being pushed out via radiation pressure from many red giant stars and supernovae form a molecular cloud that ultimate forms a stellar nebula. Escaping grains will cool and solidify into celestial and interplanetary objects.

Pre-solar grains are comprised of various types of elements with different isotopic ratios. Carbon based structures and compounds can range from, graphite and diamond-based, titanium carbide, silicon carbide, silico nitride, nanodiamonds and much more. Variations of minerals within the different pre-solar grains imply origins in different parent stars and give information about stellar mixing. This could point to our solar system condensing form multiple stellar sources. Further studies using pre-solar grains to characterize the physical and chemical properties of the different possible parent star atmospheres [45, 46].

Carbonaceous pre-solar grains have been a topic of intense studies for many years. Research has found that carbon atoms formed in red giant star atmospheres during the first five billion years of our galaxy's lifetime. The carbonaceous pre-solar grains included graphite-only particles formed around carbide "seeds", micrometer-sized silicon carbide crystals, and nanodiamonds [47-50]. Carbonaceous pre-solar grains extracted exhibited KFA1 (2.05–2.10 g/cm³), KFB1 (2.10–2.15 g/cm³), and KFC1 (2.15–2.20 g/cm³) density fractions.

The high-density KFC1 fractions have well-ordered onion-like graphite rims condensed around a frozen liquid core from supercooled carbon droplets from the vapor phase. These micron-sized particles contain "slow neutron process" isotopes indicating

formation in asymptotic giant branch (AGB) stars after dredge-up of carbon formed in the star's interior [51]. The low-density KFA1 fraction consist of disordered graphite that point to origins from supernovae.

KFC1 grains were examined by diffraction and electron phase contrast (lattice) imaging using a 300kV Transmission Electron Microscope (TEM). The electron powder diffraction patterns of a selected area of these pre-solar grains gave evidence that the graphite onion cores contain unlayered graphene sheets with 40 Å coherence widths. The lattice imaging confirmed this and suggested further that the sheets nucleated to form faceted pentacones [52-54].

Figure 1.7a shows a false color slice of the core-rim pre-solar graphite onion extracted from Murchison meteorite. The field width of the false color image is on the order of a micron. Figure 1.7b shows a high-resolution TEM image of intersecting line segments. These intersections are made up of edge-on graphene sheets around 2–5 nm in length. They intersect at an angle between 39° – 65°. The electron diffraction only showed (hk0) spacings with the high frequency tails expected for atom thick sheets. There was also an absence of any graphite (002) “layering” lines. The intersecting atom thick graphene sheets must have formed faceted pentacones.

Synthesis of core-rim (& core-only) particles can be done in an “evaporating carbon oven” but graphene-sheet coherence widths turn out to be much smaller (around 1 nm). Figure 1.8 demonstrates the mass density versus nearest neighbor distances of elemental carbon phases. The tetrahedral (sp³ coordination) bonding of diamond and graphite (sp² coordination) has the smallest nearest neighbor spacing of 1.45-1.52 Å. This small nearest neighbor distance gives very strong covalent bonding. Experimental studies report a

density estimation for liquid carbon around 1.8 g/cm^3 end for unlayered graphene found in the core of pre-solar core-rim graphite onion [25, 52].

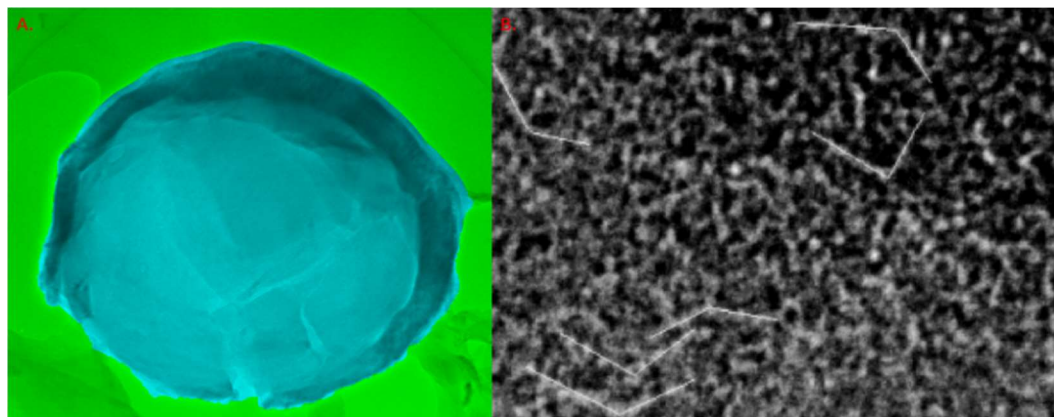


Figure 1.7. TEM Imaging of Carbonaceous Pre-Solar Grain. (a) A false-color TEM image of a slice from a graphitic onion particle from the Murchison meteorite with micron field width. (b) TEM image of thin onion core material with white lines denoting intersecting graphene sheets.

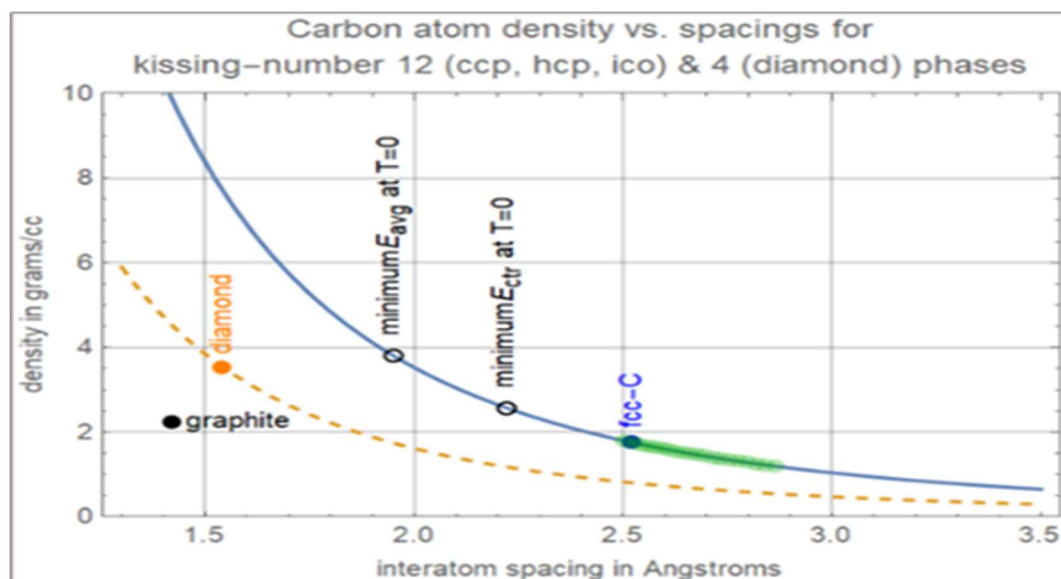


Figure 1.8. Carbon Mass Density Versus Interatom Spacing. The orange dashed line indicates the tetrahedral bonding of diamond face centered cubic arrangement. The dark blue line represents the coordination 12 cubic close pack arrangement of fcc-carbon and icosahedral symmetry of clusters. The density range 1.2 g/cm^3 – 1.8 g/cm^3 shown in green is for liquid carbon.

Due to extreme conditions, like high temperature and high pressure, needed to study liquid carbon in the lab, analytical modelling and computer simulation methods become an important role to understand the formation & structure of carbonaceous pre-solar grains. The experimental and pre-solar observations of graphite-onions and unlayered graphene gives a good starting point to direct the analytical and computational methods of future work.

1.4. NUCLEATION AND SOLIDIFICATION

1.4.1. Nucleation. When referring to nucleation, it is typically defined as the first step in the formation of the either of two processes: the formation of a new thermodynamic phase or a new structure via self-assembly or self-organization. The process of nucleation determines how long an observer must wait before the new phase or self-organized structure will appear. First-order phase transitions can be studied by understanding their nucleation process. Nucleation is known to be very sensitive to impurities within the system. Due to this sensitivity, it is important to distinguish between the types of nucleation, heterogeneous and homogeneous. Heterogeneous nucleation will occur at nucleation sites on the surfaces the system [55]. Homogeneous nucleation will occur away from surface becoming seeds for further heterogeneous nucleation.

Nucleation can usually be described as a stochastic (random) process. This means that two identical systems could have nucleation occur at different times [55-57]. The standard theory that describes the behavior of nucleation of a new thermodynamic phase is classical nucleation theory (CNT). CNT states that for a new thermodynamic phase, such as the formation of ice in water, if there is no evolution in time and the transition occurs in

one step, then the probability that nucleation has not occurred will be represented by a Boltzmann exponential factor. CNT is a widely used theory to approximate the rate of the exponential decay especially how they vary due to temperature. CNT is usually given by the following form [58],

$$r^* \cong \left(N \frac{k_B T}{h} \right) \exp \left[- \frac{(\Delta f^* + \Delta F^*)}{k_B T} \right]. \quad (1.2)$$

Here N is the number density of nuclei per unit volume, k_B is the Boltzmann constant, T is the temperature, h is Planck's constant, Δf^* the free energy of activation for short range travel across the interface to the new phase, ΔF^* is the free energy needed to create a critical-size cluster.

With heterogenous nucleation occurring much more than homogeneous nucleation, it can be observed that the heterogeneous nucleation will start when rate of homogeneous nucleation is essentially zero [55,57]. This switch between the two types of nucleation predicts nucleation decay due to a free energy barrier. This barrier is due to the cost, or penalty, of forming the surface of the growing nucleus. CNT makes several assumptions, such as the microscopic nucleus as a macroscopic droplet with a well-defined surface. A nucleus can be on the order of ten molecules across and treating it as a small volume with a surface is not always clear. Though the assumptions can be difficult to define, CNT accurately predicts the extreme decrease in wait time for nucleation when supersaturated [55,56] as well as being a very reasonable approximate theory for the crystallization of hard spheres [59]. CNT is also a useful starting point at predicting the nucleation process for supercooled liquids [60].

1.4.2. Solidification. A phase transition when the liquid turns into a solid is referred to as solidification. This process is usually described as freezing as normally the temperature of a system is lowered below the freezing point. This can also take place if the pressure of the system is increased enough for solidification to begin. Most crystals freeze by crystallization, the formation of solids in a highly organized structure. As long as the solid and liquid coexist, the temperature of the system should remain relatively equal to the melting temperature. Two major events occur during crystallization. The first being nucleation which was discussed in the previous section, and the second being growth.

Crystal growth will occur as the nuclei reach sufficient critical cluster size. Free particles will adsorb onto the critical nuclei and propagate the crystal structure outwards. Usually, the growth process is much more rapid than that of the nucleation process. This is due to the presence of dislocations and other defects acting as catalysts for additional particles. Defects can act as inhibitors to crystal growth as well due to modifying the crystal habitat [61]. Growth from liquids tend to require a finite degree of supercooling in order to lower the nucleation barrier to allow nucleation to occur from thermal fluctuations. Studies have shown that two major mechanisms take part in the growth from a melt: uniform normal growth and non-uniform lateral growth [62, 63].

Uniform normal growth is where the surface will propagate normal to itself without the need for any type of stepwise growth mechanic. This is a situation where there is a sufficient thermodynamic driving force (or degree of supercooling) present. Every element of surface will be capable to change continuously contributing to the propagation of the interface. Non-uniform lateral growth will have the surface propagate by lateral step motions which will be some integral multiple of the interplanar spacing in height. The step

is the transition between two adjacent regions of a surface. These surfaces are parallel to each other displaced by an integral number of lattice planes and have identical configurations.

The two growth mechanisms allow for the distinction if a surface will be singular or diffuse. A singular surface will have a pointed minimum for the surface tension as a function of orientation. Singular surfaces usually have non-uniform lateral step type growth. A diffuse surface will have the change from one phase to another be continuous. Carbon for geological time frames is not to be considered as a strong diffusion barrier. Carbonaceous pre-solar grains are indicating on stellar time frames this could be the opposite.

1.5. SEMI-EMPIRICAL INTERATOMIC POTENTIALS

The use of semi-empirical methods has, and will continue to be, an indispensable tool for studying many-particle systems. Semi-empirical methods use empirical corrections to improve theoretical models. In other words, experimental data is used to help improve the predictability and performance of different theoretical models. This is widely done for interatomic potentials which are functions derived to calculate the potential energy of a group of atoms given their positions in the system. Interatomic potentials are widely used in the fields of computational chemistry, physics, and materials science as the physical basis for molecular mechanics and molecular dynamics simulations. Interatomic potentials have been able to help to explain and predict different material properties such as lattice parameters, adsorption, thermal expansion, and interfacial energies.

1.5.1. Interatomic Potentials. We can write these interatomic potentials as a series expansion of functional terms that depends on the position of a number of atoms a time giving us a total potential as follows,

$$V_{total} = \sum_i^N V_1(\vec{r}_i) + \frac{1}{2} \sum_{i,j}^N V_2(\vec{r}_i, \vec{r}_j) + \frac{1}{6} \sum_{i,j,k}^N V_3(\vec{r}_i, \vec{r}_j, \vec{r}_k) + \dots \quad (1.3)$$

Here $V_{1,2,3}$ are the one-body, two-body, and three body-terms, N is the number of atoms in the system, $\vec{r}_{i,j,k}$ are the positions of atoms at i, j , and k . If we consider no external field, the one body term becomes negligible, and the potential only relies on the relative positions of the atoms and the angles between the bonds. The new form can then be written as,

$$V_{total} = \frac{1}{2} \sum_{i,j}^N V_2(\vec{r}_{ij}) + \frac{1}{6} \sum_{i,j,k}^N V_3(\vec{r}_{ij}, \vec{r}_{ik}, \theta_{ijk}) + \dots, \quad (1.4)$$

where $\vec{r}_{ij} = |\vec{r}_i - \vec{r}_j|$ is the interatomic distance and θ_{ijk} is the angle between the bonds. The three-body term does not require the interatomic distance between atoms j and k as the terms $\vec{r}_{ij}, \vec{r}_{ik}, \theta_{ijk}$ are able to give relative positions for three atoms in three-dimensional space. The terms that are of higher order than 2 are considered many-body potentials. For some interatomic potentials, the many-body terms are embedded into a pair-potential or also known as bond-order potentials.

The potential terms will sum over all N atoms, but assumptions of the range can give finite cutoffs. This cutoff will restrict to potential within a certain range making $V(r) \equiv 0$ at some distance r_{cutoff} . Applying this restriction and implementing a cellular method for finding nearest neighbors, the interatomic potential algorithm can be used for an $O(N)$ algorithm [64]. Leaving the infinite range on the N atoms, the sum of the potential

terms can be done efficiently by Ewald summation and its further developments as long as the system is periodic.

The interactions of the interatomic potentials are quantum mechanical in nature. The interactions described by both the Schrödinger equations and Dirac equations for all electrons and nuclei has been extremely difficult to cast into an analytical functional form. The difficulty to represent this quantum mechanical origin of the interactions has had potentials be built as parametric. In other words, they were developed and optimized with a fixed number of physical terms and parameters. Non-parametric potentials are being developed but are still in their infancy [65]. This means that all interatomic potentials will be approximations by necessity. Interatomic potentials have grown more and more complex increasing their accuracy, but this is still not strictly true [66].

One parametric potential that is arguably the simplest and most widely used is known as the Lennard-Jones potential [67]. The Lennard-Jones potential is usually represented in the following form,

$$V_{LJ}(r) = 4\varepsilon \left[\left(\frac{\sigma}{r} \right)^{12} - \left(\frac{\sigma}{r} \right)^6 \right]. \quad (1.5)$$

Here ε is the depth of the potential well, σ is the distance at which the potential crosses zero, the attractive term proportional $1/r^6$ comes from the scaling of the Van der Waals forces, and the repulsive term proportional to $1/r^{12}$ is an approximation by squaring the attractive term. The Lennard Jones potential is quantitatively accurate for noble gases and has been widely used for qualitative studies involving dipoles.

Another widely used potential is the Morse potential which takes a different approach to describing interatomic interactions [68]. The potential can be given by,

$$V_M(r) = D_e(e^{-2a(r-r_e)} - 2e^{-a(r-r_e)}), \quad (1.6)$$

here D_e is the equilibrium bond energy, r_e is the bond distance, and a controls the width of the potential. Applications of the Morse potential has helped studies of molecular vibrations and solids [69]. The Morse potential inspired the functional form for more accurate potentials such as bond-order potentials.

Bond-order potentials are widely used to describe covalently bonded system and are written based off the Linus Pauling bond order concept [70],

$$V_{ij}(r_{ij}) = V_{repulsive}(r_{ij}) + b_{ijk}V_{attractive}(r_{ij}). \quad (1.7)$$

Here the potential is written as a simple pair potential that depends on the interatomic distance r_{ij} . The strength of the bond is modified by the environment of atom i defined by the bond order b_{ijk} . For different potentials, this bond order can change to fit the model the potential is trying to approximate. A wide range of bond order potentials have been derived such as the Environment Dependent Interatomic Potential (EDIP) for silicon [71], the Finnis-Sinclair potential [72], the Reactive Force Field (ReaxFF) potential for hydrocarbons [73], and the Tersoff potential for silicon and carbon [74].

1.5.2. Tersoff Potential for Carbon. The development of the Tersoff potential initially came from motivations to study the different states of silicon. Being a bond order potential, the Tersoff potential incorporates a dependency on the number of bonds between pairs of atoms. This means that the order of the bonds is significant in how the Tersoff potential will model the bonds. For silicon oxide for example, the bonds of O-Si-O would be modelled differently from the bonds of Si-O-Si. The Tersoff potential consists of two-body terms and are dependent on the local environment [75]. The general form of the Tersoff potential is slightly different than the usual bond order potential and is given by,

$$\phi_{ij}(r_{ij}) = [\phi_R(r_{ij}) - B_{ij}\phi_A(r_{ij})]. \quad (1.8)$$

Similar to the general form for bond order potentials, there is a repulsive and attractive pair potential. The bond order term, B_{ij} , for the Tersoff potential will decrease as the coordination of the atoms increases. This means that the bond order is a function, $B_{ij}(\psi_{ij})$, dependent on the neighboring atoms at a certain distance and the angles between them. For studying liquid and amorphous phases of silicon, the Tersoff potential does a good job describing these different states.

Due to the similarities of silicon and carbon, Tersoff derived a form to work with carbon and carbons amorphous phases [76]. Starting from the general form of eqn. (7), the Tersoff potential for carbon can be written as,

$$\phi_{ij}(r_{ij}) = \phi_{ij}^C(a_{ij}\phi_{ij}^R - b_{ij}\phi_{ij}^A), \quad (1.9a)$$

$$\phi_{ij}^R = Ae^{-\lambda_1 r_{ij}}, \quad (1.9b)$$

$$\phi_{ij}^A = Be^{-\lambda_2 r_{ij}}. \quad (1.9c)$$

Here ϕ_{ij}^R and ϕ_{ij}^A are the competing repulsive and attractive pairwise potential terms, $\lambda_{1,2}$, A, and B are constants, and ϕ_{ij}^C is the cut-off term ensuring that only nearest neighbor atoms are considered in the interaction. The a_{ij} is a range limiting term on the repulsion that is usually set to one. As stated before, the bond order, b_{ij} , will depend on the local coordination of the atoms and can be written as,

$$b_{ij} = (1 + \beta^n \zeta_{ij}^n)^{-\frac{1}{2n}}, \quad (1.10a)$$

$$\zeta_{ij}^n = \sum_{k \neq i, j} \phi_{ik}^C g_{ijk} e^{\lambda_3^3 (r_{ij} - r_{ik})^3}, \quad (1.10b)$$

$$g_{ijk} = 1 + \frac{c^2}{d^2} - \frac{c^2}{d^2 + (h - \cos[\theta_{ijk}])^2}. \quad (1.10c)$$

θ_{ijk} is the angle between the atoms i , j , and k . The bond angle term describes the strong covalent bonding of carbon systems in different types of geometries which cannot be represented by a purely central potential model.

The Tersoff potential for carbon was later extended to describe diamond and take into account hybridization changes as bonds are broken and formed. This extension is known as the Brenner potential [77]. For solid-state carbon structures, the Brenner potential is given by the following functions,

$$\phi_{ij}(r_{ij}) = \phi_{ij}^C(\phi_{ij}^R - \bar{b}_{ij}\phi_{ij}^A), \quad (1.11a)$$

$$\phi_{ij}^R = \left(1 + \frac{Q}{r_{ij}}\right) A e^{-\alpha r_{ij}}, \quad (1.11b)$$

$$\phi_{ij}^A = \sum_{i=1}^3 B_n e^{-\lambda_n r_{ij}}. \quad (1.11c)$$

Many of the terms are similar to that of Tersoff original form for carbon. The bond order term, \bar{b}_{ij} , for the Brenner potential is written as follows,

$$\bar{b}_{ij} = \frac{1}{2}(b_{ij}^{\sigma-\pi} + b_{ji}^{\sigma-\pi}) + \Pi_{ij}^{RC} + b_{ij}^{DH}, \quad (1.12a)$$

$$b_{ij}^{\sigma-\pi} = \left(1 + \sum_{k \neq i,j} f_{ik}^C g_{ijk}\right)^{-\frac{1}{2}}, \quad (1.12b)$$

$$g_{ijk} = \sum_{i=0}^5 \beta_i \cos^i[\theta_{ijk}]. \quad (1.12c)$$

For the Brenner potential we have the term $b_{ij}^{\sigma-\pi}$ known as the pi-bond function. Similar to Tersoff's original form, the function depends on the coordination between the atoms but will also depend on the angle between the bonds. For graphene, graphite, and diamond this pi-bond function is symmetric giving $b_{ij}^{\sigma-\pi} = b_{ji}^{\sigma-\pi}$. The coefficients, β_i , that are part of the bond-bending spline function were extrapolated from experimental data for graphite and diamond. The term Π_{ij}^{RC} takes into account radical energetics such as vacancies and other defects, and b_{ij}^{DH} is a dihedral bending function that depends on local conjugation. This term is zero for diamond but is important for describing graphene and is given by,

$$b_{ij}^{DH} = \frac{T_0}{2} \sum_{k,l \neq i,j} \phi_{ik}^C \phi_{jl}^C (1 - \cos^2[\Theta_{ijkl}]). \quad (1.13)$$

T_0 is a fitting parameter, ϕ_{ik}^C is the cut-off function, and Θ_{ijkl} is the dihedral angle of four atoms i, j, k , and l . For flat graphene, the dihedral angle is either 0 or π making b_{ij}^{DH} go to zero, but if the graphene bends the contribution of this term is not negligible.

Other expansions of the Tersoff potential have been derived over the years. One such expansion was derived to describe small-scale defects on graphite surfaces [78]. Another expansion wanted to study the sp^2/sp^3 characterization techniques of X-ray photoelectron versus high energy electron energy-loss spectroscopy [79]. The Tersoff potential and its expansions are widely used in a method for analyzing the movements of atoms and molecules known as molecular dynamics. One of most recent expansion of the Tersoff potential was trying to improve the potentials accuracy of simulating graphene in different environments [80]. Even with all these expansions, one place where these potentials fall short is in the cut-off of the interactions. The cut-off function plays a big role in trying to study the molecular dynamics of carbon as a liquid. Before we dive more into

that, it is first useful to understand what exactly molecular dynamics means as a method for studying liquid carbon.

1.6. MOLECULAR DYNAMICS

To put it simply, molecular dynamics (MD) is a computational method for analyzing the physical movements of atoms and molecules. What this entails is allowing the atoms or molecules to interact over a given period of time to show the dynamic evolution of the system. The most common type of molecular dynamics simulation has trajectories of atoms and molecules determined by numerically solving Newton's equations of motion. This is done by having the forces and potential energies of the interacting particles calculated using interatomic potentials or molecular force fields. MD is widely used in the field of biophysics, chemical physics, and material science.

Molecular systems tend to consist of a vast number of particles. This makes it extremely difficult to determine properties of the complex systems analytically. MD simulations are able to circumvent this problem by employing numerical methods. Where numerical methods are algorithms that make numerical approximations for solving calculations. Due to the numerical approximations, long MD simulations generate cumulative errors making them mathematically ill-conditioned without proper algorithm and parameter selection. Even with the proper selections of algorithms and parameters, the errors will not be eliminated fully.

Systems that obey the ergodic hypothesis, which states over long periods, the time spent by a system in some region of the phase space of microstates with the same energy is proportional to the volume of this region. Another way of putting this is to say that all

accessible microstates are equiprobable over a long period of time. This means that for one MD simulation evolution of a microcanonical ensemble may be used to determine macroscopic thermodynamic properties. The microcanonical ensemble evolutions are normally referred to as microcanonical ensemble averages. This is just one type of constraint that MD simulations can have on the system. To understand MD simulations further, we need to understand what the different ensemble constraints can be assumed for a given system.

1.6.1. Microcanonical Ensemble. Considering again the microcanonical ensemble mentioned previously, we consider a system that will be isolated from changes in number of atoms, volume, and energy. This corresponds to an adiabatic process, which is a thermodynamic process without the exchange heat or mass between the surroundings. These constraints on this statistical ensemble allow for the systems energy to be exactly specified. The MD for a microcanonical ensemble will have the exchange of potential and kinetic energy in a way where the total energy is conserved.

1.6.2. Canonical Ensemble. Now for a system where the number of atoms, the volume, and the temperature are held constant, we have what is defined as the canonical ensemble. This statistical ensemble will have all possible states in thermal equilibrium with a heat bath, or thermal reservoir. The system is allowed to exchange energy with the thermal bath and is dependent on the number of atoms and volume of the systems which will affect the systems internal states. The energy of the endothermic and exothermic exchanges is given by a thermostat. A thermostat in MD simulations is an algorithm which adds and removes energy from the boundaries in an approximately realistic way. Thermostat methods control the temperature by rescaling the velocity. Some popular

thermostats are the Berendsen thermostat [81], the Nosé-Hoover thermostat [82], and the Langevin dynamics thermostat [83]. Not all thermostats will work for any given system as it is not trivial to gain the canonical ensemble distribution and velocities.

1.6.3. Isothermal-Isobaric Ensemble. There also might be systems that need more than just a thermostat, but also a barostat. The barostat will be needed for situations where the number of atoms, pressure, and temperature are held constant. This type of statistical ensemble is referred to as an isothermal-isobaric ensemble. The system for an isothermal-isobaric ensemble will correspond closely to laboratory conditions. For example, our box that makes up the system will be open to ambient temperatures and pressures. This type of ensemble plays an important role in chemistry and chemical physics [84] and is useful for measuring the equation of state for a system whose virial expansion for pressure is too complex to be evaluated or the system is near a first-order phase transition [85].

1.6.4. Generalized Ensemble. The main three ensembles discussed have set specific constraints on a thermodynamic system. The dynamics tend to be fast and there is usually some order within the systems. When applying the different ensembles, different computational errors can arise based on the different constraints. This has led to studies into creating a generalized ensemble for use in MD simulations. One method is referred to as the parallel tempering method which was initially created to study slow dynamics and disordered spin systems [86]. Parallel tempering is the simulation N copies of a system randomly initialized at different temperatures. The simulation allows for a given criterion that the high temperature configurations can be available to the low temperature configurations. This will allow for thermodynamic properties such as specific heat to be determined with great precision which is not always the case for canonical ensembles.

1.6.5. Molecular Dynamics Applications. As stated before, MD is a useful tool in the fields of chemistry, chemical physics, biophysics, and material science. In biological systems, MD simulations were able to show that protein motion was essential in function and not just accessory [87]. The importance of MD simulations its ability to allow for the study of materials at the atomic scale. This was shown in the grain size evolution of nanocrystalline aluminum wear and friction [88]. Beyond this, as MD simulations are updated and improved, they become a necessary tool for studying physical systems which are not easily attainable within the laboratory. Such a system is the high temperature and pressure environment that will have carbon in a liquid phase.

1.7. OUTLINE OF WORK

The work presented here studies the nucleation and solidification of liquid carbon. More specifically, we are studying these processes both analytically and atomistically for a supercooled carbon melt at low pressures.

Section two goes over zero kelvin tiled-cube energy minimizations using semi-empirical potentials in a MD simulator of 100 atom carbon sets at densities of 1.8 g/cm^3 which are the observed estimates for liquid carbon densities. N-member loop statistics, coordination statistics, and nearest neighbor histograms were generated from the atom lists. Section three goes over isolated cluster zero kelvin MD simulations of similar 100 atom liquid carbon sets. Like the tiled-cube simulations, N-member loop statistics, coordination statistics, and nearest neighbor histograms were generated, but also studies into preferred density, grain size, and Debye scattering profiles were done.

Paper I is previously published work that studies a zeroth order few-parameter nucleation and solidification model for supercooled carbon liquid at low pressures. Alongside that, we study the growth of the carbon melt with a graphene sheet embedded using MD anneals at different temperature ranges.

Section four goes over the atomistic molecular dynamics simulations done to study growth in both 3D and 2D. The Nosé-Hoover thermostat was used with the best performing semi-empirical potential from the zero-kelvin simulations. The data gained from the different heat treatments allowed us to determine different parameters for use in modeling the nucleation and growth analytically. Section five goes over the analytical 2D nucleation and growth models for the low-pressure liquid carbon studied here.

2. TILED-CUBE ZERO KELVIN LOOP COUNTING AND COORDINATION STATISTICS

2.1. TILED-CUBE MODEL

Observations of pre-solar grains had evidence of submicron graphite coated spheres of unlayered graphene forming around a liquid core [7]. Closer investigation via transmission electron microscopy showed joints within the core indicative of faceted pentacones. It is believed that these faceted pentacones could only form from a nucleation seed of a pentagonal ring instead of the usual hexagonal ring of graphite and graphene [52-54]. The conditions required to study the carbon liquid are very difficult to get in laboratory settings, so our method has us study the carbon liquid computationally.

2.1.1. LCBOP/EDIP Carbon Potentials. When studying carbon using interatomic potentials, Tersoff and its extensions have been able to make useful predictions of carbon's solid phases. These potentials fall short when studying graphite layering and liquid phases of carbon due to their short cut-off distances around 2.1 Å. Liquid carbon is believed to have interaction distances around 2.5 Å. Two recent potentials have been built on the shortcomings of Tersoff with long-range interaction cut-offs: the Long-Range Carbon Bond-Order Potential (LCBOP) and the Environment Dependent Interatomic Potential (EDIP) [89, 90].

The starting point of LCBOP is the Brenner extensions of Tersoff. The Brenner potentials describe only the strong covalent bonds, underestimate isotropic elastic constants, and neglect long-range interactions. LCBOP take a different approach of most long-range extensions of Brenner/Tersoff. The nearest-neighbor interactions are the only pieces excluded from the long-range interactions and the short-range interactions are

parameterized in such a way that the combined short- and long-range interactions yield correct properties such as binding energies, conjugation effects, elastic properties, and lattice constants.

Instead of using the Lennard-Jones potential for the long-range interaction, LCBOP uses a Morse-like potential which was based on a best fit for interlayer interaction energy in graphite calculated by local density approximations. The binding energy of the LCBOP semi-empirical potential can be written as follows [89],

$$E_b^{LCBOP} = \frac{1}{2} \sum_{i,j}^N V_{i,j}^{tot} = \frac{1}{2} \sum_{i,j}^N (f_{c,ij} V_{ij}^{SR} + S_{ij} V_{ij}^{LR}). \quad (2.1)$$

Here the total pair potential, $V_{i,j}^{tot}$, is the sum of the short-range interactions, $f_{c,ij} V_{ij}^{SR}$, and the long-range interaction, $S_{ij} V_{ij}^{LR}$. For the short-range interaction, $f_{c,ij}$ is a smooth cut-off function where for the long-range interaction, S_{ij} is a switching function that excludes first neighbors. The short-range piece resembles the Tersoff bond-order and is given by,

$$V_{ij}^{SR} = V_R(r_{ij}) - B_{ij} V_A(r_{ij}), \quad (2.2a)$$

$$V_R(r) = A e^{-\alpha r}, \quad (2.2b)$$

$$V_A(r) = B_1 e^{-\beta_1 r} + B_2 e^{-\beta_2 r}. \quad (2.2c)$$

V_R and V_A are the repulsive and attractive radial pair potentials and B_{ij} is the bond-order which contains many-body effects. The switching function is given by,

$$S_{ij} = 1 - f_{c,ij}, \quad (2.3a)$$

$$f_{c,ij}(x) = \Theta(-x) + \Theta(x) \Theta(1-x) \exp\left[\frac{\gamma_{LCBOP} x^3}{x^3 - 1}\right]. \quad (2.3b)$$

The cut-off function, $f_{c,ij}(x)$, was adopted from the EDIP potential for silicon where $x = (r - r_1)/(r_2 - r_1)$, and $\Theta(x)$ is the Heavyside step function [91]. The γ_{LCBOP} parameter is used to optimize the shape of the energy barrier for the diamond to graphite transition. The cut-off function is continuous up to the second derivative at $r = r_1$ and all its derivatives at the cut-off radius r_2 . This function yields a much smoother cut-off than the cosine functions used by Brenner and Tersoff. The bond-order term, B_{ij} , is taken to be,

$$B_{ij} = \frac{1}{2} [b_{ij} + b_{ji} + F^{conj}(N_{ij}, N_{ji}, N_{ij}^{conj})], \quad (2.4)$$

where b_{ij} is the angular dependent piece which is optimized for elastic properties, surface properties, and the energy barrier for the diamond to graphite transformation. F^{conj} considers conjugation effects.

The formulation of EDIP for carbon began from the original EDIP potential for silicon. EDIP for carbon has addressed a major weakness for the silicon version, namely, the absence of π -bonding. This added improvement allows for important phenomena like dihedral rotation penalties and π -repulsion to be described. Writing EDIP for carbon gives a functional form consisting of three components: a two-body pair-wise energy, a three-body angular penalty, and a generalized coordination. The two- and three-body terms will have environment dependence controlled by the atomic coordination Z . The total energy can be written as [90],

$$E_b^{EDIP} = \sum_j V_2(r_{ij}, Z_i) + \sum_{j < k} V_3(r_{ij}, r_{ik}, \theta_{ijk}, Z_i). \quad (2.5)$$

Here V_2 is a short-range pair potential of the Stillinger-Weber (SW) form [92-94]. The short-range SW potential decays to zero at a distance set by the denominator in the exponential and can be written as,

$$V_2(r, Z) = \varepsilon \left[\left(\frac{B}{r} \right)^4 - e^{-\beta Z^2} \right] \exp \left[\frac{\sigma}{r - a - a'Z} \right]. \quad (2.6)$$

The bond-order is described by the exponential term $-\beta Z^2$ and the cut-off is controlled by the variable parameter a' .

The three-body term uses a SW-like potential as well with the form,

$$V_3(r_{ij}, r_{ik}, \theta, Z) = \lambda(Z)g(r_{ij}, Z)g(r_{ik}, Z)h(\theta, Z). \quad (2.7)$$

Here the distances r_{ij} and r_{ik} will be less than the interaction cut-off and the three functions that make up this potential are given by,

$$\lambda(Z) = \lambda_0 e^{-\lambda'(Z-z_0)^2}, \quad (2.8a)$$

$$g(r, Z) = \exp \left[\frac{V_{EDIP}}{r - a - a'Z} \right], \quad (2.8b)$$

$$h(\theta, Z) = 1 - \exp[-q[\cos\theta + \tau(Z)]^2]. \quad (2.8c)$$

The term $\tau(Z)$ describes the variation in ideal bond angle based on the atom coordination. This term gives angular penalties like the Brenner and Tersoff potentials and follows the SW potential philosophy that there is an ideal angle, θ_0 , where there would be no angular penalty.

2.1.2. LAMMPS Simulation Setup. To employ the LCBOP and EDIP potentials in these studies of liquid carbon, we used a software distributed by Sandia National labs known as the Large-scale Atomic/Molecular Massively Parallel Simulator (LAMMPS) [95]. LAMMPS is a molecular dynamics coding software with a focus on materials modeling. The molecular dynamics software has been built as a tool for modeling atoms at the atomic, meso, or continuum scale.

The system setup for use in the MD simulator was that of 100 carbon atoms randomly placed with nearest neighbors distanced ranging from 1.4 – 1.9 Å. The simulation

box had side lengths of 10.345 Å to give a density of 1.8 g/cm³ which is the predicted density of liquid carbon from pre-solar and lab observations. The box was given periodic boundary conditions so we could simulate the conditions for an infinite crystal.

With the simulation box set up, we performed a zero-kelvin energy minimization via the Polak-Ribiere version of conjugate gradient optimization which is believed to be the most effective conjugate gradient method for most systems [96]. This optimization finds the arrangement of the atoms where the energy is minimum. The situation for energy minimum is set when the difference between atom arrangement gives an energy difference of 10^{-25} eV or less. Once the system is relaxed, we use the final positions to determine how many of n-member rings, where 5-member rings are pentagons and 6-member rings are hexagons, formed during relaxation.

Code was developed to determine the ring formation, coordination, and nearest neighbor statistics for a given set of atom positions. For the ring statistics, we followed methods of Deringer and Franzblau *et al.* [97,98] to place the correct constraints on what should be considered a ring and to make sure rings spanning the boundaries are neglected. The coordination statistics had a cut-off constraint of 1.7 Å interatomic distance as this is the believed covalent bond length cut-off for liquid carbon based on pre-solar and lab observations.

2.2. RESULTS AND DISCUSSION

To determine which n-member rings would be preferred nucleation seeds, loop formation statistics were taken after energy minimization of the system using both LCBOP and EDIP. The 100 atom sets had different constraints on atom distance when randomly

placed in the cell ranging from 1.4 to 1.9 angstroms. We notice first that allowing the atoms to be as close as 1.4 angstroms when using the LCBOP potential does not give more loops than atoms that are restricted to 1.9 angstrom distance. Knowing this, when using the EDIP potential, we had our atom distance constraint set to the Van der Waals radius of 1.7 Å for carbon.

Table 2.1 shows that pentagons form with the same frequency as hexagons for LCBOP and are the most prominent loop for EDIP. The pentagon formation amounts agree with independent DFT studies and other computational methods [98-101], but total ring formations are lower. Though EDIP has mainly pentagonal loops form, it also has the presence of 3- and 4-member loops which are believed to be non-physical or metastable. The formation of pentagonal loops in our simulations strengthens the conclusions of pre-solar data that the joints from the TEM could be from a pentagon being a nucleation seed. These pentagon nucleation seeds forming initially to create the cone shape of the faceted pentacones.

Along with loop formation, coordination number statistics of the 100 atom lists was determined. To keep consistency, the starting atoms for the coordination number sets had a distance constraint of the Van der Waals radius. Table 2.2a shows for the LCBOP case that coordination number 2 (sp) and coordination number 3 (sp²) are the most prominent for the relaxed atoms. This shows that carbyne (sp) and graphene/graphite (sp²) structures are forming the most during the energy relaxation process for the different 100 atom sets. Table 2.2b shows the EDIP case, which shows a similar high amount of carbyne coordination, but less graphene/graphite coordination. There is also double the percentage of coordination-1 dipoles compared to LCBOP.

Table 2.1. LCBOP/EDIP Loop Formation Statistics. a.) LCBOP and b.) EDIP after energy minimization of 100 randomly placed carbon atoms in a cell with periodic boundary conditions and volume set to give 1.8 g/cm³ liquid carbon density.

a.) LCBOP 100 Atom Loop Statistics (Tiled-Cubes)						b.) EDIP 100 Atom Loop Statistics (Tiled-Cubes)					
n	3	4	5	6	7	n	3	4	5	6	7
100-1.9a	0	0	0	0	0	100-1	0	2	1	0	0
100-1.8a	0	0	1	3	2	100-2	0	0	1	0	0
100-1.7a	0	0	3	3	1	100-3	1	1	2	0	1
100-1.6a	0	0	3	1	0	100-4	0	2	0	0	0
100-1.5a	0	0	1	3	1	100-5	0	0	2	1	0
100-1.4a	0	0	1	2	2	100-6	0	1	2	0	1
100-1.9b	0	0	1	3	1	100-7	0	0	1	0	0
100-1.8b	0	0	2	3	4	100-8	1	0	2	2	0
100-1.7b	0	0	2	2	1	100-9	0	0	0	0	1
100-1.6b	0	0	2	3	2	100-10	0	0	3	0	0
100-1.5b	0	0	2	0	3	Percentages	0.20%	0.60%	1.40%	0.30%	0.30%
100-1.4b	0	0	1	0	1						
100-vdwr-1	0	0	0	1	0						
100-vdwr-2	0	0	3	0	2						
100-vdwr-3	0	0	2	1	3						
100-vdwr-4	0	0	1	0	1						
100-vdwr-5	0	0	4	4	4						
100-vdwr-6	0	0	0	2	5						
100-vdwr-7	0	0	4	4	2						
100-vdwr-8	0	0	1	1	0						
100-vdwr-9	0	0	3	3	5						
100-vdwr-10	0	0	2	3	5						
Total Loops	0	0	39	42	45						
Percent per atom	0.00%	0.00%	1.77%	1.91%	2.05%						

Table 2.2. LCBOP/EDIP Coordination Number Statistics. a.) LCBOP and b.) EDIP after energy minimization of 100 randomly placed carbon atoms in a cell with periodic boundary conditions and volume set to give 1.8 g/cm³ liquid carbon density.

a.) LCBOP 100 Atom Coordination Statistics (Tiled Cubes)						b.) EDIP 100 Atom Coordination Statistics (Tiled-Cube)					
Coordination Number	0	1	2	3	4	Coordination Number	0	1	2	3	4
100-vdwr-1	3	12	48	35	2	Trial 1	2	16	55	26	1
100-vdwr-2	2	12	41	42	3	Trial 2	5	23	49	21	2
100-vdwr-3	0	11	45	43	1	Trial 3	1	17	45	37	0
100-vdwr-4	1	9	46	43	1	Trial 4	2	27	49	21	1
100-vdwr-5	0	11	37	49	3	Trial 5	2	32	37	33	1
100-vdwr-6	1	14	43	37	5	Trial 6	4	11	49	33	3
100-vdwr-7	3	15	32	49	1	Trial 7	5	28	48	18	1
100-vdwr-8	1	6	51	42	0	Trial 8	3	22	43	28	4
100-vdwr-9	1	12	41	42	4	Trial 9	7	21	45	25	2
100-vdwr-10	2	12	38	46	2	Trial 10	6	26	40	26	2
Totals Atoms per Coord-#	14	114	422	428	22	Totals Atoms per Coord-#	37	223	460	268	17
Percentage of Coord-#	1.40%	11.40%	42.20%	42.80%	2.20%	Percentage of Coord-#	3.70%	22.30%	46.00%	26.80%	1.70%

The high percentage of graphene/graphite sp^2 -coordination formation for LCBOP shows that the structure preference after relaxation is that of graphene/graphite. This follows independent DFT studies as well as what was seen by the pre-solar data as there was evidence of unlayered graphene formation. The high percentage of carbyne coordinated atoms for both the LCBOP and EDIP cases agree with other DFT studies into low density liquid carbon [26].

Determining the nearest neighbor atom distances after relaxation can give information on whether the atoms are bonding covalently or metallicly and links directly to radial distribution and correlation functions. Composite nearest neighbor histograms of the interatom distances were generated for the 10 Van der Waals radius constrained sets for both LCBOP and EDIP. The spike at 0 Å in Figure 2.1 is from finding an atom on top of itself, so it counts the total amount of 100 atoms for each 10 sets giving a count of 1,000. For the LCBOP case shown in Figure 2.1a, a noticeable gap between 1.7 and 2.2 Å in the interatomic distances can be seen. For the EDIP case shown in Figure 2.1b, the gap is less defined and only goes from 1.85 to 2.1 Å.

This gap could be showing the atomic distances for covalent and metallic bonds as the carbon atoms are preferring these interatomic distances. More metallic bonds are present than covalent bonds which could be evidence of a metastable metallic liquid carbon at these low densities. Taking the number of pairs with the limit of 2.6 Å and subtracting off the number of pairs with the limit of 1.7 Å we see that 52% of the atoms are preferring the metallic bonding interatomic distance.

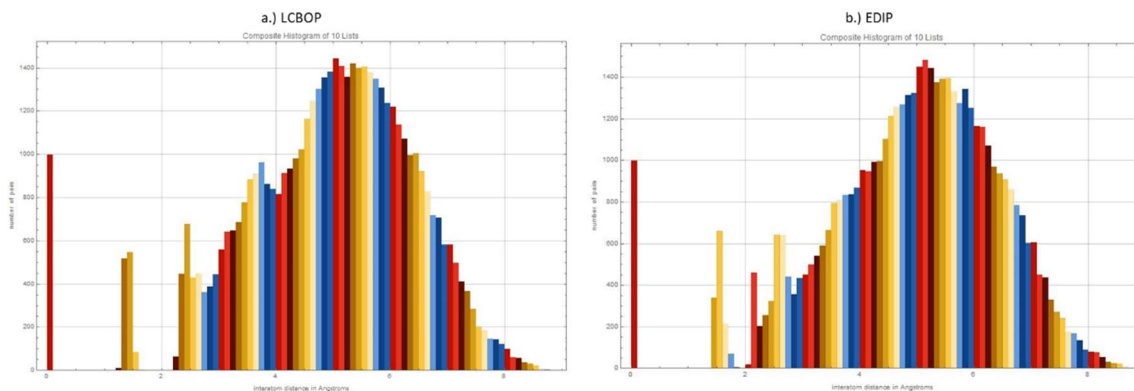


Figure 2.1. Composite Tiled-Cube Nearest Neighbor Histograms. a.) LCBOP and b.) EDIP after energy minimization of 10 sets of 100 randomly placed carbon atoms in a cell with periodic boundary conditions and volume set to give 1.8 g/cm^3 liquid carbon density.

2.3. CONCLUSION

In this section, two semi-empirical potentials written to incorporate long-range interactions that are present in carbon were used in the LAMMPS MD simulation software. Zero kelvin energy minimizations using the Polak-Ribiere version of conjugate gradient optimization was done on 100 carbon atom sets where the simulation box had periodic boundary conditions and the volume gave the experimentally expected density for liquid carbon of 1.8 g/cm^3 . From the relaxed atom positions, n-member loop formation, coordination statistics, and nearest neighbor histograms were studied.

The loop formation statistics for both the LCBOP and EDIP potentials had 5-member loops have prominent formation. The presence of pentagonal loop formation in the energy minimizations indicate that pentagons can be seeds for nucleation within the low-density liquid carbon. EDIP did have the pentagonal loop formations be its highest percentage of loop formation, but it also had 3- and 4-member loops present which are believed to be nonphysical or metastable at best.

After looking at the loop formations, coordination statistics were determined for the different 100 atom sets. For the LCBOP case, carbyne sp -coordination and graphene/graphite sp^2 -coordination are the preferred structural coordination after energy minimization with percentages of 42% and 43% respectively. Though compared to other work done on carbon coordination there is a much higher percentage of carbyne coordination [102], the higher values agree with other observations of low-density carbon [25,26]. The high percentage of carbyne and graphene/graphite coordination with prominent pentagonal loop formation could also be evidence of the pentagon-first mechanism of Y-junction carbyne chains.

The nearest neighbor histograms for both LCBOP and EDIP were able to shed light on preferred bond distances for the liquid after energy minimization. For LCBOP, a clear gap between 1.7 and 2.2 Å indicate interatomic distances of covalent and metallic bonding. Over half the atoms in the liquid were at interatomic distances resembling metallic bonds, but 48% were within the covalent bond distances. EDIP did not have as large of a gap as it saw interatomic distances at distances of 1.85 and 2.1 Å. The lack of a nice gap in the nearest neighbor histograms, the presence of possibly nonphysical loops, and double the percentage of coordination-1 dipoles compared to LCBOP could be indications that EDIP for carbon does not perform as well as LCBOP when studying liquid carbon.

3. ISOLATED CLUSTER ZERO KELVIN ATOMISTIC STUDIES

3.1. ISOLATED CLUSTER MODEL

3.1.1. Isolated Cluster Simulation Setup. A tiled-cube periodic boundary simulation is indicative of simulating an infinite crystal. The properties studied will represent bulk properties of the material. It is also interesting to study a system where interactions with the box sides is not a factor. The atoms can then move freely in space. This containerless setting, referred to as an isolated cluster for the purposes of this study, allows the liquid atoms to interact with less contributions from the environment.

The simulation setup is similar to that of the tiled-cube model, except instead of using periodic boundary conditions the simulation box is made large enough to be considered infinite in size. The simulation atom set was 100 atoms randomly placed with a nearest neighbor distance constraint of the Van der Waals radius. LCBOP was employed as the interatomic potential for the isolated cluster simulations. EDIP was unable to be used as in the current build of LAMMPS, the EDIP potential for carbon was unable to calculate an energy without the simulation code producing an error. Then the Polak-Ribiere version of conjugate gradient optimization was used for a zero-kelvin energy minimization. The simulation stopping parameters were 1,000 iterations or when the energy difference was 10^{-25} eV or less.

After energy minimization of the atoms, the final atom positions were taken for the 10 different atom sets and plugged into the ring formation, coordination statistics, and nearest neighbor histogram code. Along with determining the ring formation, coordination statistics, and nearest neighbor histograms, different models for space filling and Debye

scattering profiles were calculated from the final atom positions. The space filling models allow us to understand a preferred density for the liquid-like carbon in the containerless setting and a way to determine the containerless cluster grain size. The Debye scattering profiles allow a direct link to x-ray diffraction experiments.

3.1.2. Space Filling Models. The three space filling models were convex hull [103], ellipsoid [104-106], and Van der Waals space fill [107]. Convex hull is a method of geometry where a set of points in Euclidean space is defined to be convex if it contains the line segments connecting each pair of its points. The convex hull is then given by a set X which can be defined by four criteria: the minimal convex of X is unique, the intersection of all sets contains X , the set of all convex combinations of points contains X , and the union of all simplices with vertices contains X . For objects in three dimensions, the first criterion is enough to gauge the smallest possible convex bounding volume. With this volume, the density of the liquid-like carbon can be determined.

The ellipsoid model used here is a geometric technique of sphere packing where non-overlapping spheres are arranged within the ellipsoid space. We consider the carbon atom positions the position of each sphere with a radius of a carbon atom set to carbons Van der Waals radius. An ellipsoid envelope is then used to determine the optimal space filling. This model can construct approximate surface models for “frozen-liquid” systems like those represented by the isolated liquid carbon clusters. These clusters are expected to stay roughly ellipsoidal or even spherical. From such models, total volumes, approximate mass densities, and atom distances from the surface to distinguish bulk from surface atoms, can be calculated.

The Van der Waals space filling model stems from the concept of the Van der Waals surface. This model is an abstract representation of a molecule, illustrating where, in very rough terms, a surface might reside for the molecule based on the hard cutoffs of the Van der Waals radii. From this model, the space filling is done by representing the atoms by spheres that are allowed to overlap with carbons Van der Waals radius. This space fill model gives stable and sophisticated area, volume, and density values, especially for small and/or porous (non-convex) structures allowing for accurate modeling of the structure of the isolated liquid-like cluster.

3.1.3 Debye Scattering Profiles. Scattered intensity in powder diffraction patterns from gases, liquids, and randomly distributed nanoclusters in the solid state (to first order in kinematic approximation) can be done rather elegantly with the Debye scattering equation [108,109]. The Debye scattering equation is given as follows,

$$I_{powder}(\mathbf{q}) = \sum_{i=1}^N \sum_{j=1}^N f_i(\mathbf{q}) f_j(\mathbf{q}) \frac{\sin(\mathbf{q}r_{ij})}{\mathbf{q}r_{ij}}. \quad (3.1)$$

Here N is the number of atoms, $f_{i,j}(\mathbf{q})$ is the atom scattering factor for atoms I and j , r_{ij} is the distance between atoms I and j , and \mathbf{q} is the scattering vector ($\mathbf{q} = 2\pi\mathbf{g} = 2\pi/\mathbf{d}$) in reciprocal lattice distance units. The special period or interplanar spacing \mathbf{d}_{hkl} is associated with the reciprocal lattice vector \mathbf{g}_{hkl} . It should not be confused with the lattice vectors \mathbf{a} , \mathbf{b} , and \mathbf{c} . One can also use this to predict the effect of nano-crystallite shape on detected diffraction peaks, even if in some directions the cluster is only one atom thick [52,110,111]. These reciprocal space quantities can be related to the Bragg half-scattering angle θ_B by Bragg's law,

$$\frac{n\lambda q}{2\pi} \equiv n\lambda g \equiv \frac{n\lambda}{d} = 2 \sin[\theta_B]. \quad (3.2)$$

Following this model, Mathematica code was developed to give scattering power in “electron units”. This being the amount of classical scattering power a single free electron would provide which we adapted from Fultz and Howe [112]. Non-periodic objects will scatter with broad peaks and smoothly varying intensities called diffuse scattering. Modern x-ray synchrotron diffraction instruments are able to measure the diffuse scattering with good accuracy, using the so-called Total Scattering approach in which both Bragg (where there are present) and diffuse intensities are both measured over wide ranges of reciprocal space. This data may then be Fourier transformed to real space giving the atomic pair distribution function.

3.2. RESULTS AND DISCUSSION

To determine which n-member rings would be preferred nucleation seeds in a containerless setting, loop formation statistics were taken after energy minimization of the system using LCBOP. EDIP was unable to be used for this study as it would error due to the negligible environment effects that are the basis behind the potential’s framework. The 100 atom sets had their atoms randomly placed in a box with a nearest neighbor constraint of the Van der Waals radius of 1.7 Å for carbon. The box size was set large enough to be considered infinite in size compared to the local interactions between the particles. Table 3.1 shows an equal abundance of 5-member pentagons and 6-member pentagon formation. Though the total percentages are a bit lower than that seen in the tiled-cube infinite crystal simulations, having pentagons be preferred just as much as hexagons is more support for

pentagons being seeds for nucleation. The absence of 3- and 4-member loops is also another sign that these loops may be unstable or nonphysical for the carbon melt.

Table 3.1. LCBOP Isolated Cluster Loop Formation Statistics. 100 atoms in a containerless setting simulation box after energy minimization using the Polak-Ribiere version of conjugate gradient optimization and LCBOP interatomic potential.

LCBOP 100 Atom Loop Statistics (Isolated Cluster)					
n	3	4	5	6	7
100-vdwr-1	0	0	1	1	1
100-vdwr-2	0	0	2	1	1
100-vdwr-3	0	0	0	0	1
100-vdwr-4	0	0	1	0	2
100-vdwr-5	0	0	1	0	1
100-vdwr-6	0	0	0	2	1
100-vdwr-7	0	0	2	1	0
100-vdwr-8	0	0	2	2	1
100-vdwr-9	0	0	2	4	2
100-vdwr-10	0	0	2	2	0
Percentages	0.00%	0.00%	1.30%	1.30%	1.00%

After determination of the loop formations, the coordination statistics were generated to study the structure preference after minimization. Table 3.2 shows a high percentage of carbyne coordinated atoms similar to the infinite crystal simulations. The difference between the containerless setting that the infinite crystal is a lower percentage of graphene/graphite coordinated atoms. When comparing this to DFT studies done on low density carbon [26], carbyne chains dominate the structure preference. The presence of

these chains in the containerless setting and in the infinite crystal setting are giving support that the carbyne chains could be stable or meta-stable structures in the carbon melt.

Table 3.2. LCBOP Isolated Cluster Coordination Number Statistics. 100 atoms in a containerless setting simulation box after energy minimization using the Polak-Ribiere version of conjugate gradient optimization and LCBOP interatomic potential.

LCBOP 100 Atom Coordination Statistics (Isolated Cluster)					
Coordination Number	0	1	2	3	4
100-vdwr-1	6	25	43	25	1
100-vdwr-2	9	20	43	27	1
100-vdwr-3	6	33	47	13	1
100-vdwr-4	9	20	47	23	1
100-vdwr-5	2	28	51	18	1
100-vdwr-6	5	26	45	23	1
100-vdwr-7	3	30	49	16	2
100-vdwr-8	4	21	49	24	2
100-vdwr-9	7	23	38	27	5
100-vdwr-10	9	30	37	24	0
Totals Atoms per Coord-#	60	256	449	220	15
Percentage of Coord-#	6.00%	25.60%	44.90%	22.00%	1.50%

The nearest neighbor histograms for the containerless setting are showing a much wider gap than the infinite crystal tiled-cube histograms. Figure 3.1 shows for the containerless isolated cluster setting, covalent bond peaks are closer to the 1.42 Å bonds of graphene and graphite. The interatomic distance that corresponds to metallic bonding is roughly 2.3 Å which is slightly longer than the 2.1 Å seen for the infinite crystal setting. Also seen in Figure 3.1, the peak representing the graphene covalent bond length of 1.42 Å is highest for sets 1, 2, 3, 5, 7, and 8. This indicates for six of the ten simulations, the

containerless isolated cluster had a high preference for graphene/graphite bond distances after energy minimization.

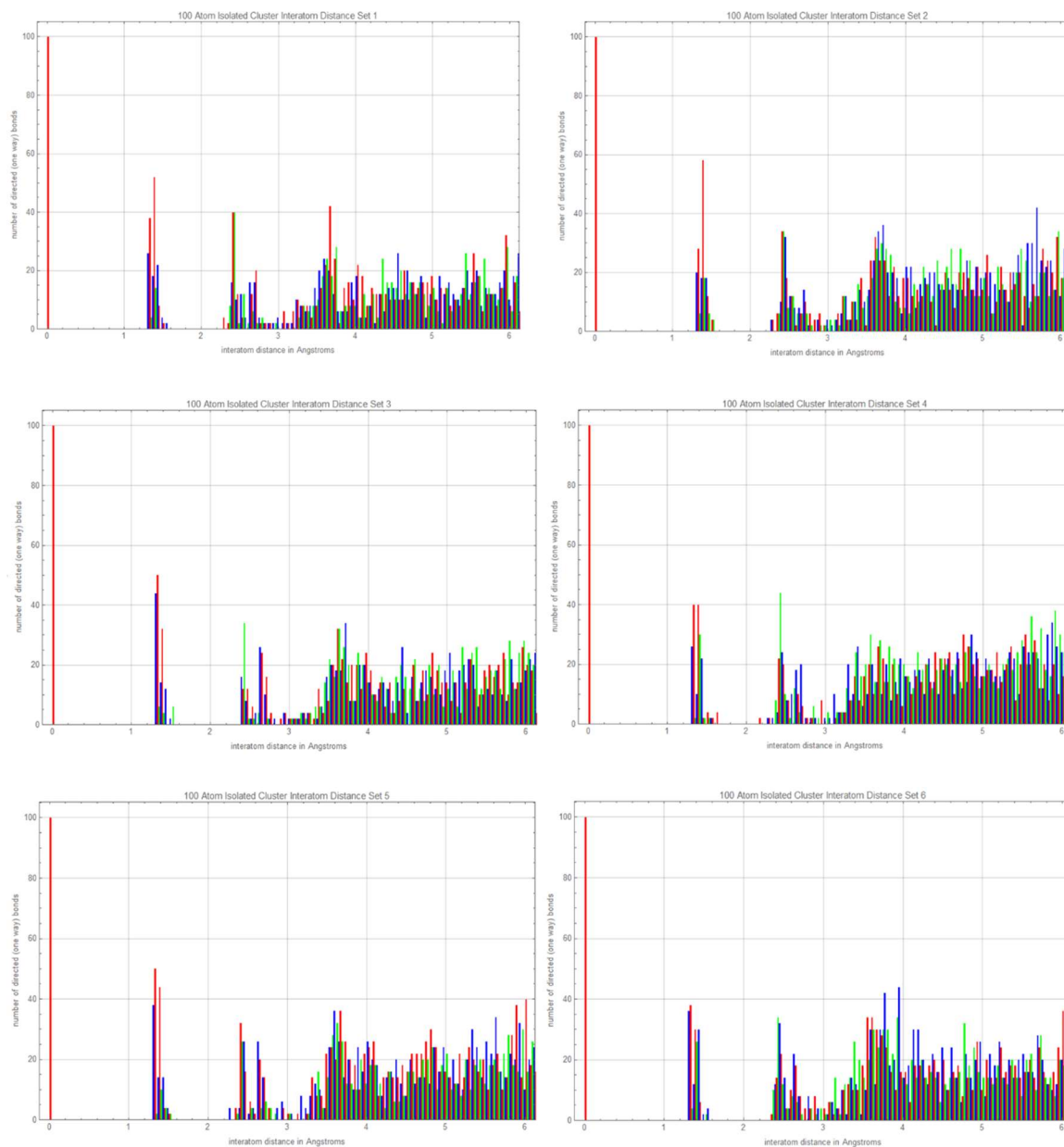


Figure 3.1. Isolated Cluster Nearest Neighbor Histograms. 10 sets of 100 atom isolated cluster zero kelvin energy minimizations. A noticeable gap from 1.42 to 2.3 Å can be seen in all 10 sets. Sets 1, 2, 3, 5, 7, and 8 show highest peaks at the graphene covalent bond distance of 1.42 Å.

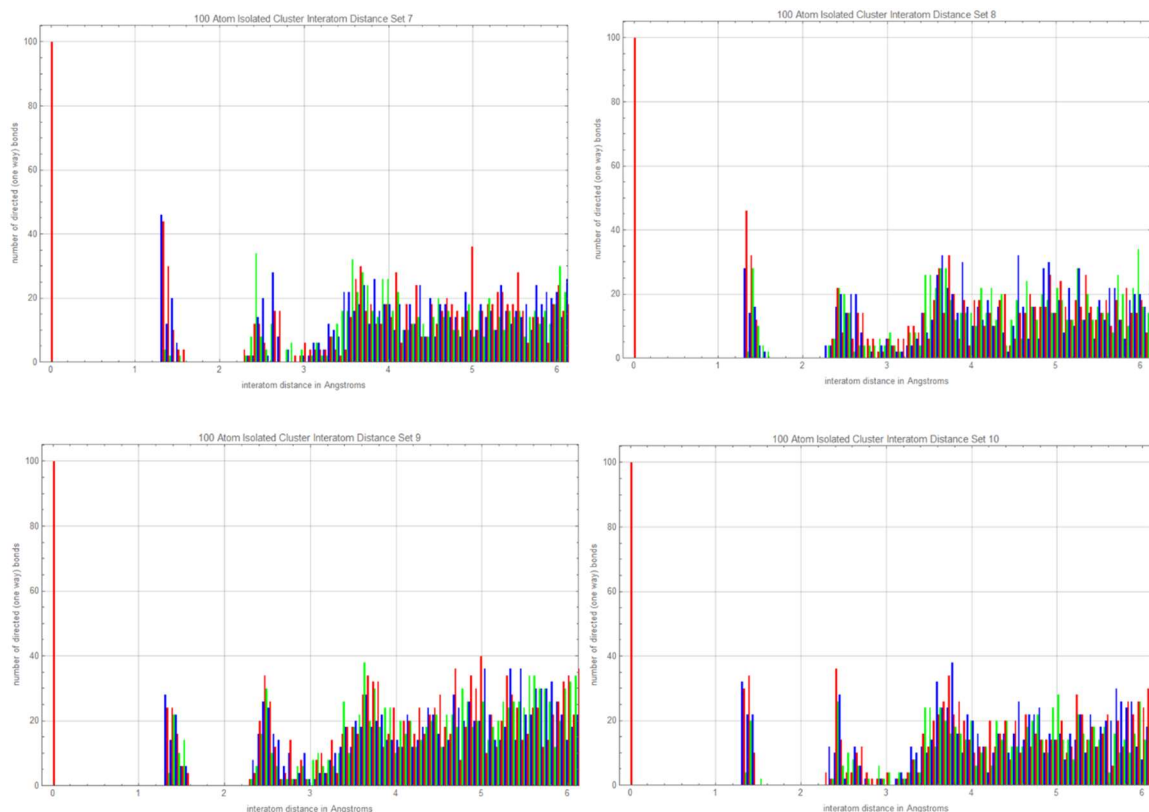


Figure 3.1. Isolated Cluster Nearest Neighbor Histograms. 10 sets of 100 atom isolated cluster zero kelvin energy minimizations. A noticeable gap from 1.42 to 2.3 Å can be seen in all 10 sets. Sets 1, 2, 3, 5, 7, and 8 show highest peaks at the graphene covalent bond distance of 1.42 Å. (Cont.)

Energy minimization in the containerless setting gives a situation which does not give direct information of the system density. Since the atoms are freely moving, models for space filling can be used to study the preferred density of the atoms within the “frozen-liquid”. Three different space filling approaches were used to gauge the density for our relaxed atom positions: convex hull, ellipsoid, and Van der Waals. Table 3.3 shows the output from the three different models when applied to a single set of atoms. These models are able to give information on surface area, volume, mass density, equivalent diameter, and grain size. For the case shown here, the convex hull and Van der Waals space fill give similar density values and are much higher than predicted by the ellipsoid model.

Table 3.3. Isolated Cluster Space Filling Model Output. Convex hull, ellipsoid, and Van der Waals space filling models when applied to the positions of 100 atom isolated cluster after energy minimization.

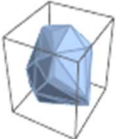
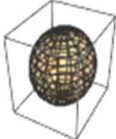
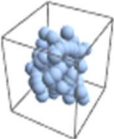
	convex hull model	ellipsoid model	vdw spacefill
three-dimensional graphic			
surface area A in \AA^2	636.458	757.456	1593.46
volume V in \AA^3	1322.68	1944.09	1315.02
mass density in grams/cm ³	1.50652	1.02497	1.5153
'eq. diameter' $1.24V^{1/3}$ in \AA	13.6192	15.4848	13.5929
'grain size' $6V/A$ in \AA	12.4691	15.3997	4.95157

Table 3.4. Isolated Cluster Preferred Density Statistics. Convex hull, ellipsoid, and Van der Waals space filling models of 100 atom isolated cluster energy minimization simulations.

LCBOP 100 Atom Density Statistics (g/cc)			
Model	Convex Hull	Ellipsoid	Van der Waals
100-vdwr-1	1.12	0.81	1.63
100-vdwr-2	1.12	0.81	1.63
100-vdwr-3	1.31	0.917	1.51
100-vdwr-4	1.57	1.12	-
100-vdwr-5	1.85	1.14	1.59
100-vdwr-6	1.76	1.21	-
100-vdwr-7	1.47	1.01	1.56
100-vdwr-8	1.51	0.96	1.67
100-vdwr-9	1.99	1.48	1.63
100-vdwr-10	1.51	1.02	1.51
Average Density	1.52	1.05	1.59
Density Standard Deviation	0.28	0.19	0.06

The space fill modelling was applied to all 10 sets of 100 atom isolated cluster energy minimizations. From the information gained, the preferred density was of high interest as it can tell us if the “frozen-liquid” system is preferring densities that correspond to liquid-like carbon melts. Table 3.4 shows the determined density values from the three space filling models for each set of energy minimizations. For all sets of data, the ellipsoid model gives the lowest density values with a majority being on the order of 1 g/cm³. For some of the cases, the convex hull and Van der Waals models give similar density values near their respective average values of 1.52 and 1.59 g/cm³. Most of the time though, the density values vary by 0.2 to 0.5 g/cm³.

Standard deviation analysis of the densities also shows the convex hull model gives the largest standard deviation. This is most likely due to the atomic structures not always being convex which can allow for larger errors in the calculation of the density. The errors in the convex hull model also shows up in independent DFT studies. A couple of the data sets were unable to determine a density with the Van der Waals model. This was most likely due to the presence of carbyne chains poking out from local ordering of the atoms causing an extremely complex volume which the code could not calculate. Even with these missing calculations, the Van der Waals model gave the most consistent density calculation with the lowest standard deviation. From the data here, the Van der Waals method gave a more stable and accurate determination of the isolated cluster preferred atom density of 1.59 ± 0.06 g/cm³. The Van der Waals and convex hull models show agreement with estimated density values of ~ 1.5 g/cm³ of the liquid core of lab grown graphite onions [52,113]. There is an expansion as the density drops from the beginning 1.72 g/cm³, but

the overall preferred density after energy minimization still falls within the expected density range for liquid carbon.

The surface fill models do a good job of giving an understanding of the preferred density as well as allowing for the determination of the grain (or cluster) size for the different containerless clusters. The grain size is determined from the surface to volume ratio via $D \equiv 6V/A$. Table 3.5 shows that statistics of the grain size for all 10 containerless setting sets. Of the three models, the Van der Waals model gives a grain size much smaller than the convex hull and ellipsoid models. The convex hull and ellipsoid models have closer agreement on the grain size, but when compared to work done in lab-grown specimens [52,113] the Van der Waals model comes closest. Lab-grown specimens see cluster sizes near 6 \AA which is closest to the average value generated by the Van der Waals space fill of $5.19 \pm 0.24 \text{ \AA}$. The Van der Waals model also has the smallest standard deviation of the three models.

When comparing to the initial (unrelaxed) atom set, the convex hull and ellipsoid model show an increase in grain size, where the Van der Waals sees a shrink from 7.19 \AA to $5.19 \pm 0.24 \text{ \AA}$. The difference in how the models calculate the surface area and volume can be attributed to the vastly different grain size calculations. For the convex hull and ellipsoid models, the volume during energy minimization nearly doubles, but the surface area only slightly increases. For the Van der Waals model, the volume increases much less than the surface area. The decreasing density and grain size comes from the rearrangement of atoms between surface and bulk. The more sophisticated model for volume and area from the Van der Waals model provides more accurate values of grain size and density which agree with lab-grown specimens.

Table 3.5. Isolated Cluster Grain Size Statistics. Convex hull, ellipsoid, and Van der Waals space filling models of 100 atom isolated cluster energy minimization simulations.

LCBOP 100 Atom Grain Size Statistics (Å)			
Model	Convex Hull	Ellipsoid	Van der Waals
100-vdwr-1	13.03	16.42	5.03
100-vdwr-2	13.30	16.42	5.03
100-vdwr-3	12.51	15.87	4.84
100-vdwr-4	12.18	14.63	-
100-vdwr-5	11.30	14.73	5.32
100-vdwr-6	11.88	14.43	-
100-vdwr-7	12.13	14.95	5.36
100-vdwr-8	11.55	15.24	5.40
100-vdwr-9	11.35	13.46	5.55
100-vdwr-10	12.47	15.40	4.95
Average Grain Size	12.17	15.16	5.19
Grain Size Deviation	0.64	0.88	0.24

With the preferred density and grain size data determined, Debye scattering profiles were generated to investigate signs of structure of the containerless setting isolated cluster. Figure 3.2 shows the generated Debye scattering profile for all 10 studied atom sets. Each set of energy optimized atom sets are showing a peak in their Debye profiles at the (100) graphite Miller index. The peaks are broad due to the small size of the clusters. The absence of the (200) peak which corresponds to the $1/3.4 \text{ \AA}$ spacing of the graphite layers is evidence that the structure of the containerless cluster is resembling more of a graphene than graphite structure. The low frequency peaks before the (100) peak for graphite is from the amorphous liquid atoms. We also see the presence of the liquid from the slight wave in the tail of the scattering profiles. The Debye profiles along with the density calculation from the Van der Waals space fill are showing preference for graphene structure and agree with previously observed lab-grown cores.

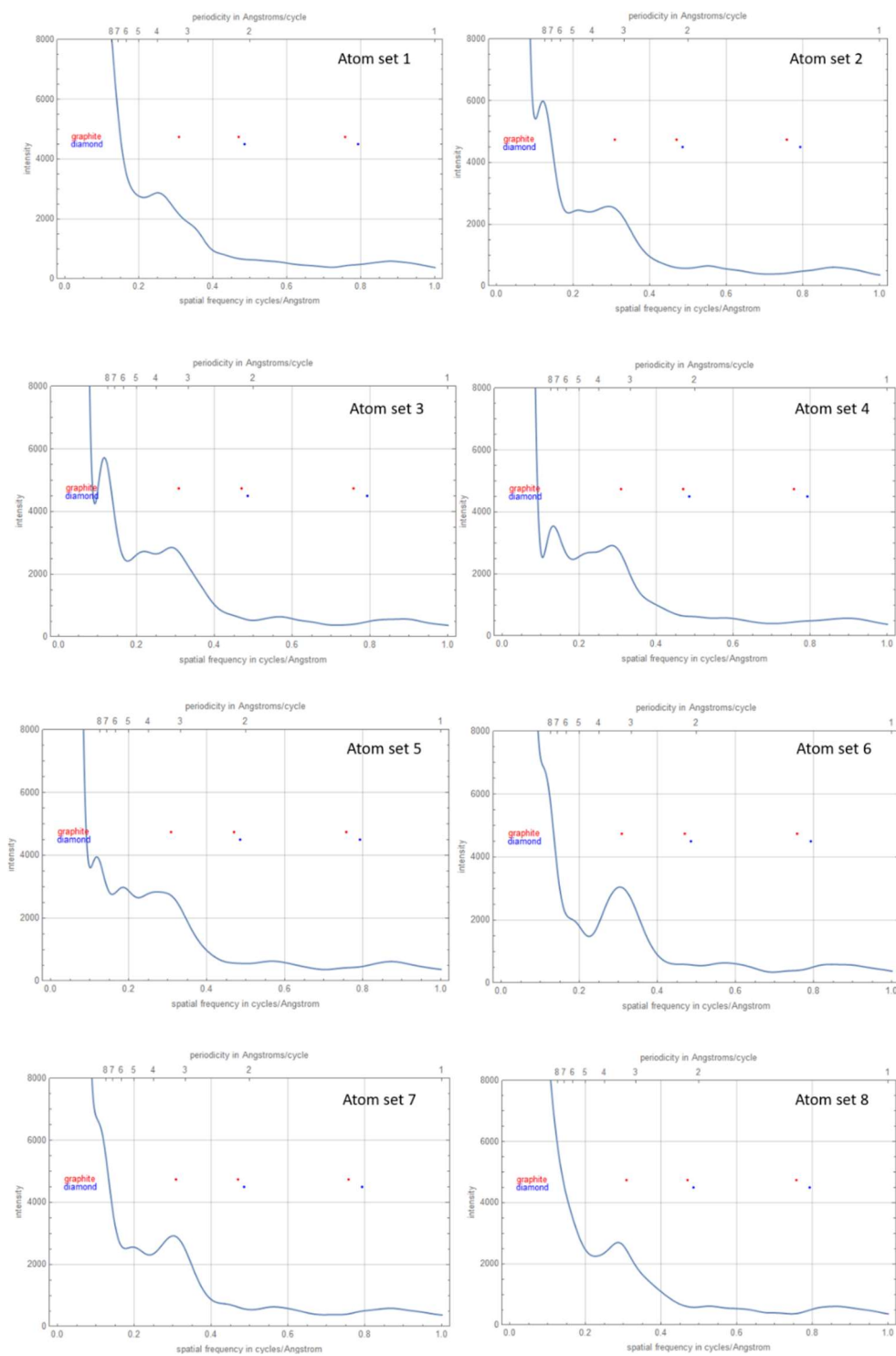


Figure 3.2. Debye Scattering Profiles. 100 atom isolated cluster relaxations. Red dots indicate (100), (110), and (200) graphite Miller indices. Blue dots indicate the (111) and (220) diamond Miller indices.

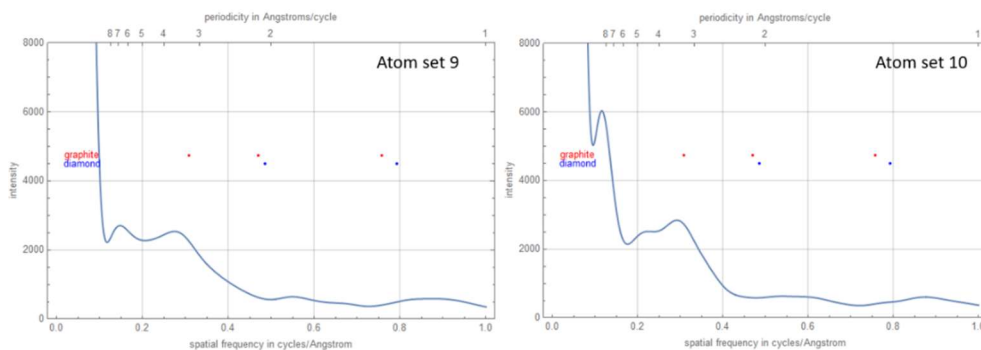


Figure 3.2. Debye Scattering Profiles. 100 atom isolated cluster relaxations. Red dots indicate (100), (110), and (200) graphite Miller indices. Blue dots indicate the (111) and (220) diamond Miller indices. (Cont.)

3.3. CONCLUSION

In this section the LCBOP semi-empirical potential for carbon was used to simulate isolated clusters of 100 carbon atoms randomly placed with a nearest neighbor distance constraint of the carbon Van der Waals radius. Unlike the tiled-cube infinite crystal studies, the EDIP potential was not able to be used here to compare the two long range models as the high dependence on environmental effects of EDIP caused the potential to error during the simulations. Zero kelvin energy minimizations using the Polak-Ribiere version of conjugate gradient optimization was done to find an optimum energy configuration for the atoms. With the relaxed atom positions, n-member loop formation statistics, coordination statistics, density and grain size statistics from different space fill models, and Debye scattering profiles were generated.

The n-member loop formations were showing similar results to the tiled-cube infinite crystal studies with pentagonal 5-member loops forming just as much as hexagonal 6-member loops. This gives more support that pentagonal 5-member loops are just as likely

to be nucleation seeds for liquid carbon. The coordination statistics show a high percentage of carbyne sp -coordination which agrees with previous computational studies of low-density carbon. The presence of graphene/graphite sp^2 -coordination with the presence of pentagonal loop formation is another indication of the pentagon-first mechanism from Y-junction carbyne chains. Both the infinite crystal and containerless settings are showing evidence of pentagons being possible nucleation seeds which agrees with independent DFT studies.

Convex hull, ellipsoid, and Van der Waals space fill models were used with the atom positions to determine the preferred density and grain-size after energy minimization. When determining the density of the containerless setting isolated clusters, the ellipsoid model generated a much smaller density compared to the other two. For a select few atom sets, the convex hull and Van der Waals models were in close agreement on density and their respective averages were close in value as well. The standard deviation in the density showed the Van der Waals model gave a more precise and stable estimate for the density of the cluster. Though the convex hull model has a bigger standard deviation, it and the Van der Waals model estimates agree with density observations of liquid cores of lab grown graphite onions. The determination of the grain size looked at the surface to volume ratio. During energy minimization the models estimated the volume changes differently. The convex hull and ellipsoid estimated a volume change of nearly double, but the surface area only slightly increased. The Van der Waals model had the volume increase much less than the surface area. Comparing the average grain size values and their standard deviations the Van der Waals model comes closest to observed lab-grown cluster sizes in a containerless setting. The more complex and sophisticated determination of volume and

surface area gives a more accurate representation of the grain-size than the other two models.

Debye scattering profiles, which can be directly related to x-ray diffraction experiments, were generated from the atom positions of each energy minimized atom set. Each set sees a peak at the (100) graphite index. The peak is broad due to the small size of the cluster and low-frequency peaks from the amorphous liquid are present. For a select few sets, the low-frequency peak is negligible or completely absent giving a large peak at the (100) index. This peak with the absence of the (200) interplanar $1/3.4 \text{ \AA}$ spacing peak is showing the containerless “liquid-like” minimized atom positions are preferring a graphene structure. The wave-like features at the tail of the Debye profile are also indicative of a liquid-like structure showing a preference for a liquid state in a containerless low-density and pressure setting.

PAPER**I. THE RATES OF UNLAYERED GRAPHENE FORMATION IN A SUPERCOOLED CARBON MELT AT LOW PRESSURE**

Philip Chrostoski, Chathuri Silva, P. Fraundorf
Department of Physics and Astronomy
University of Missouri – St. Louis
St. Louis, MO 63121

ABSTRACT

Elemental carbon has important structural diversity, ranging from nanotubes to graphite and diamond. Studies of primitive meteorite extracted micron-size core/rim carbon spheres suggest they formed via the solidification of condensed carbon-vapor droplets, followed by gas-to-solid carbon coating to form the graphite rims. We show here how analytical models of reaction limited nucleation & growth can be used to connect thermal history (e.g. time at temperature) to electron microscope observations of mean graphene sheet size and number density. Atomistic models using the LCBOP semi-empirical potential show promise for estimating latent heat and the temperature-dependence of barrier heights, which are not yet incorporated in the model. We also show that growth of 2D clusters from a 2D liquid takes place more rapidly than from a 3D liquid, which with suitable scaling might open the door to simulating growth over millisecond time scales in the study of liquid carbon's solidification at low pressures.

1. INTRODUCTION

Liquid carbon has been difficult to study experimentally due to the high temperature and pressure levels needed for formation. Requirements such as high pulsed laser heating of diamond-like carbon or graphite along with immediately measuring the rapidly expanding and boiling liquid phase are not trivial for experiment [1-9]. After cooling to ambient temperatures, a wide variety of structures have been reported to form; nanoclusters of diamond and graphite [10], carbyne chains [11], and novel super-dense phases [12]. This has given rise to the desire to study liquid carbon computationally [13-20]. The *Long-Range Carbon Bond Order Potential* (LCBOP) was created to begin studies into liquid carbon phases [21]. This has led us to employ LCBOP in our studies of the nucleation and solidification of liquid carbon.

Micron-size core/rim carbon spheres extracted from primitive meteorites have recently inspired some interesting results on the condensation of liquid carbon at low pressure, as well as its subsequent solidification. The submicron graphite-coated spheres observed via transmission electron microscopy imaging and diffraction have shown to contain unlayered graphene [3-9]. Electron phase contrast imaging of edge-on sheets has moreover suggested the presence of faceted penta-cones. This, and subsequent laboratory synthesis work [3-7], suggest that carbon vapor at low pressure condenses first as liquid droplets which, if cooled slowly, form unlayered graphene sheets in an otherwise disordered matrix. Experimental densities are on the order of 1.8 g/cm^3 at ambient pressure after solidification [4,8].

The environments in which both specimens were formed also were likely well under atmospheric pressure (10^{-3} and 10^{-8} bars).

We report on here a first pass at semi-empirical modelling of liquid-carbon solidification, using data from electron microscope study of pre-solar and lab grown “cores”. In particular, we build “few-parameter” models of graphene sheet nucleation and growth. The nucleation model builds on the classic analytical model of Turnbull and Fischer [22], although we have not yet included temperature dependence for the activation energies (which we hope will eventually provide insight into the supercooling threshold which triggers nucleation). Similarly, the growth model uses a single fixed activation energy, starting with a 6-atom critical nucleus even though independent DFT and experimental work suggest that 5-atom rings are active nucleation sites as well [23].

2. COMPUTATIONAL METHODS

Nucleation model: Following the classic paper by Turnbull and Fisher [22] we model the time (t) rate at which the number density (η) of nuclei per unit volume increases with an expression of the form,

$$\frac{\delta\eta}{\delta t} \cong \left(\frac{k_B T}{h}\right) e^{\left[-\frac{(\Delta f^* + \Delta F^*)}{k_B T}\right]} \eta_0 t, \quad (1)$$

where k_B is the Boltzmann constant, T is the temperature, h is Planck’s constant, Δf^* the free energy of activation for short range travel across the interface to the new phase, ΔF^* is the free energy needed to create a critical-size cluster, and η_0 is the number of carbon

atoms per unit volume in the liquid. We report here on a *nominally fixed* value for the sum Δf^* and ΔF^* at 8.36 eV, which may seem large until one realizes that for 2D growth ΔF^* is inversely proportional to the supercooling increment ΔT , and so becomes quite large as temperature increases.

Growth model: Considering 2D growth at sheet edges only, we begin by modelling a sheet as a circle with radius r . The number of atoms is written as $n \approx \sigma\pi r^2$, where the number of atoms per unit area in a graphene sheet is $\sigma \approx 3.82 \times 10^{15}/\text{cm}^2$. The rate of atom-addition at a given temperature is presumed proportional to the length of the perimeter ($p \approx 2\pi r = 2\pi\sqrt{n/\pi\sigma} = 2\sqrt{\pi n/\sigma}$) immersed in the growth liquid. Since the amount of perimeter is proportional to the square root of the area, the differential growth equation will take the form,

$$\frac{\delta n(t)}{\delta t} = \left(\frac{\delta n/\delta t}{p} \right) p = a\sqrt{n(t)}. \quad (2)$$

The proportionality constant $a = 2\sqrt{\pi/\sigma} \frac{\delta n}{p\delta t}$, is the rate of atom addition per unit perimeter at a given temperature, for whose temperature dependence we add a Turnbull-Fischer type attempt rate and Boltzmann activation energy factor that can be calibrated empirically. At fixed temperature, the solution to this first-order differential equation under the initial condition that the “critical” starting seed size is $n(0) = b$ is quadratic in time with the form,

$$n(t) = b + a\sqrt{bt} + \left(\frac{at}{2} \right)^2. \quad (3)$$

Individual carbon loops are plausible nucleation seeds given their tight binding energies, and here we choose b as nominally 6. This may later be adapted to changing effects of edge curvature, possible nucleation on pent loops, shape changes during growth and more.

We combine nucleation and 2D growth by monitoring the distribution of cluster sizes as a function of time during a constant temperature anneal. Using discrete time steps, new small nuclei are added to the distribution after the existing nuclei are grown by an amount appropriate to the time step involved. We then calculate two curves: One for time to nucleate a fixed number of sheets per unit volume, and the second for time to grow a distribution of sheets to a mean size, as a function of temperature. This general approach allows us to look for intersections between number-density and mean-size curves for the two experimental specimen types in hand.

Atomistic modeling: For atomistic work we employ LCBOP using Sandia's *Large-scale Atomic/Molecular Massively Parallel Simulator* (LAMMPS). The binding energy of the LCBOP semi-empirical potential [21] can be written as follows,

$$E_b = \frac{1}{2} \sum_{i,j}^N V_{i,j}^{tot} = \frac{1}{2} \sum_{i,j}^N (f_{c,ij} V_{ij}^{SR} + S_{ij} V_{ij}^{LR}). \quad (4)$$

Here the total pair potential, $V_{i,j}^{tot}$, is the sum of the short-range interactions, $f_{c,ij} V_{ij}^{SR}$, and the long-range interaction, $S_{ij} V_{ij}^{LR}$. For the short-range interaction, $f_{c,ij}$ is a smooth cut-off function where for the long-range interaction, S_{ij} is a switching function that excludes first neighbours. Our heat treatments used the same temperature range as our analytical model

on a 100-atom liquid with 42 of those atoms forming a graphene sheet to determine the growth in both 2D and 3D.

3. RESULTS

Figure 1 shows the rate that nuclei/cc are formed over time at different temperatures predicted by our nucleation model. The increase is linear at fixed temperature, until the supply of unprecipitated carbon atoms grows short. We cannot yet predict solidification times from this plot because the temperature dependence of the nucleation barrier is not yet considered. Horizontal lines denote experimentally observed number densities of grown graphene sheets [23], from which we have inferred densities of grown nuclei after recognizing that pent-loops can each nucleate 5 flat sheets while hex-loops nucleate only one.

Figure 2 allows us to address the second problem, namely the requirement of time to grow to the observed size, by combining nucleation and growth to determine the solidification time as temperature increases. Intersection points between the nucleation and growth curves suggest self-consistent values of time and temperature for solidification. Extending our nucleation model to include the temperature dependence of barrier height therefore shows promise for allowing one to infer thermal history (e.g. time at temperature during solidification) from observed microstructure (e.g. average cluster size and number per unit volume), and vice versa.

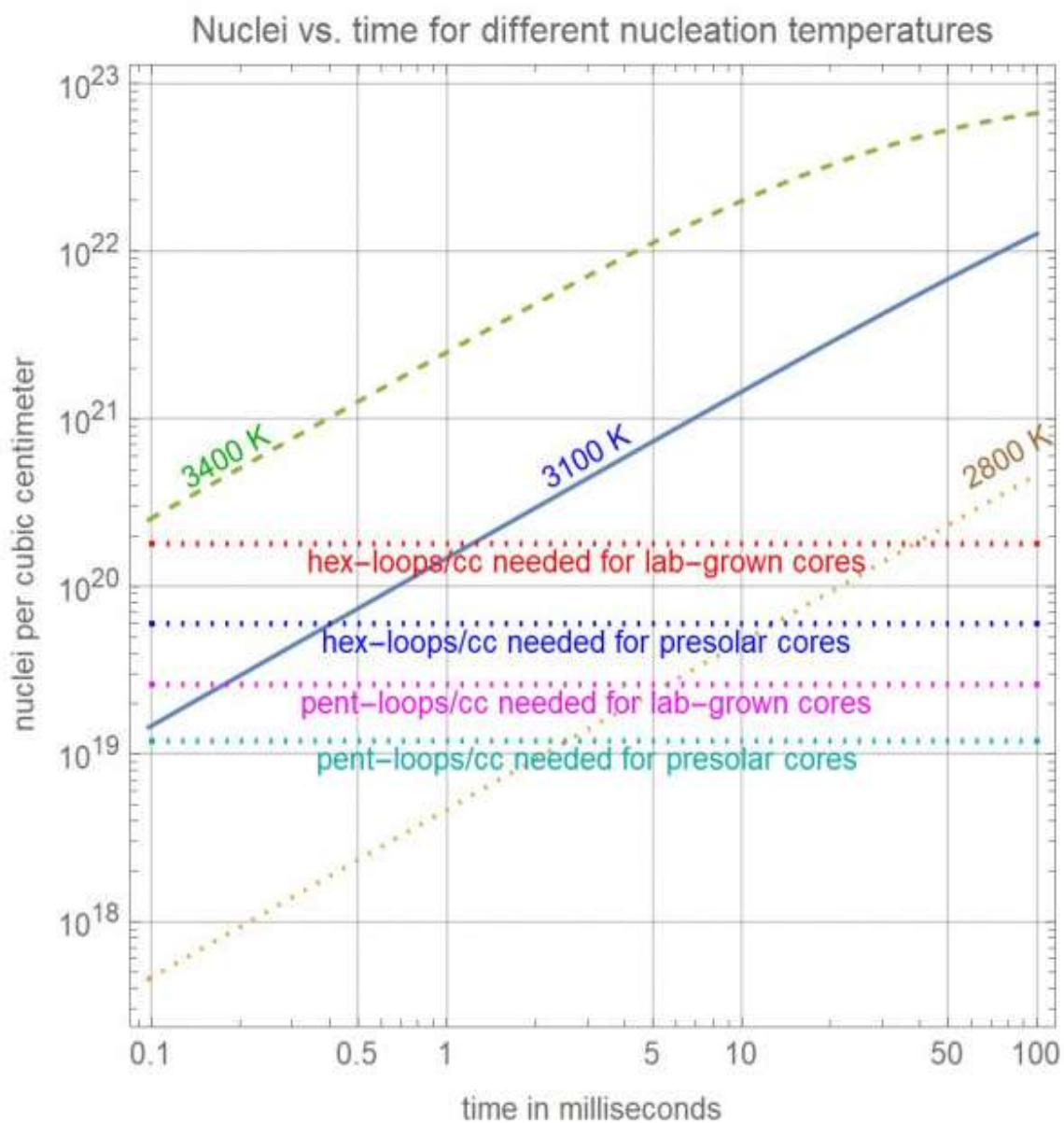


Figure 1. Zeroth-Order Nucleation at Different Temperatures. Nuclei/cc as a function of time at different temperatures; dotted is 2800 K, solid blue 3100 K, and dashed orange 3400 K. The lines across denote sheet density levels: (a) in lab-grown cores if from hex-loops (red) or from pent-loops (magenta), and (b) in presolar cores if from hex-loops (blue) or from pent-loops (cyan).

First pass at unlayered graphene solid nucleation/growth model
 time increasing presolar (blue) saturation effects are ignored

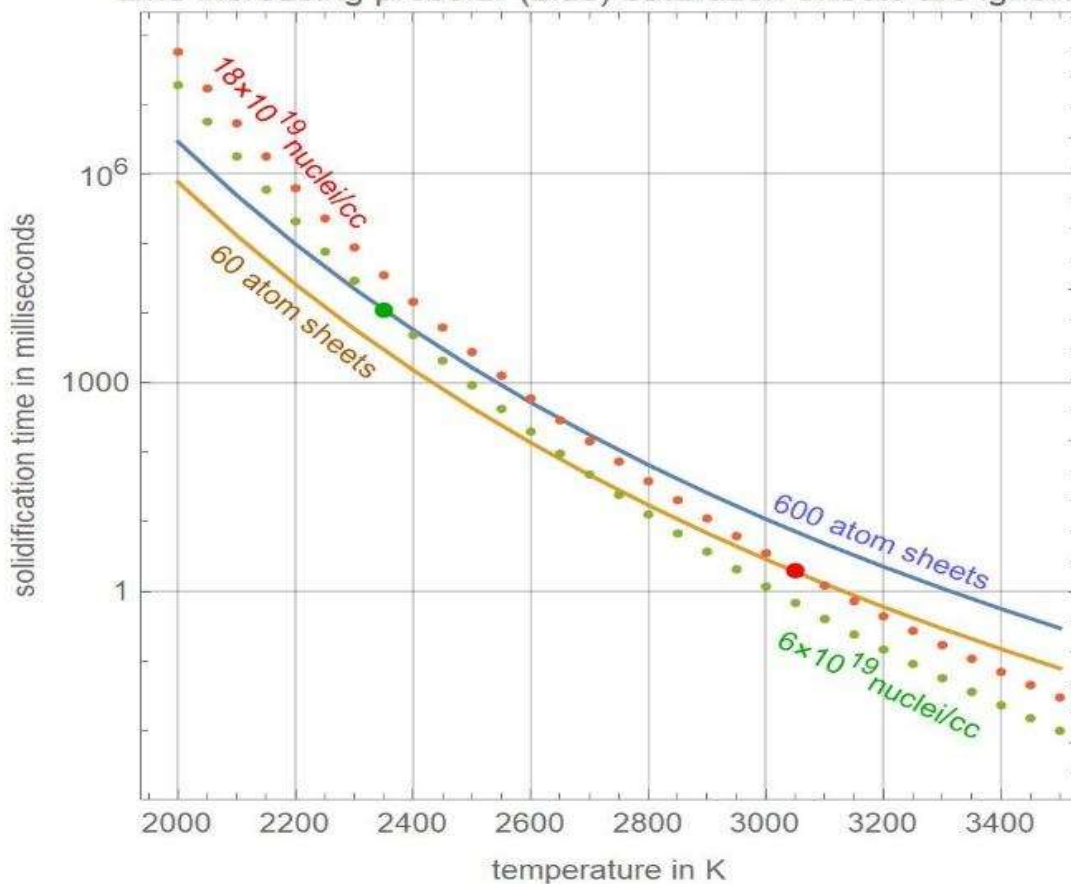


Figure 2. Zeroth-Order Solidification Times as a Function of Temperature. The solid lines denote times (as a function of fixed temperature) to grow 600-atom (blue) and 60-atom (orange) graphene sheets from a supercooled droplet at low pressure (neglecting saturation effects). The intersection (large green dot) of the per-solar nucleation model (small green dots) curve with the pre-solar blue 600-atom curves likewise connect (large red dot with the nucleation model curve (small red dots) for the higher observed lab-grown core number density.

Use of atomistic simulations, to explore energy differences (including latent heats and barrier heights) as well as growth rates at temperature, are a second part of our strategy. The challenge is that solidification times in the millisecond or larger time frame may be

involved, even though simulation time intervals begin in the femtosecond range. This is consistent with the lack of graphene sheet growth from a 3D liquid during 20 nanosecond LCBOP molecular dynamic anneals at temperatures in the range from 2400K to 3400K.

To address this issue, we explore a possible scaling advantage for growing a 2D graphene sheet from a 2D rather than a 3D liquid. Figure 3 shows the final sheet atoms after the 20 nanosecond LCBOP heat treatments of a 100-atom “liquid-like” carbon with 42 atoms in the form of a 13-loop graphene sheet. The simulation was done by forcing all forces and movement along the z-axis to be zero.

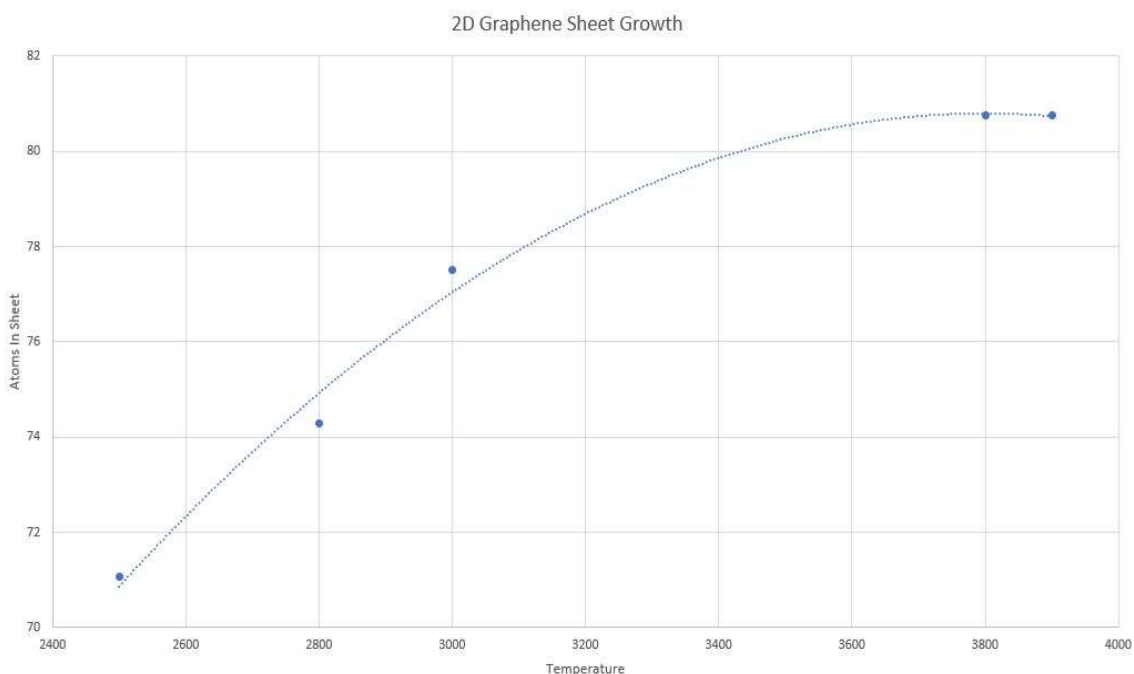


Figure 3. Atomistic 2D Graphene Sheet Atoms as a Function of Temperature. Final number of atoms in graphene sheet versus temperature, after a two-dimensional LCBOP heat treatment over 20 ns time integration of 100-atoms including a 42 atom (13-loop) graphene sheet. The dotted line is a spline fit to the data.

If at around 3000K it takes e.g. a tenth millisecond to grow 60-atom sheets from a 3D liquid in the lab, but it takes only 20 nanoseconds to grow roughly 70-atom sheets from a 2D liquid in LCBOP, this suggests that scaling relations for growth of 2D structures from a reduced dimensionality liquid may provide insight into growth from a higher dimensional liquid with less computer time doing molecular dynamics. Regardless, LCBOP calculations show promise for checks on latent heat of fusion and temperature-dependent barrier height extension of these models.

4. DISCUSSION

We describe here a strategy for semi-empirically modelling the solidification of a carbon melt at low pressure, based on observational data from the cores of carbon spheres formed in cool giant star atmospheres, as well as in the laboratory. The strategy as outlined appears robust, but so far, we have limited the number of parameters used in the modelling. We have not included a temperature dependence for the barrier height to nucleation, for which atomistic estimates of latent heat of phase transition and barrier heights to reaction may be crucial.

We have also shown that atomistic simulations for the growth of 2D structures in a 2D instead of 3D liquid might allow for molecular dynamics simulation of longer time periods, provided that suitable scaling relations for the switch from 2D to 3D can be identified. The atomistic method was able to get good growth of a graphene sheet when restricting the simulation to 2D by zeroing out forces along the z-axis.

5. CONCLUSION

Recent laboratory observations of micron-size carbon spheres, with cores containing randomly oriented and unlayered graphene sheets embedded in a frozen liquid matrix obtained by the cooling of a carbon vapor, open the door to experimental work on liquid carbon at low pressures. In this paper, we describe a strategy for relating the observed size and number density of these unlayered graphene sheets to analytical models for sheet nucleation and growth from the carbon melt.

The nucleation and growth models examined so far have a minimum of empirical parameters. We see at higher temperatures less time is needed to generate enough 5/6-atom loop seeds to agree with lab-grown and pre-solar core observations but at lower temperatures more time is needed to generate enough 6-atom loop seeds. This first pass zeroth order model may be pointing to 5-atom pent loops being the more abundant nucleation seed in our lab grown and pre-solar observations. Atomistic simulations (both LCBOP/semi-empirical and VASP/ab-intio) show promise for expanding those parameter sets, and eventually connecting observed structures to thermal history of the solidification process.

Our understanding of the super-cooling threshold for solidification (which may in carbon's case be even higher than that for liquid metals in containerless settings [24]) may emerge from this exploration. Extensions of the models are still needed, however, to the temperature dependence of the nucleation threshold, and to the switch from the effects of "time at temperature" to effects of a given "cooling rate". Though our current understanding of the pressure-effects to nucleation is limited, atomistic studies to

determine the latent heat of fusion is showing negligible dependence on pressure. More studies into the effects of pressure will be needed to determine the effect of pressure on our analytical models. In addition to the larger ramifications, this work is of immediate relevance to studies of carbon condensation in cool giant star atmospheres, and to the possible laboratory synthesis of “unlayered graphene solid” with unprecedented properties as a diffusion barrier.

ACKNOWLEDGEMENT

The atomistic calculations, analytical modelling, and manuscript writing was done by PC, the DFT calculations were done by CS, and the pre-solar and lab grown observations, analytical modelling and program writing, and manuscript writing was provided by PF. We thank the Missouri Space Grant for funding this research and Missouri S&T for access to the Forge cluster supercomputer to do the atomistic calculations.

REFERENCES

1. D. Kasuya, M. Yudasaka, K. Takahashi, F. Kokai and S. Iijima, *J. Phys. Chem. B* **106**, 4947-4951 (2002).
2. W. A De Heer, P. Poncharal, C. Berger, J. Gezo, Z. Song, J. Bettini and D. Ugarte, *Science* **307**:5711, 907-910 (2005).
3. P. Fraundorf and M. Wackenhut, *Ap. J. Lett.* **578** (2): L153-156 (2002).
4. P. Fraundorf, T. Hundley and M. Lipp, *HAL-02238804* (2019).
5. T. J. Hundley, P. Fraundorf, *49th Lunar and Planetary Science Conference 2018 (LPI Contrib. No. 2083)*, 2154-2155 (2018).
6. P. Fraundorf, M. Lipp, T. Hundley, C. Silva and P. Chrostoski, *Microscopy and Microanalysis* **26**: S2, pp. 2838-2840 (2020).

7. P. Fraundorf, S. Chathuri, P. Chrostoski and M. Lipp, *COSPAR 2021 Sydney, International Council of Scientific Unions Committee on Space Research*, (2021), .
8. T. Bernatowicz, R. Cowsik, P. C. Gibbons, K. Lodders, B. F. Jr., S. Amari, and R. S. Lewis, *Astrophysical Journal* **472**, 760 (1996).
9. P. Fraundorf, K. Pisane, E. Mandell and R. Collins, *Microscopy and Microanalysis* **16** Supplement **2**, 1534-1535 (2010).
10. C. C. Yang and S. Li, *J. Phys. Chem. C* **112**, 1423-1426 (2008).
11. C. Cannella and N. Goldman, *J. Phys. Chem* **119**, 29-31 (2015).
12. M.S. Dresselhaus, G. Dresselhaus and P.C. Eklund, *Science of Fullerenes and Carbon Nanotubes*, (Academic Press, San Diego, CA, 1996).
13. P. E. Blöchl, *Phys. Rev. B* **50**, 17953 (1994).
14. J.P. Perdew, K. Burke, and M. Ernzerhof, *Phys. Rev. Lett.* **77**, 3865 (1996).
15. D. S. Franzblau, *Phys. Rev. B* **44**, 4925 (1991).
16. V. L. Deringer and G. Csányi, *Phys. Rev. B* **95**, 094203 (2017).
17. C. Toh, H. Zhang, J. Lin, A. S. Mayorov, Y. Wang and C. M. Orofeo, *Nature* **577**, 199-203 (2020).
18. J. R. Morris, C. Z. Wang, and K. M. Ho, *Phys. Rev. B* **52**, 4138 (1995).
19. C. J. Wu, J. N. Glosli, G. Galli, and F. H. Ree, *Phys. Rev. Lett* **89**, 135701 (2002).
20. N. A. Marks, N. C. Cooper, and D. R. McKenzie, *Phys. Rev. B* **65**, 07541, (2002).
21. J. H. Los and A. Fasolino, *Phys. Rev. B* **68**, 024107 (2003).
22. D. Turnbull and J. C. Fisher, *J. Chem. Phys.* **17**, 71 (1949).
23. C. Silva, P. Chrostoski, and P. Fraundorf, *MRS Advances* **6** (7), 203–208 (2021).
24. K. Kelton and A. L. Greer, “*Nucleation in condensed matter: applications in materials and biology*”, Elsevier (2010).

SECTION

4. TEMPERATURE ANNEALS OF LIQUID CARBON

4.1. HEAT TREATMENT MODEL

In the previous sections, the LCBOP potential was used to study zero kelvin energy minimizations of 100 atom “liquid-like” carbon sets. The energy minimizations allowed us to study n-member loop formations and preferred structures for infinite crystal setting tiled-cubes and containerless setting isolated clusters. The next step is to study physical properties of the “liquid-like” carbon at temperature ranges proposed for supercooling of the carbon melt. To do this study, molecular dynamics techniques are used to simulate the atoms at different temperatures. The simulations at temperature require a thermostat to correctly simulate the temperature of the system and for some of the cases a barostat to keep the system at a preferred pressure.

4.1.1. Molecular Dynamics Thermostats. In molecular dynamics simulations, thermostats are used to add and remove energy from the boundaries of the simulation. There are a variety of algorithms which try to simulate the adding and removing of energy in a realistic way. Popular methods for controlling the temperature rescale the atom velocities. As mentioned in Section 1, such methods include the Nose-Hoover thermostat, the Berendsen thermostat, and Langevin dynamics. Obtaining a canonical ensemble using these algorithms is not trivial as it depends on the specific system being studied. This makes it important to understand the different thermostats to know which will be useful for studies of the supercooled carbon melt.

For the Berendsen thermostat, the system is weakly coupled to the heat bath. This thermostat suppresses fluctuations of the kinetic energy and corrects the temperature of the system in the following way,

$$\frac{dT}{dt} = \frac{T_0 - T}{\tau}. \quad (4.1)$$

Here the term τ is an exponential decay time constant of the deviation of the temperature. Due to the suppression of fluctuations, the Berendsen thermostat cannot produce trajectories consistent with the canonical ensemble for small systems. When used on systems with hundreds or thousands of molecules, the approximation does generate roughly correct estimates for most calculated properties [114]. The thermostat is used mainly due to its efficiency to get the bath to a desired temperature which makes it a good candidate for initial equilibration. The Berendsen thermostat can result in the flying ice cube effect which is an artifact where the energy of high-frequency fundamental modes drains into low-frequency modes, particularly into zero-frequency motions such as overall translation and rotation of the system. This artifact is entirely consequence of the thermostat algorithm and is highly unphysical making the Berendsen thermostat only useful for efficient equilibration of the systems heat bath.

Langevin dynamics approaches the modeling of the molecular dynamics by accounting for omitted degrees of freedom using stochastic differential equations. These differential equations will consist of one or more terms being a stochastic (random) process. This will ultimately result in a solution which is also a stochastic process. Stochastic processes can model different types of phenomena. For Langevin dynamics the phenomena are thermal fluctuations. Molecular systems in the real world are unlikely to be present in a vacuum. Langevin dynamics attempts to extend molecular dynamics to

allow for effects that perturb the system such as high velocity collisions of particles and jostling of solvent. Langevin dynamics mimics the viscous aspect for a solvent but does not fully model an implicit solvent as it does not account for electrostatic screening or the hydrophobic effect which are prominent in denser solvents. We can describe Langevin dynamics by considering N particles with mass M whose coordinates $X = X(t)$ that constitute a time-dependent random variable. This will result in the Langevin equation [115],

$$M\ddot{X} = -\nabla U(X) - \gamma M\dot{X} + \sqrt{2M\gamma k_B T}R(t). \quad (4.2)$$

Here $U(X)$ is the interatomic potential, \dot{X} is the velocity, \ddot{X} is the acceleration, γ is the dampening parameter, T is the temperature, and k_B is the Boltzmann constant. $R(t)$ is a delta-correlated stationary Gaussian process which can be described by,

$$\langle R(t) \rangle = 0, \quad (4.3)$$

$$\langle R(t)R(t') \rangle = \delta(t - t'), \quad (4.4)$$

where δ is the Dirac delta function. The dampening constant should be kept small to control the temperature, but over dampening will switch to the Brownian regime where no average acceleration is estimated.

The Nosé-Hoover thermostat is a deterministic molecular dynamics algorithm for constant temperature. The heat bath only consists of one imaginary particle, but simulation systems do achieve realistic constant temperature conditions. To understand the Nosé-Hoover thermostat, we begin by considering the velocity Verlet algorithm which allows us to integrate Newton's equations of motion,

$$m_i \frac{d^2 \mathbf{r}_i}{dt^2} = - \sum_{j \neq i} \nabla_i U(|\mathbf{r}_i - \mathbf{r}_j|). \quad (4.5)$$

Here m_i is the mass of particle I , the position of the particle in three-dimensional space is $\mathbf{r}_i = (x_i, y_i, z_i)$, and similar to the other algorithms $\nabla_i U(|\mathbf{r}_i - \mathbf{r}_j|)$ is the gradient of the interatomic potential between atoms I and j . The velocity Verlet algorithm then is implemented as follows:

$$\mathbf{r}_i(t + \delta t) = \mathbf{r}_i(t) + \mathbf{v}_i(t)\delta t + \frac{\mathbf{F}_i(t)}{2m_i}\delta t^2, \quad (4.6a)$$

$$\mathbf{v}_i\left(t + \frac{\delta t}{2}\right) = \mathbf{v}_i(t) + \frac{\delta t}{2} \frac{\mathbf{F}_i(t)}{m_i}, \quad (4.6b)$$

$$\mathbf{F}_i(t) = \mathbf{F}_i(\mathbf{r}_i(t + \delta t)), \quad (4.6c)$$

$$\mathbf{v}_i(t + \delta t) = \mathbf{v}_i\left(t + \frac{\delta t}{2}\right) + \frac{\delta t}{2} \frac{\mathbf{F}_i(t + \delta t)}{m_i}. \quad (4.6d)$$

Here \mathbf{r}_i , \mathbf{v}_i , and \mathbf{F}_i are the position, velocity, and the force subjected to the i^{th} atom. No forces are dissipative, so the overall energy is conserved in this algorithm. This algorithm used within the Nosé-Hoover thermostat provides a way to simulate within the canonical ensemble.

How this is done is by introducing a fictitious dynamical variable whose physical meaning is that of a friction, ζ , which slows down or accelerates particles until the temperature reaches the desired value. The equations of motion in 3D will then change to be,

$$m_i \frac{d^2 \mathbf{r}_i}{dt^2} = \mathbf{F}_i - \zeta m_i \mathbf{v}_i, \quad (4.7a)$$

$$\frac{d\zeta}{dt} = \frac{1}{Q} \left[\sum_{i=1}^N m_i \frac{\mathbf{v}_i^2}{2} - \frac{3N+1}{2} k_B T \right]. \quad (4.7b)$$

Q in this formulation determines the relaxation of the dynamics of the friction $\zeta(t)$ and T is the target temperature. One can see that if $\frac{d\zeta}{dt} = 0$, the kinetic energy will simplify down to what is required by equipartition, $\frac{3}{2}(N + 1)k_B T$. The $3N + 1$ instead of $3N$ comes from the extra factor ζ . It is important to note that the temperature is not fixed but tends towards a target temperature. Now using the velocity-Verlet algorithm from before we can implement the Nosé-Hoover thermostat via a small modification. Our algorithm will change to,

$$\mathbf{r}_i(t + \delta t) = \mathbf{r}_i(t) + \mathbf{v}_i(t)\delta t + \left(\frac{\mathbf{F}_i(t)}{m_i} - \zeta(t)\mathbf{v}_i(t) \right) \frac{\delta t^2}{2}, \quad (4.8a)$$

$$\mathbf{v}_i(t + \delta t/2) = \mathbf{v}_i(t) + \frac{\delta t}{2} \left(\frac{\mathbf{F}_i(t)}{m_i} - \zeta(t)\mathbf{v}_i(t) \right), \quad (4.8b)$$

$$\mathbf{F}_i(t + \delta t) = \mathbf{F}_i(\mathbf{r}_i(t + \delta t)), \quad (4.8c)$$

$$\zeta\left(t + \frac{\delta t}{2}\right) = \zeta(t) + \frac{\delta t}{2Q} \left[\sum_{i=1}^N m_i \frac{\mathbf{v}_i(t)^2}{2} - \frac{3N + 1}{2} k_B T \right]. \quad (4.8d)$$

The two-step character of the velocity-Verlet algorithm must be matched so $\zeta(t)$ is first updated at time $t + \delta t/2$. One final step is needed to fully implement the thermostat into the algorithm,

$$\zeta(t + \delta t) = \zeta(t + \delta t/2) + \frac{\delta t}{2Q} \left[\sum_{i=1}^N m_i \frac{\mathbf{v}_i(t + \delta t/2)^2}{2} - \frac{3N + 1}{2} k_B T \right], \quad (4.9a)$$

$$\mathbf{v}_i(t + \delta t) = \frac{\left[\mathbf{v}_i(t + \delta t/2) + \frac{\delta t}{2} \frac{\mathbf{F}_i(t + \delta t)}{m_i} \right]}{1 + \frac{\delta t}{2} \zeta(t + \delta t)}. \quad (4.9b)$$

The last equation is slightly more complicated than the counterpart due to the dissipative force term is computed at time $t + \delta t$. The Nosé-Hoover thermostat is the most commonly used thermostat due to its accuracy and efficient methods to give constant temperatures, which is the reasoning for its use in this work over the other two thermostats discussed.

4.1.2. Molecular Dynamics Barostat. In molecular dynamics there are a range of barostat that can be used to control pressure for a simulation. Similar to the thermostat, the correct barostat to use will depend on the system being studied. For the work done here, the Berendsen barostat was chosen for its efficiency to equilibrate the pressure of the system. To implement the pressure, consider that the instantaneous pressure, P , is given by [116],

$$P = \rho T + \frac{1}{3} \frac{\sum_{i>j} \mathbf{F}(r_{ij}) \cdot \mathbf{r}_{ij}}{V}. \quad (4.10)$$

Here ρ is the density, T is the temperature, $\mathbf{F}(r_{ij})$ is the force exerted on particle i by j , and V is the system's volume. The Berendsen barostat uses a scale factor to scale the length of the box sides of the simulation to control the external pressure. The scale factor, μ , will be a function of the pressure and is given by,

$$\mu = \left[1 + \frac{\delta t}{\tau_p} (P - P_0) \right]^{1/3}. \quad (4.11)$$

τ_p is the “rise time” of the barostat which controls how the pressure will tend to the target P_0 . The Berendsen barostat can lead to violent oscillations in highly ordered systems, but with the liquid-like carbon systems studied here being a mix of amorphous and graphene-like carbon, those oscillations are negligible.

4.1.3. LAMMPS Heat Treatment Setup. The heat treatment simulations were comprised of different liquid carbon tiled cube infinite crystal systems. To study the growth, a 42-atom graphene sheet was placed inside a box with the remaining 58 atoms being randomly placed in the liquid using the Van der Waals radii distance constraint. The box size was set to give a density of 1.8 g/cm^3 . This was done for both a 3-dimensional (3D) and 2-dimensional (2D) case. To simulate in 2D, the interactions between the atoms and velocities along the z-axis were forced to zero. The LCBOP and EDIP potentials were employed for both the 3D and 2D heat treatments. The Nosé-Hoover thermostat was implemented to hold the simulation at a desired temperature. The initial atom sets for both the 3-dimensional and 2-dimensional case can be seen in Figure 4.1.

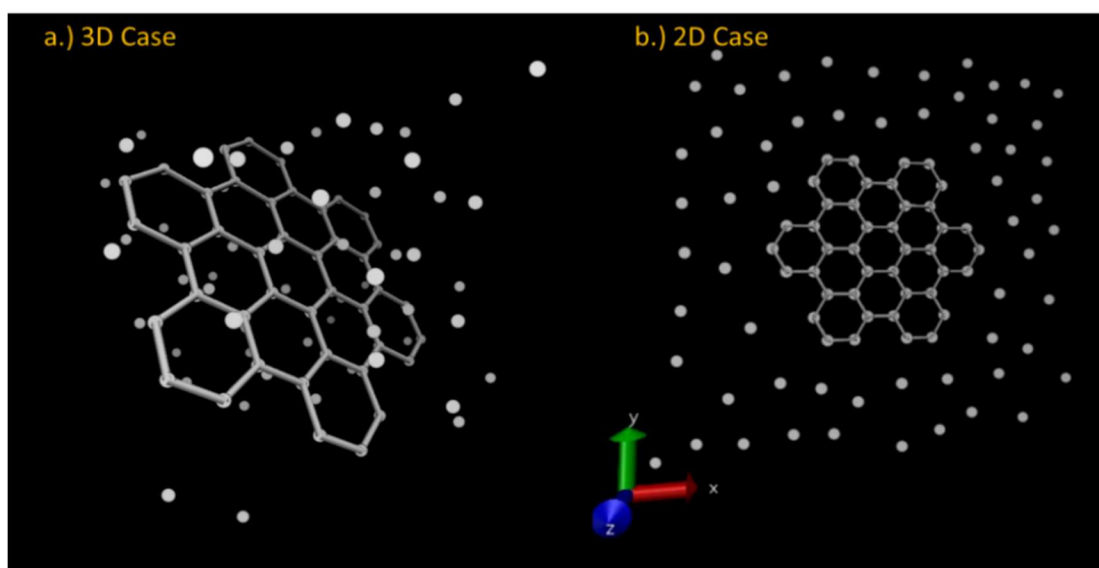


Figure 4.1. 3D and 2D 100 Atom Liquid with 42-Atom Graphene Sheet Embedded. The remaining 52 atoms were randomly placed with a nearest neighbor distance constraint of the carbon Van der Waals radii of 1.7 \AA .

After studying the growth of the system, temperature anneals were done on a 100-atom tiled-cube system that was pre-relaxed via the zero-kelvin energy minimizations done before. For a few of the simulations, a Berendsen barostat was used to hold the pressure in the range expected for the atmosphere of AGB stars. From the temperature anneals, the energy of the atoms was taken over time to study structural and physical properties of the liquid carbon. Such properties were the correlation between the coordination and different energy states and the latent heat of fusion. Lab observations of the latent heat of fusion and the bulk modulus have been evasive for some time due to the difficulties of producing stable liquid carbon in the lab. The atomistic studies here give some insight on what these values might be.

4.2. RESULTS AND DISCUSSION

The simulation time step for the heat treatments of the 100-atom liquid with the 42-atom graphene sheet embedded was 0.02 picoseconds (2 femtoseconds) and done for 1 million iterations. This gives a total simulation time of heat treatment anneals of 20 nanoseconds. To study the growth of the system, the final atoms in the sheet were calculated by using the loop counting code used for the zero-kelvin tiled-cube energy minimizations. To double check the loops were added to the initial sheet, a trajectory file was created for the simulation to be used in the Virtual Molecular Dynamics (VMD) software from the Nation Institute of Health and the department of biophysics at the University of Illinois at Urbana-Champaign [117]. When looking at the growth in 3D, Figure 4.2 shows no noticeable growth after heat treatment at 2800 K for the LCBOP case though atoms do seem to be nucleating above and below the sheet. For EDIP case obvious

dissipation of the graphene sheet can be seen. This is a common trend for all temperatures in the range of 2400-3800 K anneals studied. Considering the lab-observed growth times of tenths-of-milliseconds, the fact that no growth is being seen in the 3D case during the 20 ns heat treatment can be expected.

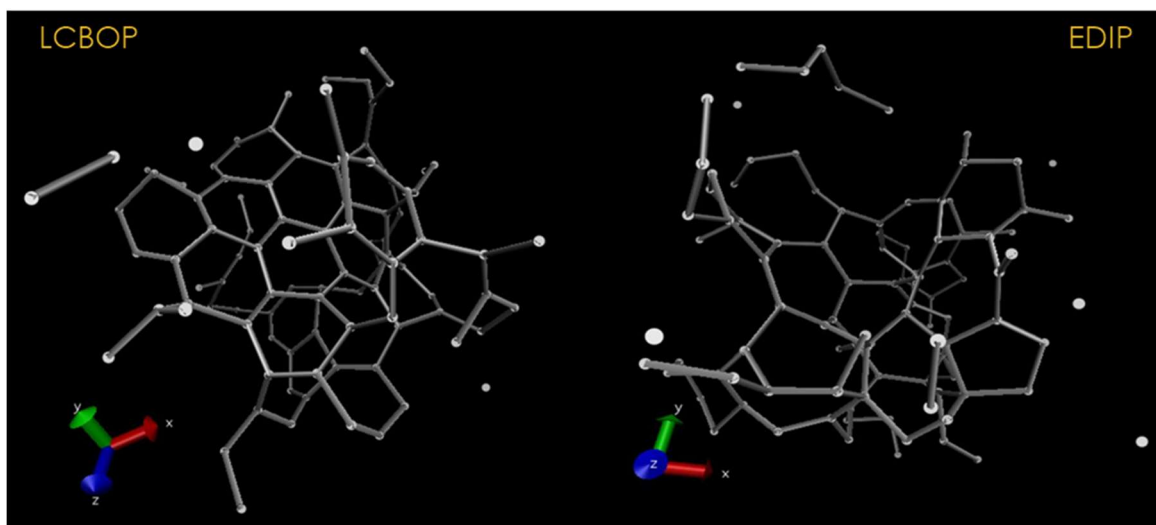


Figure 4.2. VMD of 3D Final Positions after 20 ns Heat Treatment at 2800 K. Nucleation above and below the sheet can be seen in the LCBOP case where dissipation of the sheet can be seen in the EDIP case.

Moving to 2D, we see a different outcome for our growth studies for the two potentials. Figure 4.3 shows the final positions after heat treatment at 3800 K for both the LCBOP and EDIP cases. The graphene sheet is seeing noticeable growth for both cases as the atoms appear to be solidifying into a singular graphene sheet. Both the LCBOP and EDIP cases show pentagonal loop formation, but the EDIP shows these loops form near the center of the sheet. Lab observations show that a central pentagon will have the hexagonal sheets form at an angle and not flat. As the simulations were 2D and forced z-directionality to zero, this type of growth does not seem physical. LCBOP's pentagons

form mainly on the edge of sheets and due to higher degrees of freedom are likely metastable or formed due to the “pentagon first” mechanism at a Y-junction. The atom addition as a function of temperature in Paper I shows a trend of increased growth with increased temperature. The growth of the 70-80 atoms over 20 ns in simulation compared to the tenths-of-milliseconds growth of 60 atom sheets from observational data points towards scaling relationships for growth between the 2D liquid and higher dimension liquid.

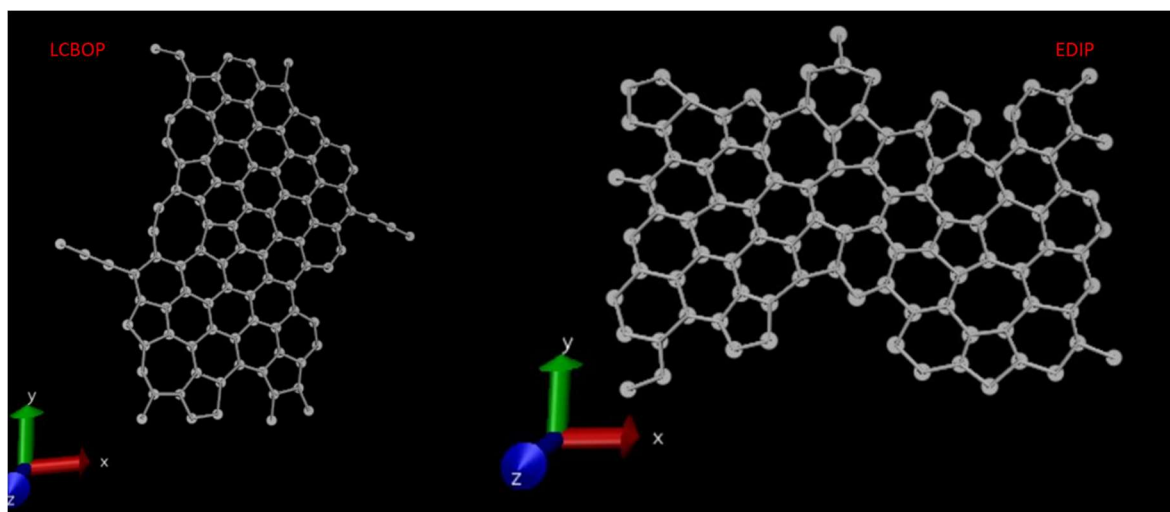


Figure 4.3. VMD of 2D Final Positions after 20 ns Heat Treatment at 3800 K. Growth and solidification can be seen for both cases, but the pentagonal center loops should not be flat making them non-physical or metastable.

Studying growth is a good way to look at the structure of a system using MD simulations. Apart from that, the study of physical properties of a material can be done. To study physical properties of the supercooled liquid carbon, a 100-atom liquid previously equilibrated via zero-kelvin energy minimization was heat treated in a box such that the density would be 1.8 g/cm^3 . From the heat treatment, the atom positions and energy values

of each atom were taken throughout the time integration of the simulation. Having the energy values at each time interval allowed us to graph the energy of each atom at any given point in time and see how the atom energies changed over the simulation. This is displayed in Figure 4.4.

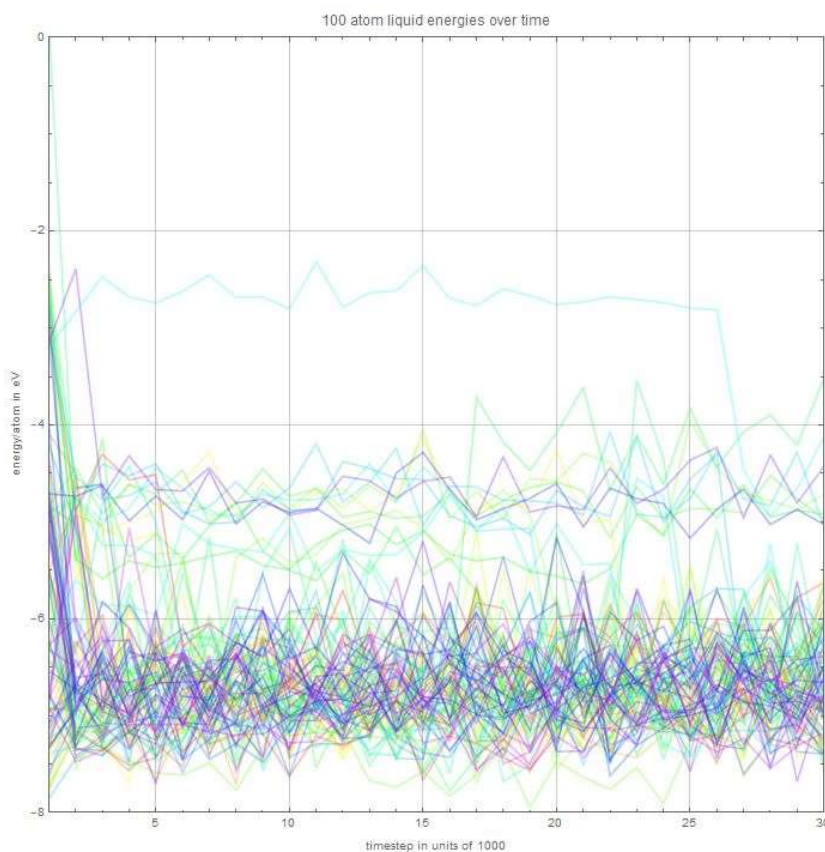


Figure 4.4. 2500 K Heat Treatment Energy vs. Time. Pre-relaxed, via energy minimization, 100-atom carbon liquid at 1.8 g/cm^3 .

The first thermodynamic property studied from the energy versus time data was the latent heat of fusion, ΔH_f . This was done both with and without the Berendsen barostat to determine any pressure dependence. To determine ΔH_f , the difference between the binding

energy within graphene, ~ 7.4 eV, and the average energy of atoms that had binding energies smaller than graphene binding. For the simulations without the Berendsen barostat the average ΔH_f value came to be 1.015 ± 0.078 eV/atom. When holding the pressure at $\sim 10^{-3}$ bars, the average value comes out slightly higher at 1.178 ± 0.053 eV/atom.

Flash heating studies [118] of carbon and high pressure melting of graphite [119] determined ΔH_f values of 1.04 to 1.14 ± 0.12 eV/atom and an average of 1.08 eV/atom respectively. These experimentally determined values fall in the range and uncertainties of values determined from these simulations when looking at both high-pressure and low-pressure systems. DFT studies into the melting of graphite have also considered values for ΔH_f .

One reported using a value of 1.20 eV/atom [120] where another determined a value of 1.05 eV/atom [121] which both fall in the high and low ends of the determined range for the latent heat. Figure 4.5 shows ΔH_f as a function of temperature for both cases. The value stays relatively constant and both high and low-pressure cases fall relatively close within the error bars of one another. Figure 4.5 shows an insensitivity to the pressure and temperature for the latent heat of fusion value.

Looking back at Figure 4.4, the presence of possible distinct energy bands can be seen. Having the energy of each atom at the different time intervals, it is possible to look at how the energy of a single atom changes and to see if the energy band is in fact a phenomenon going on during the simulation. Figure 4.6 looks at one atom within the simulation and the distinct energy bands the atom fluctuates within can be seen. Since the energy bands are a phenomenon within the graph, these energy bands should have some sort of correlation to the structure of the system.

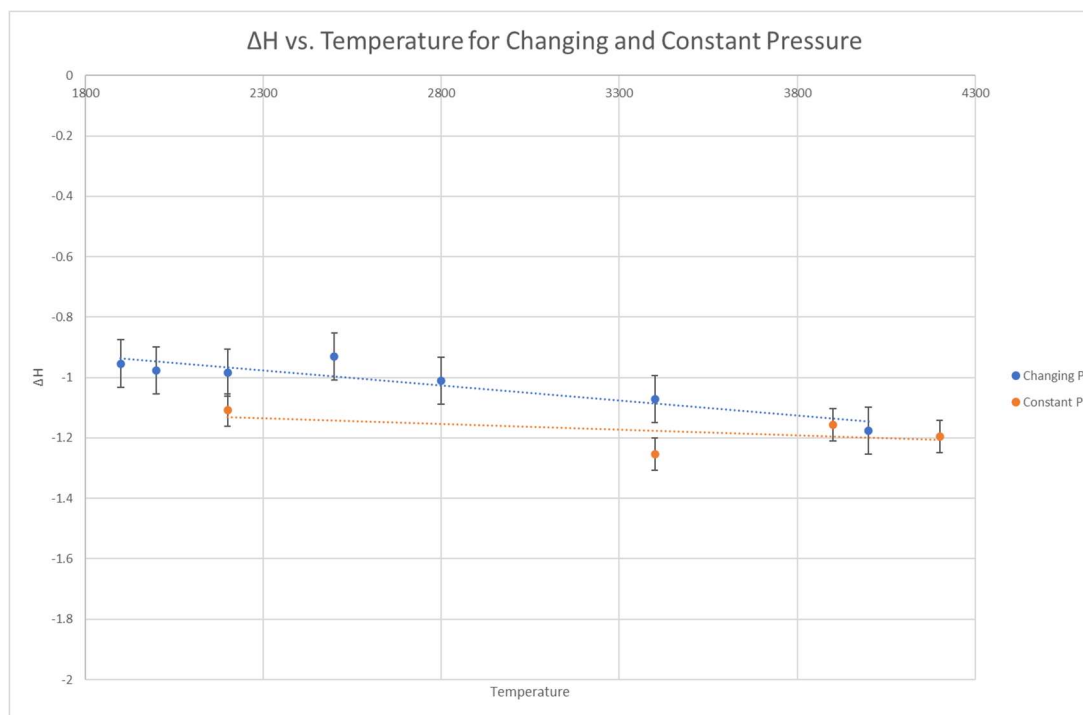


Figure 4.5. Latent Heat of Fusion vs. Temperature for Different Pressure Cases. Liquid carbon when simulation allows external pressures to change (blue line high-pressure case) and being held constant using Berendsen barostat (orange line low-pressure case).

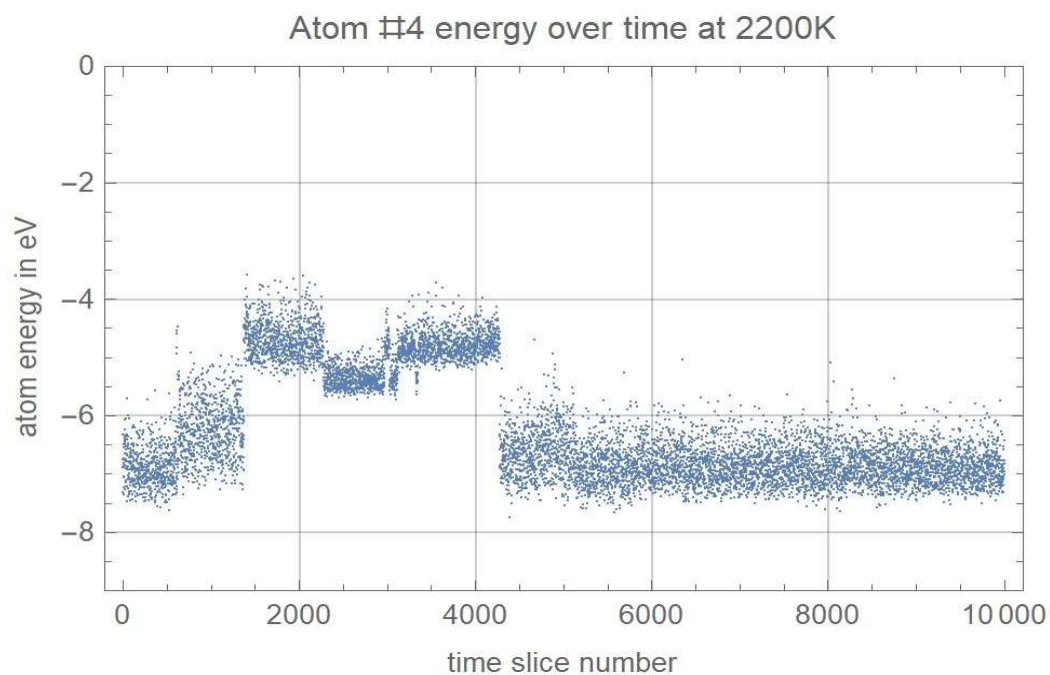


Figure 4.6. A Carbon Atom Through Time. The binding energy of a single atom in a 2200 K heat treatment of a 100-atom carbon liquid at 1.8 g/cm^3 density.

The atom positions of each atom were also taken at the different time intervals of the simulation. From the atom positions, the coordination of each atom can be determined. With the binding energy of each atom and the coordination of each atom, the relation between a carbons binding energy and coordination can be determined. In Table 4.1, the coordination statistics for different heat treatments both with and without the Berendsen barostat was generated. Similar to the zero-kelvin simulations, there is a high percentage of carbyne and graphene coordination. The energy of each atom of the given coordination was taken. A range of binding energies and an average binding energy was determined for each coordination number and displayed in Table 4.1 as well. The data is showing that on average in the supercooled liquid, a coordination-1 carbon atom will have a binding energy of $3.22 \pm 0.72 \text{ eV}$, a coordination-2 carbon atom will have $6.21 \pm 0.54 \text{ eV}$, and coordination-3 atoms have the expected 7.40 eV .

Table 4.1. Coordination Statistics and Binding Energies After Heat Treatment. 100 atom carbon liquid coordination statistics and binding energy range and averages from different temperature heat treatments.

Number of atoms with specific coordination at different temperatures			
Temp	1	2 (sp)	3 (sp²)
1900 K	4	31	65
2200 K	6	46	48
2200 K Cons P	5	45	50
2500 K	8	40	52
2800 K	9	45	46
3400 K	14	43	43
3900 K	13	40	47
3900 K (t = 400)	0	8	92
Percentage	8.43%	41.43%	50.14%
Range of Binding Energy	2.31-4.15 eV	5.30-7.12 eV	7.21-7.52 eV
Average Binding Energy	$3.22 \pm 0.72 \text{ eV}$	$6.21 \pm 0.54 \text{ eV}$	$7.39 \pm 0.12 \text{ eV}$

4.3. CONCLUSION

In this section, the LCBOP and EDIP semi-empirical potentials for carbon were used with the Nosé-Hoover thermostat and occasionally also with the Berendsen barostat to do a molecular dynamics simulation of sets of 100 supercooled low- density and pressure carbon atoms. One atom set had a 42-atom graphene sheet embedded into the 100-atom liquid, while the other set was a pre-relaxed at 0K set of 100-atoms. Set temperature simulated anneals were done at temperatures ranging from 1900-3900K over 20 ns total simulation time integrations. The atom positions and their binding energies were taken throughout the simulation. With the atom positions, the VMD simulator was used to study the growth in both 2D and 3D. The energy values were used to determine the thermodynamic property of the latent heat of fusion and its pressure dependence. Lastly, the combination of the atom energies and their positions over time were used to determine a correlation between the binding energies and the atom coordination.

For the 3D growth case, both potentials used show negligible growth over the 20 ns simulation time. Of the two, EDIP shows more dissipation than any nucleation or growth to the embedded sheet. This trend remains for all the temperature anneals studied. When considering lab-grown cores grew at time scales of tenths-of-milliseconds compared to the 20 ns in simulation, the trend of negligible growth in the LCBOP case and dissipation in the EDIP case makes sense. Also, one can consider that the supercooling limit for liquid carbon might be more than the usual 30% for liquid metals. For the range of temperatures studied, a majority are at supercooling temperature of 45% or higher. If the onset of solidification is at supercooling of 50 or even 60%, the 5-member and 6-member loops may not be stable. The instability of 5- or 6-member loops and the time scale could be the

leading factors in why negligible growth, and even dissipation in the EDIP case, was seen for simulations in 3D.

For the 2D growth case, both potentials see noticeable growth of the graphene sheet. A trend of increased growth as the temperature increases which follows our analytical model for growth. The 20 ns to growth 70-80 atom sheets in simulation compared to 60 atoms in tenths-of-milliseconds in the lab could give insight into a scaling relationship between 2D and 3D growth. Pentagonal loop formation is prominent for both potentials, but for the EDIP case these loops form near the center of the sheet. A central pentagon will have hexagonal loops nucleate and then grow at an angle and not flat. As the simulations were 2D and forced z-directionality to zero, this type of growth may be showing some non-physical phenomena. LCBOP on the other hand had pentagons form mainly on the edge of sheets. Due to having higher degrees of freedom these pentagons are likely metastable or formed from the “pentagon first” mechanism.

The binding energies of the individual atoms after simulated annealing of a 100-atom liquid pre-relaxed via energy minimization at 0K were used to determine the latent heat of fusion, ΔH_f . To determine this thermodynamic property, the difference between the binding energy for graphene and the average binding energy of atoms smaller than that was taken. This was done for simulations which did and did not have a Berendsen barostat used. The average ΔH_f value came to be 1.015 ± 0.078 eV/atom for the high-pressure case using no barostat. For the low-pressure case holding the pressure at $\sim 10^{-3}$ bars, the average value came out slightly higher at 1.178 ± 0.053 eV/atom. Both high-pressure and low-pressure systems give values that fall within the range of uncertainty of experimental flash heating and high-pressure melting studies of carbon. DFT studies used a value of 1.20

eV/atom without external reference or given reason, and another DFT study determined a value of 1.05 eV/atom at zero-pressure for ΔH_f . The intuitive choice still falls in the high end of the determined range for the latent heat while the zero-pressure calculation falls within the low end.

Both the atom positions and binding energies were used to determine a correlation between the atom coordination and its binding energy as distinct energy bands can be seen when looking at the energy of each atom over the integration time. Taking the energy of each atom at a given coordination, an average energy for each coordination value can be determined. For coordination-1 atoms the average binding energy came to be 3.22 ± 0.72 eV, coordination-2 carbon atoms had an average energy of 6.21 ± 0.54 eV, and coordination-3 atoms had their averages come out to be the expected 7.40 eV. The correlation between the coordination number and the binding energy gives a specific energy state for a carbon atom based on the number of nearest neighbors in the environment. The data also showed once again for the supercooled low-density liquid carbon a high percentage of sp and sp² coordination which corresponds to a mixture of carbyne and graphite structuring as seen in previous DFT studies. This helps support that the low-density carbon melt will have either stable or metastable carbyne chains which could produce pentagon nucleation seeds from the Y-junction “pentagon first” mechanism.

5. ANALYTICAL MODELING OF LIQUID CARBON 2D NUCLEATION AND SOLIDIFICATION

5.1. NUCLEATION MODEL

The analytical model to study the low-pressure liquid carbon starts from classical nucleation theory which describes a first-order phase transition which describes the rate of formation of nucleating clusters from a nonequilibrium state. The pioneering works of Becker and Döring [122], Zeldovich [123], and Turnbull and Fischer [58] laid the groundwork for future nucleation theories. The Becker-Döring- Zeldovich (BDZ) theory states that the rate of nucleation in condensed systems such as solid-solid transformations or liquid-solid transformations can be written as follows,

$$r^* = K \exp \left[-\frac{(\Delta F_i^* + q)}{k_B T} \right]. \quad (5.1)$$

Here, ΔF_i^* is the maximum free energy for nucleus formation, q is the activation energy for diffusion across the phase boundary, k_B is the Boltzmann constant, T is the temperature, and K is an unknown constant. Turnbull and Fischer went on to extend BDZ theory to derive an exact expression for r^* based on the theory of absolute reaction rates to determine the unknown constant K .

To do so, a metastable state can typically be assumed to be a mixture of clusters containing n molecules and molecules in the nonequilibrium state. In BDZ theory, direct interactions between the clusters are neglected meaning the clusters will only change their size due to an evaporation-condensation mechanism. Mainly, a cluster of n molecules will only grow or shrink by the condensation or loss of a single molecule. The derivation of Turnbull and Fischer gives a rate of nucleation to be eqn. (1.2),

$$r^* \cong \left(N \frac{k_B T}{h} \right) \exp \left[- \frac{(\Delta f^* + \Delta F^*)}{k_B T} \right]. \quad (5.2)$$

Earlier in this dissertation, N is described as the number density of nuclei per unit volume and h is Planck's constant. Another way of describing this pre-exponential factor is that $N = N_n(t)$ which is the average number of clusters of size n at time t within the volume.

The nucleation rates of BDZ and Turnbull and Fischer have been good approximations, but recent understanding from studies of liquid metals give a more accurate representation of nucleation. These models so far have looked at a specific thermodynamic variable called the free energy. This energy is in fact the Gibbs free energy which is a function of other thermodynamic parameters. The theory of thermodynamics tells us that a phase transformation will only take place when the change in the Gibbs free energy, ΔG , has a negative value. The interest of the work done here is on the transition to a solid within a supercooled liquid.

For this, the total Gibbs free energy of a system, assuming the nucleus will be spherical in geometry, will have two contributions. The first will be the contribution from the energy difference between the solid and liquid phases, the volume Gibbs free energy ΔG_v . The value of ΔG_v will be negative if the systems temperature is below the equilibrium solidification temperature. The magnitude of this contribution will be product of this difference and the volume of the spherical critical nucleus. The second contribution will come from the solid-liquid phase boundary during the transformation. A positive surface free energy, σ , with its magnitude being a product with the surface area of the nucleus will constitute this phase boundary contribution. From this we can describe the Gibbs free energy as follows [124],

$$\Delta G = \frac{4}{3}\pi r^3 \Delta G_v + 4\pi r^2 \sigma. \quad (5.3)$$

Plotting the energy change as a function of radius, the energy change will give an initial increase until it passes through a maximum. After passing through this maximum, the energy change will start to decrease as show in Figure 5.1. Physically what this means is as liquid atoms start to form solid clusters the free energy will increase in the system. Growth will continue in the system with a decrease in energy as long as the cluster reaches a certain critical radius r^* . If the cluster does not reach the critical radius for growth, the cluster will begin to shrink and eventually dissolve.

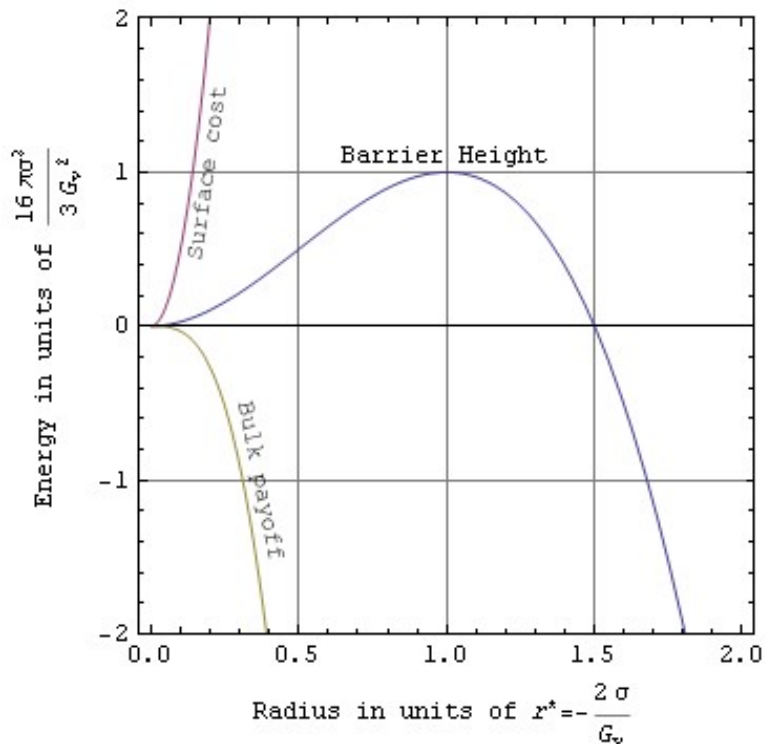


Figure 5.1. 3D Cluster Free Energy vs. Cluster Radius.
Classical cluster energy as a function of cluster radius.

From Figure 5.1 we can see that at the maximum of the energy curve there is a critical free energy, which will be denoted as ΔG^* , which occurs at the critical radius. This critical energy is the free energy required to form a stable nucleus. In other words, the critical energy is the activation free energy barrier for nucleation. As there is a maximum point on the free energy curve which occurs at r^* and ΔG^* , these two parameters can be derived by differentiating eqn. (5.3) with respect to the radius. Setting the differentiation to zero, we can solve for r^* . This gives,

$$\frac{d(\Delta G)}{dr} = 4\pi\Delta G_v r^2 + 8\pi\sigma r = 0, \quad (5.4a)$$

$$4\pi\Delta G_v r^2 = -8\pi\sigma r, \quad (5.4b)$$

$$r^* = -\frac{2\sigma}{\Delta G_v}. \quad (5.4c)$$

Now r^* can be substituted back into eqn. (5.3) to yield an expression for ΔG^* ,

$$\Delta G^* = \frac{4}{3}\pi \left(-\frac{2\sigma}{\Delta G_v}\right)^3 \Delta G_v + 4\pi \left(-\frac{2\sigma}{\Delta G_v}\right)^2 \sigma, \quad (5.5a)$$

$$\Delta G^* = -\frac{4}{3}\pi \frac{8\sigma^3}{\Delta G_v^2} + 4\pi \frac{4\sigma^3}{\Delta G_v^2}, \quad (5.5b)$$

$$\Delta G^* = \frac{16\pi\sigma^3}{3\Delta G_v^2}. \quad (5.5c)$$

ΔG_v is a temperature dependent driving force for solidification. ΔG_v is zero at the equilibrium melting temperature, T_m , and as the temperature decreases the volume free energy will be increasingly negative. The temperature dependence of ΔG_v can be derived from the general equation for the Gibbs free energy, which is given by,

$$G = H - TS. \quad (5.6)$$

Here H is the enthalpy, S is the entropy, and T is the temperature. The H term is weakly dependent on temperature, but the term TS is strongly dependent on temperature. To get the temperature dependence for G the first step is to take the partial derivative with respect to T . This gives,

$$\frac{\partial(G)}{\partial T} = \left(\frac{\partial G_{Final}}{\partial T} \right) - \left(\frac{\partial G_{Initial}}{\partial T} \right) = -\Delta S. \quad (5.7)$$

The final and initial free energies can be thought of in different ways in the partial derivative. For example, in a usual chemical reaction the final phase is the products, and the initial phase is the reactants. Here the initial phase would be the liquid carbon atoms, and the final phase would be the solid cluster nucleus.

From eqn. (5.7) the temperature dependence can be derived by considering the two different phases of the reaction. The value of ΔG_v is the difference between the liquid and solid Gibbs free energies, eqn. (5.6) as follows,

$$\Delta G_v = G_S - G_L = \Delta H_f - T\Delta S, \quad (5.8)$$

Here $G_{S,L}$ are the Gibbs free energies of the stable solid and metastable liquid phases and ΔH_f is the enthalpy (latent heat) of fusion. The term, ΔH_f , is the amount of heat given up during transformation from liquid to solid. The point at which the Gibbs free energy for both the liquid and solid will happen at a specific critical equilibrium melting temperature, T_m . Solving for this temperature we get,

$$T_m = \frac{\Delta H_f}{\Delta S}. \quad (5.9)$$

Solving for the entropy, and plugging back into eqn. (5.8) the following equation can be gained,

$$\Delta G_v = \Delta H_f - T \frac{\Delta H_f}{T_m}, \quad (5.10a)$$

$$\Delta G_v = \Delta H_f \left(1 - \frac{T}{T_m}\right), \quad (5.10b)$$

$$\Delta G_v = \frac{\Delta H_f \Delta T}{T_m}. \quad (5.10c)$$

Here $\Delta T = T_m - T$ which is known as the supercooling limit. This limit of the supercooling gives a barrier to nucleation from the undercooling of the metastable liquid [125].

Using the temperature dependent expression for ΔG_v , the expressions for the critical radius and free energy can be updated to the following,

$$r^* = -\frac{2\sigma T_m}{\Delta H_f (T_m - T)}, \quad (5.11a)$$

$$\Delta G^* = \frac{16\pi\sigma^3 T_m^2}{3\Delta H_f^2 (T_m - T)^2}. \quad (5.11b)$$

What these expressions say is that as temperature decreases, both the critical radius and free energy will increase. Physically, this tells us that as the temperature lowers further below the equilibrium melting temperature nucleation of solid clusters will happen more readily. These expressions are for the 3D case, but when considering a low-pressure system for a supercooled carbon melt nucleation will be graphene sheets. This will result in 2D nucleation, and the Gibbs free energy contribution will be given by the following,

$$\Delta G = \pi r^2 \Delta G_A + 2\pi r \lambda. \quad (5.12)$$

Before the Gibbs free energy had a volume contribution, ΔG_v , here the energy is the product between the energy difference and the area of critical nucleus. The analogue for the interfacial surface free energy, σ , will be the edge free energy denoted by λ which will be

multiplied by the perimeter of the nucleus. Plotting the energy as a function of the radius, a critical energy and radius can be seen in Figure 5.2.

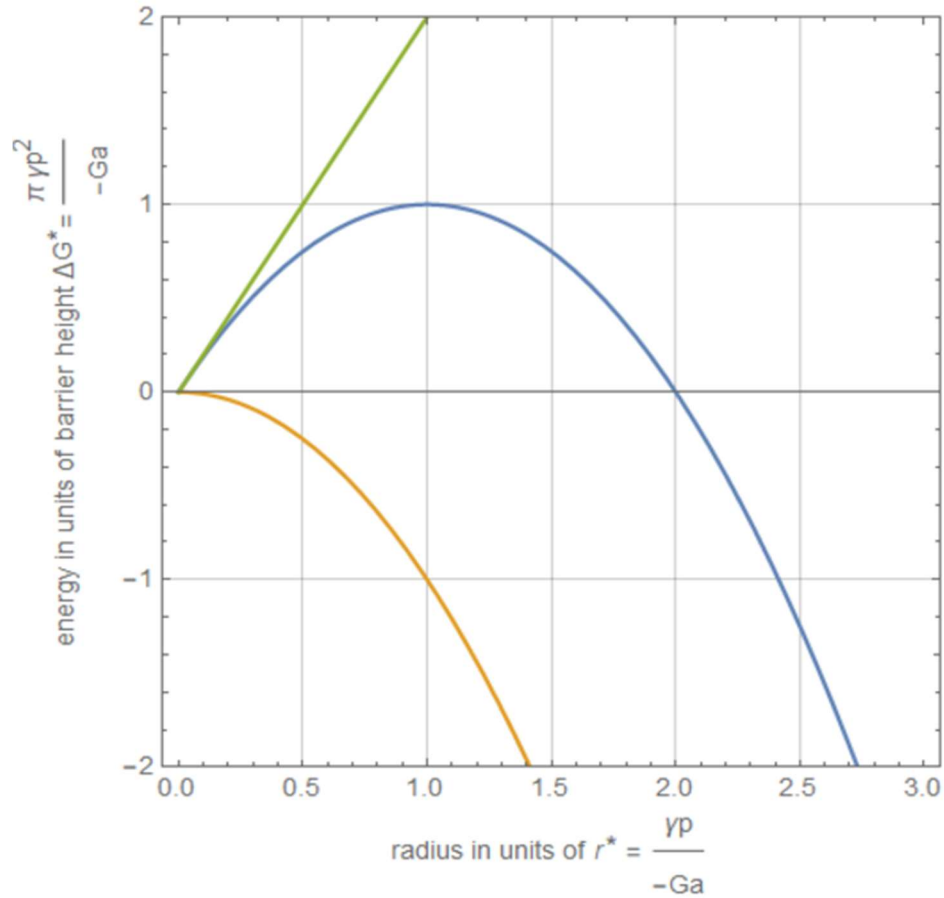


Figure 5.2. 2D Cluster Free Energy vs. Cluster Radius. Energy change (green), radius (orange) and critical radius plots for nucleation and growth of 2D sheets from a liquid matrix.

Similar to the 3D case, expressions for the critical radius and Gibbs free energy can be derived for 2D. To start, the derivation of eqn. (5.12) will be taken with respect to the radius and set equal to zero giving the following,

$$\frac{d(\Delta G)}{dr} = 2\pi r \Delta G_A + 2\pi \lambda = 0. \quad (5.13)$$

Some trivial algebra will show give an expression for the critical radius and plugging that back into equation (5.12) will give the critical Gibbs free energy in 2D to be as follows,

$$r^* = -\frac{\lambda}{\Delta G_A}, \quad (5.14a)$$

$$\Delta G^* = \frac{2\lambda^2}{\Delta G_A}. \quad (5.14b)$$

The temperature dependence for the critical radius and Gibbs free energy can be determined using the fact that the Gibbs free energy temperature dependence expression comes from the Gibbs equation which is a general thermodynamic property. Using $\Delta G_A = \Delta H_f \Delta T / T_m$ and the supercooling limit, $\Delta T = T_m - T$, the temperature dependence can be written as,

$$r^* = -\frac{\lambda T_m}{\Delta H_f (T_m - T)}, \quad (5.15a)$$

$$\Delta G^* = \frac{2\lambda^2 T_m}{\Delta H_f (T_m - T)}, \quad (5.15b)$$

Considering the theory of thermodynamic fluctuation dictated by the second law of thermodynamics [123], the distribution of solid clusters will obey a Gaussian distribution,

$$\eta = A e^{-\frac{\Delta G^*}{k_B T}}. \quad (5.16)$$

The pre-exponential constant A here will be related to the number of nuclei of the solid phase and give us the correct units for a time rate at which the stable number of nuclei increases. Following once again the classic work of Turnbull and Fischer, the time rate of increasing stable nuclei can be expressed as,

$$\frac{\delta \eta}{\delta t} \cong \left(\frac{k_B T}{h} \right) e^{-\frac{\Delta G^*}{k_B T}} \eta_0 t. \quad (5.17)$$

Here $\eta_0 t$ is the expression for $N = N_n(t)$ from equation (5.2). Considering again the 2D nature of the graphene sheet nucleation of the low-pressure supercooled carbon liquid, we can express this nucleation rate in terms of different parameters by substituting in equation (5.15b),

$$\frac{\delta\eta}{\delta t} \cong \left(\frac{k_B T}{h}\right) \exp\left[-\frac{2\lambda^2 T_m}{\Delta H_f (T_m - T)} \left(\frac{1}{k_B T}\right)\right] \eta_0 t. \quad (5.18)$$

The contribution from the clustering of atoms by short range diffusion is usually the next piece to consider, but observational data has given insights that the nucleation of the low-pressure supercooled carbon melt will be reaction limited so no diffusion effects are being considered at this time. From equation (5.18) three major parameters are required for understanding the nucleation, the interfacial edge energy λ , the latent heat of fusion ΔH_f , and the temperature T . As the expression is written now, the nucleation predicted will be for a set temperature equilibrium system.

In the atmosphere of an AGB star or in a vacuum oven in the lab, the temperature of the system will not be set but evolve over time and cool. From this, the importance of the temperature will be the cooling rates and they can differ drastically. The lab grown carbon onions had cooling rates on the order of 1000K per millisecond whereas in the solar atmosphere the cooling rates are on the order of 1K per minute. These cooling rates differ by $\sim 10^7$ orders of magnitude meaning the two systems could have drastically different phenomenon occur. The cooling rates for the solar atmosphere case were determined by finding the temperature versus time for the carbon particles as they are being ejected from the solar atmosphere. This solar cooling rate can be seen in Figure 5.3.

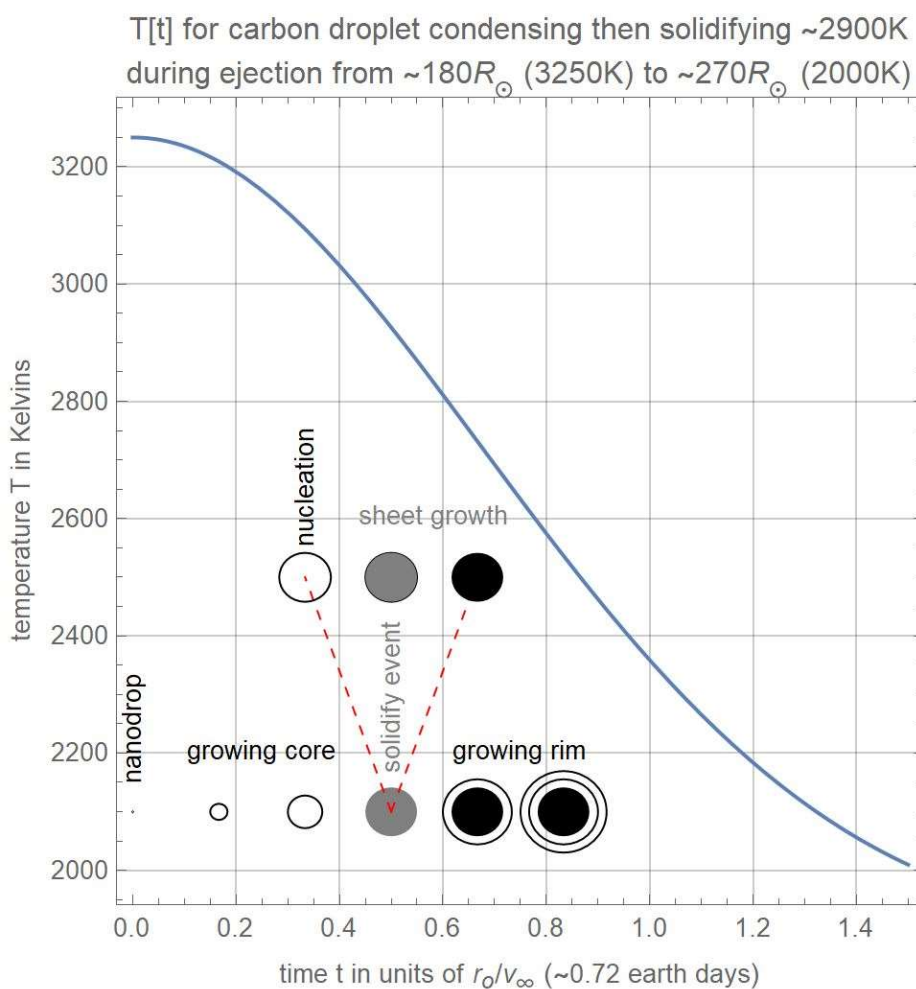


Figure 5.3. AGB Star Temperature vs. Time for a Growing Carbon Grain. Condensed (final size under 1 micron in diameter) in (or just outside) the photosphere of an AGB star, with schematics that illustrate stages in the ejection process. The cooling rate is on the order of 1.07 K/minute.

5.2. GROWTH MODEL

With the nucleation model set, the next step is to determine a model for the growth of the 2D graphene sheets. This was described in Paper I but will be restated here as well for review and expand the model. The 2D growth will be at sheet edges only. From this, one can consider starting with a circle of radius r and the number of atoms to be describes as $n \approx \sigma \pi r^2$ where σ is the number of atoms per unit area in a graphene sheet. At a given

temperature, the rate of atom addition will be proportional to the perimeter immersed in the growth liquid given by,

$$p \approx 2\pi r = 2\pi \sqrt{\frac{n}{\pi\sigma}} = 2\sqrt{\frac{\pi n}{\sigma}}. \quad (5.19)$$

The perimeter is proportional to \sqrt{n} making the differential equation which will describe the growth will take the following form,

$$\frac{\delta n(t)}{\delta t} = \left(\frac{\delta n/\delta t}{p}\right)p = a\sqrt{n(t)}, \quad (5.20a)$$

$$a = 2\sqrt{\frac{\pi}{\sigma}} \frac{\delta n}{p\delta t}. \quad (5.20b)$$

The proportionality constant, a , can be physically described as the rate of atom addition for a given temperature where the term $\frac{\delta n}{p\delta t}$ is the presumed constant rate of atom addition per unit length of perimeter.

The solution to the first order differential equation, with the initial condition that the critical starting seed will be $n(0) = b$, is quadratic in time and is given by the following form,

$$n(t) = b + a\sqrt{bt} + \left(\frac{at}{2}\right)^2. \quad (5.21)$$

Nominally, the value b will be 6 as individual carbon atoms forming a single hex loop are plausible nucleation seeds due to their tight binding energies. It can also be presumed from previous work that pentagonal loops are also plausible nucleation seeds. This value for b can also be updated to consider changing effects of edge curvature, shape changes during growth, and other processes which can affect the growth.

The next step for our growth model is to add the temperature dependence. This is done by adding an attempt rate similar to our nucleation model and a Boltzmann factor probability comprised of an Arrhenius activation energy. The attempt rate and activation energy come into the model via the atom addition rate per unit length of perimeter giving the following,

$$\left(\frac{\delta n}{p\delta t}\right) = \frac{k_B T}{h\Delta x} e^{-\frac{\varepsilon}{k_B T}}. \quad (5.22)$$

Here Δx is the separation between source regions along the perimeter and ε is the Arrhenius activation energy. The value for Δx can be determined from geometry and empirical data from lab grown specimens and *ab initio* studies allow for the value for ε can be determined as well [126]. The graph of the temperature dependence on this model can be seen in Figure 5.4.

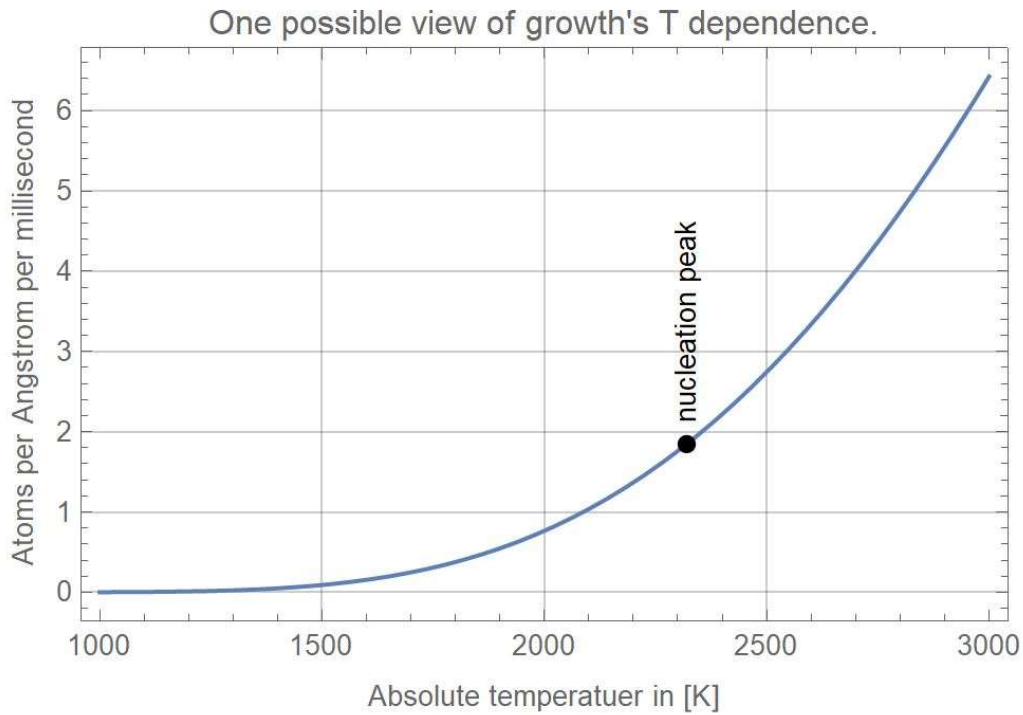


Figure 5.4. Growth Rate Temperature Dependence. The black dot represents where the nucleation peak showing that as these low temperatures, the growth rate is slow.

5.3. RESULTS AND DISCUSSION

5.3.1. Supercooling Threshold. Analysis of the solidification processes and undercooling of liquid carbon from the nucleation and growth models has led to some interesting insights. When comparing to other metallic elemental liquids whose undercooling is universally thought to be around 30% of the melting temperature [127,128], the work here instead shows undercooling on the order of 50-60% of the melting temperature for carbon. The rate of nucleation will be at its maximum at this critical temperature value which coincides with the critical radius for the nuclei allowing growth. The growth of the graphene sheets is due to the 3D liquid transitioning into a 2D solid. The work here has shown that for elemental carbon, supercooling thresholds of 50-60% below the melting temperature are reached before critical nuclei size can be achieved.

The nucleation is highly dependent on the latent heat of fusion and edge energy as they dictate the criticality for nucleation of the liquid to solid transition for carbon as seen from equations 5.15a and 5.15b. The critical temperature of nucleation will be dependent on the latent heat of fusion and the edge energy as well as the dimension of the nucleation theory which dictates the system. This can be seen by the following descriptions of the supercooling temperature for 2D and 3D,

$$T_{crit2} = T_{melt} \left(1 - \frac{\lambda}{\Delta H_f} \sqrt{\frac{\pi\sigma}{n_{crit}}} \right), \quad 5.23a$$

$$T_{crit3D} = T_{melt} \left(1 - \frac{2\gamma}{\Delta H_f} \left(\frac{4\pi\rho}{3n_{crit}} \right)^{\frac{1}{3}} \right). \quad 5.23b$$

Here σ and ρ are densities of atoms, n_{crit} is the critical number of atoms, and ΔH_f has different dimensions for the different dimensionality of the nucleation model. There is a

clear dependence for the 2D case on the ratio between the latent heat of fusion and the edge energy and an overall dependence on the critical temperature on the dimensionality of the system.

In this work we use values for these parameters estimated by the atomistic simulation temperature anneals done with LCBOP. For any model for nucleation of a carbon liquid into a solid to be able to make physical predictions, these two parameters must be specific values otherwise the onset of solidification would constantly shift. Other works have estimated values for the edge energy for the liquid-solid transition which [121], but the values presented lead to critical radii smaller than the radius of a carbon atom and critical temperature values that don't agree with predictions from observational data.

5.3.2. Solidification Rates. The solidification models also give insights into graphene sheet number density and fraction crystalline which both have been observed from lab grown and pre-solar micron sized core/rim spheres. Figure 5.5 shows the temperature dependence of the nucleation. A clear peak can be seen at 2350 K along with saturation insights based on fast or slow cooling of the carbon melt. Observations of lab grown graphene sheet number densities show much larger abundance than from pre-solar specimens.

The physical reason for this difference is due to the different cooling rates. In the stellar atmosphere of an AGB star, the carbon will sit at high temperatures for a long period of time. The nucleation rate will be extremely small, but the few nuclei that will reach critical size will grow due to the faster growth rate at high temperatures. This will have larger sheet sizes, but less total amount of sheets. For the lab grown case where cooling is rapid, the temperature will quickly move to the maximum nucleation rate. This allows

many nuclei to reach critical size and be seeds for growth. The growth rate is slower so the size of the sheets will be smaller but there will be a larger abundance of graphene sheets. This cooling rate dependence also gives insight into the saturation effects of the two different situations. The slow cooling system will require adding a saturation effect into the analysis as the fast growth rate has the system running out of atoms much faster than the fast-cooling rate system.

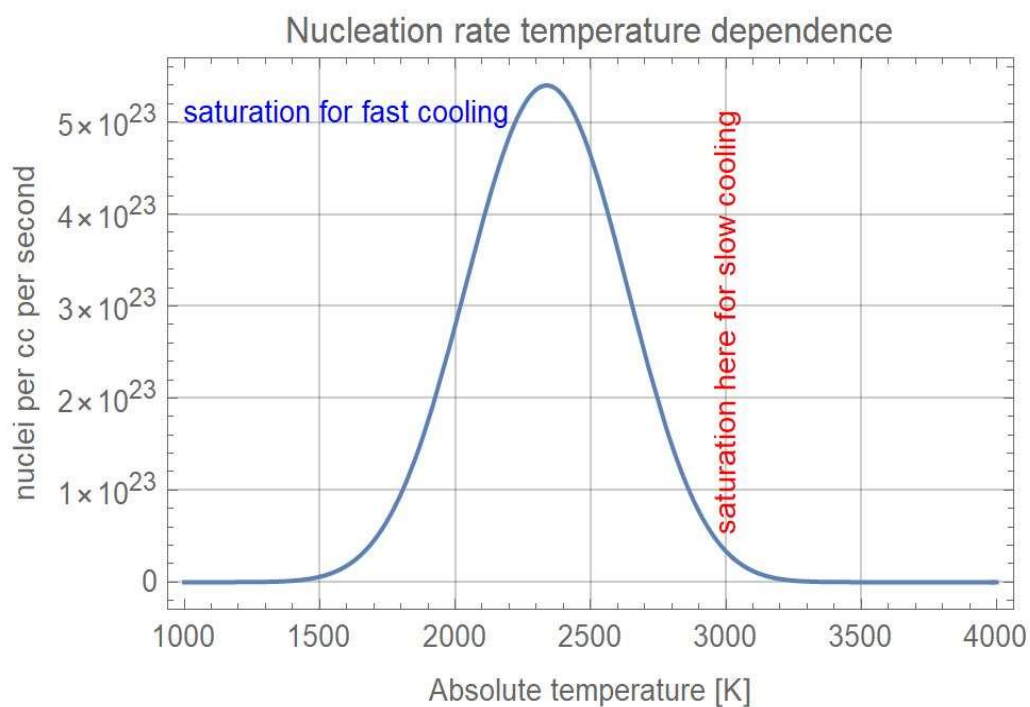


Figure 5.5. Nucleation Rate Temperature Dependence. Using computational and experimentally determined parameters. The saturation text indicates the points at which saturation will take affect for the different cooling rates.

5.3.3. Graphene Sheet Size and Number Density. With insight into how the cooling rates play a part in the nucleation and growth determining the graphene sheet size will be useful to predict as it will relate directly with experimental observation. A value

from the number density can be inferred through its relationship to the number of atoms in each sheet, s , and the number of sheets per cubic centimeter which are s atoms in size, $n(s)$.

This relationship can be written in the following way,

$$\eta_{atoms} = \sum_{s=1}^{s=s_{max}} sn(s). \quad (5.24)$$

This value can be used to normalize the sheet size to make sure the predicted sheet sizes do not grow too large when compared to observational data. Now to determine the mass weighted average, it is logical to consider that a cluster that can grow will be a graphene sheet only if it is above a nominal critical size s_{min} . From current understandings of graphene sheet growth and independent DFT studies, s_{min} will need to be a loop of 5 or 6 atoms as graphene sheets will only grow from a 5- or 6-member loop. This leads to the mass weighted average to be given by,

$$s_{avg} = \frac{\sum_{s=s_{min}}^{s=s_{max}} sn(s)}{\sum_{s=s_{min}}^{s=s_{max}} n(s)} = \frac{\eta_{cryst}}{n_{cryst}}. \quad (5.25)$$

Here η_{cryst} is the number of crystalline atoms per unit volume in the system and n_{cryst} is the number of crystalline clusters per unit volume in the system. With a way to describe the number of crystalline atoms and clusters, the fraction of carbon atoms in crystalline form can be written as follows,

$$f_{cryst} = \frac{\sum_{s=s_{min}}^{s=s_{max}} sn(s)}{\sum_{s=1}^{s=s_{max}} sn(s)} = \frac{\eta_{cryst}}{\eta_{atoms}}. \quad (5.26)$$

Using a hex loop nucleation seed and initial value estimates for the parameters which make up the nucleation and growth model, we determined from our own temperature anneals and assumptions from experiment, we were able to determine a fraction crystalline

for a 3ms cooldown from 3000 to 2000 K of 7%, a mass weighted average of 26 atoms, and a number density of approximately 2.44×10^{20} graphene sheets per unit volume. This is shown in Figure 5.6 which also indicates a strange switching point from a usual exponential curve to an asymptotic style line. This seems to be from switching between fast to slow cooling when our cooling rates get below 10^4 K/s. The switching point is indicative of requiring the addition of saturation effects to study number density, fraction crystalline, and mass weighted average.

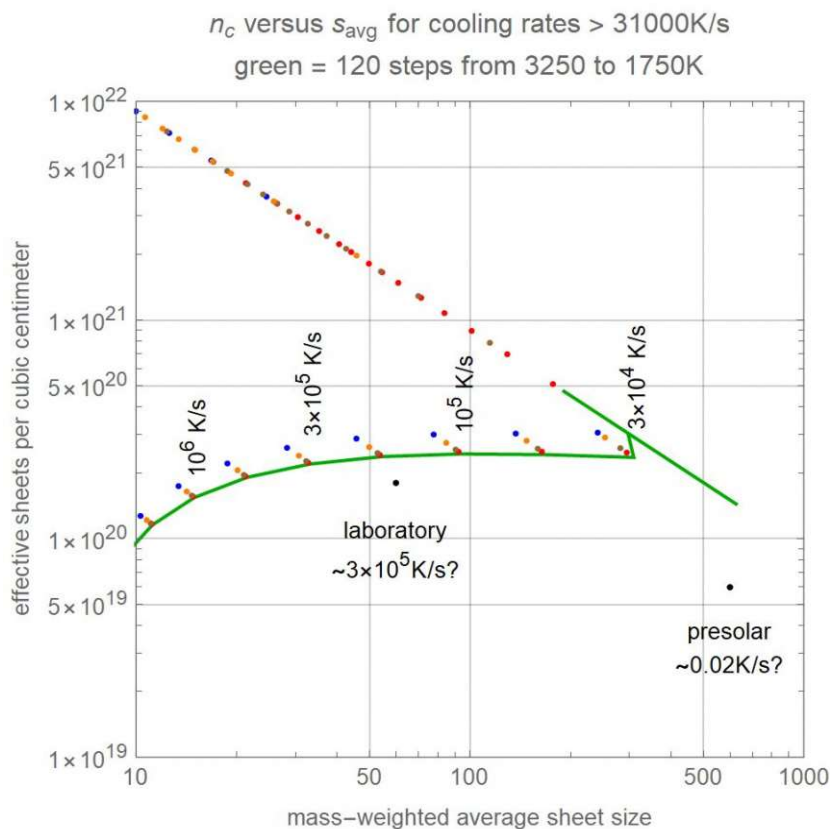


Figure 5.6. Effective Graphene Sheet Density vs. Mass-Weighted Average Sheet Size. The two black dots represent points taken from laboratory and pre-solar cores where the dots above the green line are different number of steps the simulation took at different cooling rates from 10 to 120 steps (indicated by the green line).

The nucleation and growth models that make up the predictions for graphene sheet number density, mass weighted average, and fraction crystalline are dependent on different parameters ($\Delta H_f, \lambda, E_a, T_m$). This allows analyzing the sensitivity of these models to the different parameters. Changing the latent heat of fusion (ΔH_f) and edge energy (λ) gives a large change in the number density of graphene sheets versus mass weighted average. A change in either parameter by less than a factor of two can see changes in many orders of magnitude. This can be explained by the fact that the latent heat of fusion and the edge energy give the Gibb's free energy for nucleation. In changing these two parameters, the Gibb's free energy changes which will change the nucleation peak and supercooling temperature for nucleation.

As the lab-grown and presolar cores were formed in a low-pressure system, setting the latent heat of fusion to the value obtained from temperature anneals at the constant low-pressure of $\sim 10^{-3}$ bars is a useful analysis. When the latent heat of fusion is changed to this value, the values for number density versus mass weighted average change wildly. Multiplying by a factor of two will have the analytical model for fast heating line up perfectly with the observational estimate for the lab grown cores. This agreement can be seen in Figure 5.7. Experimental and other simulations done constrain the value of the latent heat of fusion. The critical temperature for nucleation depends on the ratio between the latent heat and the edge energy penalty, λ . Since this ratio is important, the constraints on ΔH_f will put similar constraints on λ . Cutting one value in half, requires cutting the other value in half.

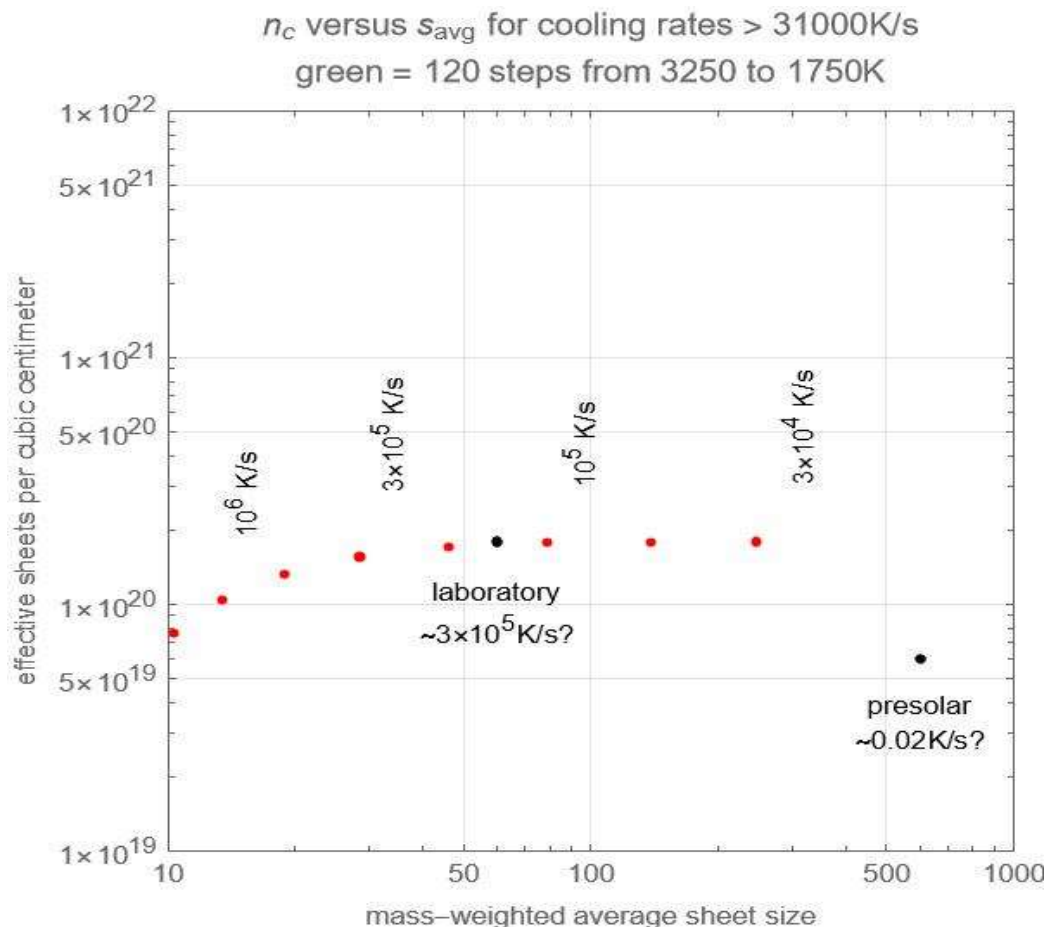


Figure 5.7 Graphene Sheet Density vs. Mass-Weighted Average with Determined ΔH_f . Value determined through constant pressure temperature anneal simulations using LCBOP.

When changing the Arrhenius activation energy (E_a), there is no change in sheet density versus mass weighted average even when increasing this energy penalty by over double. This shows a clear insensitivity to the growth rate for the number density of graphene sheets. This insight along with the insight into the switching point from the sensitivity to the cooling rates requires the consideration of saturation as the system begins to run out of atoms to continue the growth.

5.3.4. Saturation Effect of Slow Cooling. To take into account the effects of saturation, it is first beneficial to look at the distribution when at critical nuclei size of a 6-member loop in this current case for fixed temperature anneals. This is shown in Figure 5.6 and it can be seen that distributions will give straight lines when plotted on a log-log scale. This can be described as follows,

$$\log[n(s)] = \log[n_6] - a(\log[s] - \log[6]). \quad (5.27)$$

The value n_6 is the number of sheets of critical size (6-member loop). From here a representation for $n(s)$ can be determined,

$$n(s) = n_6 \left(\frac{6}{s}\right)^a. \quad (5.28)$$

The number of sheets of critical size, n_6 , will depend purely on the nucleation rate at a given temperature. The power value, a , will depend on the growth rate and the total anneal time.

From here the saturation values, s_{max} , can be determined by setting the sum $\sum_{s=6}^{s=s_{max}} sn(s) = n_1 =$ the initial number of atoms in the system. By setting this sum equal to the initial number of atoms, the saturation values can be determined as this sum is stating that all the free atoms will be used up at any temperature. This sum cannot be solved analytically so a series of sums were run numerically for different temperatures and the outcome can be seen in Figure 5.8. A straight line on a log-log scale shows that the power value, a , is simply -1. This means that the growth rate only affects the total time elapsed. This verifies the insight the analytical model was showing of the overall insensitivity to the growth rate.

If log–log slope of $n[s]$ is -1 , s_{max} depends only on nuclei n_6
 hence the growth rate determines time elapsed only

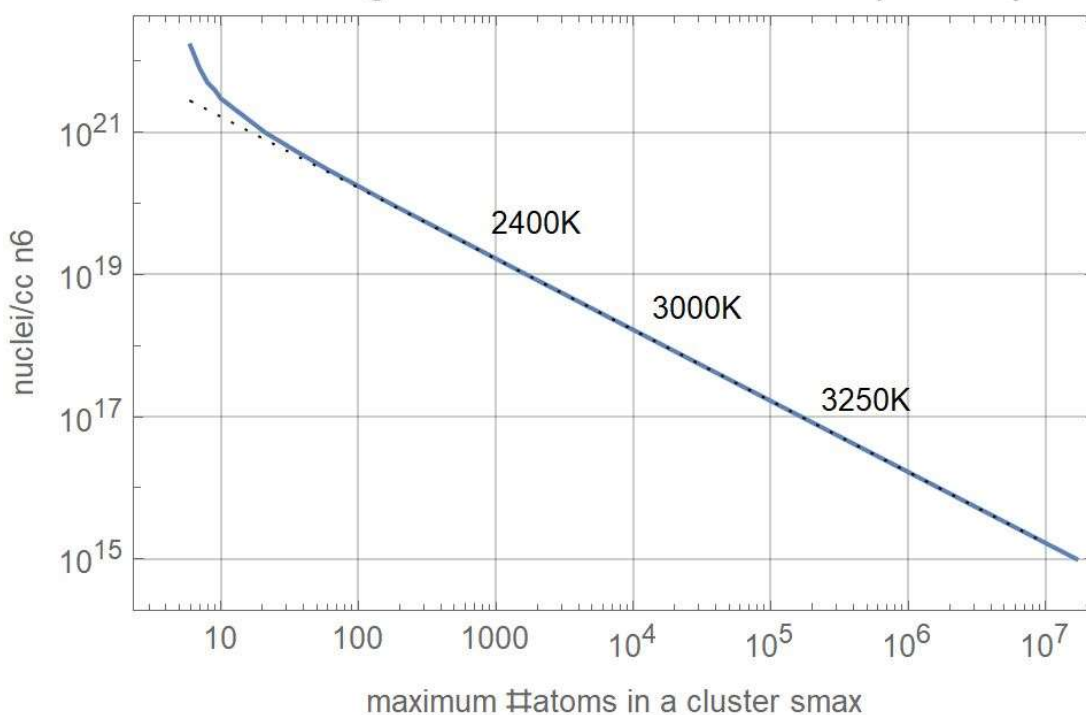


Figure 5.8. Saturation End-Point Statistics. Different temperatures give a straight line before hitting an asymptote at $n_6 \cong \frac{5}{3} \times 10^{22} \frac{1}{s_{max}}$.

The saturation end point is analogous to asymptotic slow cooling which is the same situation happening in the AGB star atmosphere where the pre-solar cores came from. With the saturation effect taken into account for the slow-cooling process, the analytical model for graphene sheet size per cubic centimeter versus mass weighted average can be graphed along with the numerical simulation. Figure 5.9 shows the numerical model lines up perfectly with the switching point for the analytical model. It seems the analytical model was already hinting at the saturation effects which up until now were never considered.

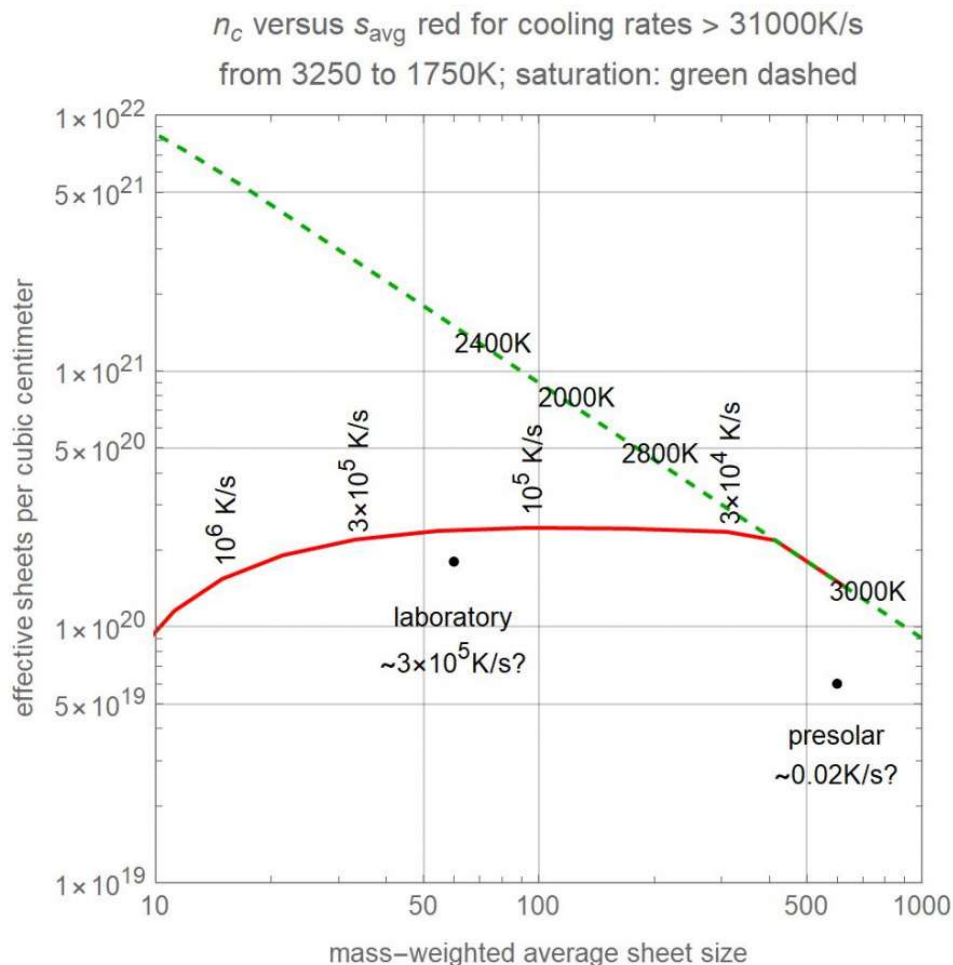


Figure 5.9. Analytical Density vs. Mass Weighted Average with Saturation. Number of graphene sheets per cubic centimeter versus mass weighted average of an “unimpeded saturation” numerical model for slow cooling along with an analytical curve for fast cooling.

5.4. CONCLUSION

The analytical models presented here for 2D nucleation and growth which use experimentally and computationally determined parameters has been able to give insight into and predict physical processes of the solidification of liquid carbon. Analysis into supercooling thresholds for a low-pressure carbon melt was able to be performed. The data shows for low pressure liquid carbon will have undercooling on the order of 50-60% of

carbon's melting temperature which is much greater undercooling than the 30% undercooling of the melting temperature expected to be universal for most metallic elemental liquids that have been studied. The difference in undercooling comes from the fact that graphene sheet growth is much different than most solidification processes. The 3D amorphous liquid solidifies into a 2D solid crystalline structure. This requires a 2D rather than 3D nucleation theory which will be affected by temperature differently.

The nucleation model, in either 3D or 2D, will be dependent on parameters that dictate different criticality in the system. For instance, the critical radius and critical temperature which are reliant on the latent heat of fusion and edge energy ratio. Current knowledge for metallic elemental liquids considers a 3D classical nucleation model which has a different temperature dependence than the 2D case. 3D classical nucleation has its criticality (peak nucleation) temperature dependence be proportional ΔT^2 where the 2D model presented here has criticality proportional to ΔT . The different power dependence of the supercooling threshold will then give chance for deeper supercooling in for the nucleation of a 2D liquid. Looking at the critical temperature and its dependence on ΔH_f and λ , it becomes clear that the ratio of these two values will be key to understanding the nucleation process. Due to the deeper supercooling determined from the analytical models, the growth simulations were misled, and annealing temperatures did not reach the temperature range where growth can occur.

Analyzing graphene sheet number densities, fraction crystalline, and abundance of clusters allowed for direct comparison with experimental data. Observations of lab grown micron sized core/rim spheres have shown larger number densities when compared to similar structures extracted from primitive meteorites. The analytical models shows that

the difference can be physically explained by the drastically different cooling rates when considering a laboratory setting and the stellar atmosphere of an AGB star. In the case of solidification in the star's atmosphere, the carbon will stay at high temperatures for long periods of time. At these high temperatures, the nucleation rate to get a stable nucleus of a critical size to start promoting growth will be very small. The growth rate, however, will be much faster at these high temperatures. Though there will be a small number of nucleation seeds of critical size, the faster rate of growth will allow for growth into larger sheet sizes, but the total number of sheets will be small as the number of atoms to create new nuclei will run out. In the lab case, the rapid cooling will quickly move the system through the nucleation's maximum rate giving many nucleation seeds of critical size to grow from. The growth rate will however be slower at these lower temperatures causing many smaller sized sheets to form but giving an overall higher sheet density.

When comparing the determined values for fraction crystalline, mass-weighted average, and number density of graphene sheets to the experimentally determined values from lab grown cores using values estimated by simulations done separately and experimental assumptions, close agreement with the experimentally observed values was observed. The fraction crystalline and number densities came rather close to the 10% and 1.8×10^{20} determined, but the mass weighted average predicted from these models did fall a bit short to the determined 60 atoms. This showed these models were pointing in the right direction and allowed the ability to analyze the sensitivity of the models to the different parameter values ($\Delta H_f, \lambda, E_a, T_m$) to gauge which parameter values are key to making physical predictions.

A strong sensitivity to the ratio of the latent heat of fusion (ΔH_f) and the edge energy (λ) and the cooling rates was noticed when analyzing the change in graphene sheet density and mass weighted average. On the other hand, a strong insensitivity to the growth rate was determined. The insights into the sensitivity to the cooling rates and insensitivity to the growth rates were strengthened when considering the saturation effects due to slow cooling. Using a numerical approach for the slow cooling saturation which is analogous to an asymptotic low cooling rate. When comparing to our analytical model, it was seen that the numerical model overlapped exactly where this switch occurred. The asymptotic low cooling from the numerical saturation model gives insight into the growth only affecting overall time.

This is also seen when analyzing the graphene sheet number density and mass weighted average analytically by changing the Arrhenius activation energy and seeing a large insensitivity to this energy change. The sensitivity to cooling rates is initially seen from the nucleation peak at the critical temperature. The nucleation peak is also dependent on the Gibb's free energy which is related directly to the latent heat of fusion and edge energy. The dependence on the ratio of ΔH_f and λ strongly effects the nucleation peak and criticality of the nucleation. This means small changes in either value can change the number density of graphene sheets by a large amount as there is a constraint on what ΔH_f or λ can be. The ratio between these two parameters is then key for any nucleation model to make physical predictions for the onset of solidification.

6. CONCLUSIONS

In the work presented in this dissertation, two types of models (atomistic and analytical) were used to test the nucleation and onset of solidification for liquid carbon. The atomistic model used LCBOP with the LAMMPS molecular dynamics simulator to perform “zero-kelvin” conjugate gradient energy minimizations for two types of liquid-like carbon systems: tiled-cube supercells and isolated clusters. The analytical models followed classical models for nucleation and growth, but these models had to be transformed since (unlike other metallic liquids) liquid carbon transitions from a 3D amorphous liquid into a solid matrix filled with 2D crystalline sheets.

The zero kelvin energy minimizations for the tiled-cube systems tested two semi-empirical potentials (LCBOP and EDIP) written to incorporate long-range interactions that are present in carbon were used in the LAMMPS MD simulation software. The loop formation statistics for both potentials had more 5-member loop than 6-member loops, in agreement with independent DFT studies. Pentagonal loop formation in the energy minimizations indicate that pentagons can be seeds for nucleation within the low-density liquid carbon, as suggested by observational work on presolar particles. EDIP gave nonphysical/meta-stable loop formations. The coordination statistics for the LCBOP case saw carbyne sp -coordination and graphene/graphite sp^2 -coordination are the preferred structural coordination after energy minimization with percentages of 42% and 43% respectively. When compared to other work done on carbon coordination there is a much higher percentage of carbyne coordination, but the higher values agree with other observations of low-density carbon. The high percentage of carbyne and graphene/graphite

coordination with prominent pentagonal loop formation could also be evidence of the pentagon-first mechanism of Y-junction carbyne chains.

The nearest neighbor histograms for the tiled-cube case for both LCBOP and EDIP were able to shed light on preferred bond distances for the liquid after energy minimization. LCBOP analysis had a clear gap between 1.7 and 2.2 Å indicate interatomic distances of covalent and metallic bonding. Over half the atoms in the liquid were at interatomic distances resembling metallic bonds, but 48% were within the covalent bond distances. EDIP did not replicate this gap in the nearest neighbor histograms. Overall, when comparing EDIP with LCBOP, the different analysis done could be indications that EDIP for carbon does not perform as well as LCBOP when studying liquid carbon.

For the case of isolated cluster (containerless) systems, the LCBOP semi-empirical was the only potential of any use. The EDIP potential has high dependence on environmental effects which caused errors to occur during the simulations making it impossible to get accurate results from the simulations. Zero kelvin energy minimizations using the Polak-Ribiere version of conjugate gradient optimization was done to find an optimum energy configuration for the atoms. With the relaxed atom positions, n-member loop formation statistics, coordination statistics, density and grain size statistics from different space fill models, and Debye scattering profiles were generated.

The n-member loop formations and coordination statistics showed similar results to the tiled-cube infinite crystal studies. This gives more support that pentagonal 5-member loops are just as likely to be nucleation seeds for liquid carbon. The coordination statistics show a high percentage of carbyne sp-coordination which agrees with previous computational studies of low-density carbon. The presence of 5-member loop formation

and carbyne chains is another indication of the pentagon-first mechanism from Y-junction carbyne chains.

Convex hull, ellipsoid, and Van der Waals space fill models were used with the atom positions to determine the preferred density and grain-size after energy minimization. When determining the density of the containerless setting isolated clusters, the Van der Waals model estimates agreed the most with density observations of lab grown graphite onions. The determination of the grain size looked at the surface to volume ratio. Again, the Van der Waals model comes closest to observed lab-grown cluster sizes in a containerless setting. The more complex and sophisticated determination of volume and surface area of the Van der Waals model gives a more accurate representation of the grain-size than the other two models.

Debye scattering profiles, which can be directly related to x-ray diffraction experiments, had each set seeing a peak at the (100) graphite index. The peak is broad due to the small size of the cluster and low-frequency peaks from the amorphous liquid are present. For a select few sets, the low-frequency peak is negligible or completely absent giving a large peak at the (100) index. This peak with the absence of the (200) interplanar spacing peak indicates the containerless “liquid-like” minimized atom positions are preferring a graphene structure. The wave-like features at the tail of the Debye profile can also be interpreted as a preference for a liquid state in a containerless low-density and pressure setting.

Changing from zero-kelvin energy minimizations to temperature anneals was done with the LCBOP and EDIP semi-empirical potentials for carbon used with the Nosé-Hoover thermostat and occasionally also with the Berendsen barostat. One atom set had a

42-atom graphene sheet embedded into the 100-atom liquid, while the other set was a 100 atom set pre-relaxed at 0K. Simulated temperature anneals were done at temperatures ranging from 1900-3900K over 20 ns time integrations. With the atom positions, the VMD simulator was used to study the growth in both 2D and 3D. The energy values were used to determine the thermodynamic property of the latent heat of fusion and its pressure dependence. Lastly, the combination of the atom energies and their positions over time were used to determine a correlation between the binding energies and the atom coordination.

For the 3D growth case, both potentials used show negligible growth over the 20 ns simulation time. EDIP showed more dissipation than any nucleation or growth to the embedded sheet was consistent for all the temperature anneals studied. When considering lab-grown cores grew at time scales of tenths-of-milliseconds compared to the 20 ns in simulation, the trend of negligible growth in the LCBOP case and dissipation in the EDIP case makes sense. Also, one can consider that the supercooling limit for liquid carbon might be more than the usual 30% for liquid metals. For the range of temperatures studied, a majority are at supercooling temperature of 45% or higher. If the onset of solidification is at a supercooling threshold of 50 or even 60%, the 5-member and 6-member loops may not be stable. The instability of 5- or 6-member loops and the time scale could be the leading factors in why negligible growth, and even dissipation in the EDIP case, was seen for simulations in 3D.

For the 2D growth case, both potentials had noticeable growth of the graphene sheet. Growth increased as the temperature increased which follows our analytical model for growth. The 20 ns to grow 70-80 atom sheets in simulation compared to 60 atoms in

tenths-of-milliseconds in the lab could give insight into a scaling relationship between 2D and 3D growth. Pentagonal loop formation was shown to be prominent for both potentials. In the case of EDIP, there were central pentagons. Growth from a central pentagon will have hexagonal loops nucleate and then grow at an angle and not flat. As the simulations were 2D and forced z-directionality to zero, this type of growth may be showing some non-physical phenomena. LCBOP on the other hand had pentagons form mainly on the edge of sheets. Due to having higher degrees of freedom these pentagons are likely metastable or as independent DFT studies and the zero-kelvin energy minimizations are giving insight to are formed from the “pentagon first” mechanism.

To determine ΔH_f , the difference between the binding energy for graphene and the average binding energy of atoms smaller than that was taken. This was done for simulations which did and did not have a Berendsen barostat used. The average ΔH_f value came to be 1.015 ± 0.078 eV/atom for the high-pressure case using no barostat. For the case holding the pressure at $\sim 10^{-3}$ bars, the average value came out slightly higher at 1.178 ± 0.053 eV/atom. Both cases gave values that fall within the range of uncertainty of experimental and DFT studies done before.

The energy of each atom was taken at a given coordination and used to gain the average energy for each coordination value. For coordination-1 atoms the average binding energy came to be 3.22 ± 0.72 eV, coordination-2 carbon atoms had an average energy of 6.21 ± 0.54 eV, and coordination-3 atoms had their averages come out to be near the expected 7.40 eV. This correlation gives insight into a specific energy state for a carbon atom based on the number of nearest neighbors in the environment. For the low-density liquid carbon temperature anneals a high percentage of sp and sp² coordination which

corresponds to a mixture of carbyne and graphite structuring was determined. This, with information gained from independent DFT studies, helps support that the low-density carbon melt will have either stable or metastable carbyne chains which could produce pentagon nucleation seeds from the Y-junction “pentagon first” mechanism.

2D classical analytical models for nucleation and growth were presented here. Using experimentally and computationally determined parameters with these models have been able to give insight into and give early predictions of physical processes of the solidification of containerless liquid carbon. The data shows the containerless liquid carbon will have undercooling on the order of 50-60% of carbon’s melting temperature which is much greater undercooling than the 30% undercooling expected for most metallic elemental liquids that have been studied. The solidification of the containerless carbon melt is much different than most solidification processes. The 3D amorphous liquid solidifies into a 2D solid crystalline structure. This requires a 2D rather than 3D nucleation theory which is affected by temperature differently.

The nucleation model is dependent on parameters that dictate different criticality in the system. For instance, the critical radius and critical temperature which are reliant on the latent heat of fusion and edge energy. 3D classical nucleation models have a different temperature dependence than the 2D case. The 3D classical nucleation model widely used has its criticality (peak nucleation) temperature dependence be proportional ΔT^2 where the 2D model has criticality proportional to ΔT . The different power dependence of the supercooling threshold will then give chance for deeper supercooling in the nucleation of a 2D liquid. Due to the deeper supercooling determined from the analytical models, the

growth simulations were misled, and annealing temperatures did not reach the temperature range where our models are saying growth can occur.

Observations of lab grown micron sized core/rim spheres have shown larger number densities when compared to similar structures extracted from primitive meteorites. The analytical models showed that the difference can be physically explained by the drastically different cooling rates when considering a laboratory setting and the stellar atmosphere setting. The carbon melt will stay at high temperatures for long periods of time inside the stellar atmosphere. At these high temperatures, the nucleation rate will be very small whereas the growth rate will be much faster. The faster rate of growth will allow for growth into larger sheet sizes, but the small nucleation rate will mean the total number of sheets will be small as the number of atoms to create new nuclei will run out. In the lab case, the rapid cooling will quickly move through the nucleation's peak rate giving many nucleation seeds of critical size. The growth rate will however be slower at these lower temperatures causing many smaller sized sheets to form but giving an overall higher sheet number-density.

The determined values for fraction crystalline, mass-weighted average, and number density of graphene sheets showed very close agreement with the experimentally observed values from lab grown cores. The $\sim 7\%$ fraction crystalline and $\sim 2.3 \times 10^{20}$ number densities came rather close to the 10% and 1.8×10^{20} determined, but the ~ 30 atoms mass weighted average predicted from the analytical model fell a bit short to the determined 60 atoms. This indicates these models are pointing in the right direction and allowed the analysis of the sensitivity of the models to the different parameter values ($\Delta H_f, \lambda, E_a, T_m$) to gauge which parameter values are key to making physical predictions.

A strong sensitivity to the ratio between latent heat of fusion (ΔH_f) and the edge energy (λ) and the cooling rates was noticed when analyzing the change in graphene sheet density and mass weighted average. On the other hand, a strong insensitivity to the growth rate was determined. The insights into the sensitivity to the cooling rates and insensitivity to the growth rates were strengthened when considering the saturation effects due to slow cooling. Using a numerical approach for the slow cooling saturation which is analogous to an asymptotic low cooling rate. When comparing to the analytical model, the numerical model overlaps exactly where the observed switch occurred.

The asymptotic low cooling from the numerical saturation model gives insight into the growth only affecting overall time. This is also seen when analyzing the graphene sheet number density and mass weighted average analytically by changing the Arrhenius activation energy and seeing a large insensitivity to this energy change. The sensitivity to cooling rates is initially seen from the nucleation peak at the critical temperature. The nucleation peak is also dependent on the Gibb's free energy which is related directly to the latent heat of fusion and edge energy. The critical supercooling temperature was also seen to depend directly on the ratio of ΔH_f and λ . This puts constraints on the possible values so if one is changed the other must be changed giving a strong effect on the nucleation peak and criticality of the system. This means the ratio between these two parameters is key and must be a specific value to be able to make physical predictions for the onset of solidification.

The 2D nucleation and growth models show a strong sensitivity to different parameters that make up these analytical models. This work can be extended by looking deeper into the multiparameter space to gauge a stronger understanding of the plausible

values for each of these parameters that make up the analytical models. The numerical model for evolving distributions used here implements free-growth during constant cooldown capped by a full-saturation with infinitesimal cooldown. Effectively, this full-saturation can be thought as a point at an effective fixed-temperature where 100% of the atoms have crystallized. A more sophisticated model for saturation should be considered to gauge accurate predictions of graphene sheet growth. A way to extend this saturation model is by looking at adding a simple version for Ostwald ripening [129,130]. This simple approach of the Ostwald ripening model would involve unimpeded growth to the experimentally determined fraction crystalline. Following this would be a redistribution of the smallest clusters to increase the size of the larger clusters until the observed average crystal size is reached. These additions would get these models closer to making physical predictions for the growth of graphene sheets from a low-pressure carbon liquid.

BIBLIOGRAPHY

1. S. a. J. R. Scandolo, The Centers of Planets: In laboratories and computers, shocked and squeezed matter turns metallic, coughs up diamonds and reveals Earth's white-hot center. *American Scientist* **2003**, *91* (6), p. 516–525.
2. M. Ross, The ice layer in Uranus and Neptune - diamonds in the sky? *Nature* **1981**, *292*, 435–436.
3. S. L. Johnson, P. A. Heimann, A. G. MacPhee, A. Lindenberg, O. R. Monteiro, Z. Chang, R. W. Lee and R. W. Falcone, Bonding in liquid carbon studied by time-resolved x-Ray absorption spectroscopy. *Phys. Rev. Lett.* **2005**, *94*, 057407.
4. A. Hu, Q.-B. Lu, W. W. Duley and M. Rybachuk, Spectroscopic characterization of carbon chains in nanostructured tetrahedral carbon films synthesized by femtosecond pulsed laser deposition. *J. Chem. Phys.* **2007**, *126*, 154705.
5. A. Hu, M. Rybachuk, Q.-B. Lu and W. W. Duley, Direct synthesis of sp-bonded carbon chains on graphite surface by femtosecond laser irradiation. *Appl. Phys. Lett.* **2007**, *91*, 131906.
6. A. Y. Basharin, V. S. Dozhikov, V. T. Dubinchuk, A. V. Kirillin, I. Y. Lysenko and M. A. Turchaninov, Phases formed during rapid quenching of liquid carbon. *Tech. Phys. Lett.* **2009**, 428–431.
7. P. Fraundorf, T. Hundley and M. Lipp, *HAL-02238804* **2019**.
8. Artem Oganov, Structure, Bonding, and Mineralogy of Carbon at Extreme Conditions. *Reviews in Mineralogy and Geochemistry* **2013** *75*: 47-77.
9. J.E. Graebner, Thermal Conductivity of Diamond, *Springer*, **1995**.
10. C .Fron del and U.B. Marvin, Lonsdaleite, A new hexagonal polymorph of diamond. *Nature* **1967**, *214* (5088): 587–589.
11. C .Fron del and U.B. Marvin, Lonsdaleite, A hexagonal polymorph of diamond. *American Mineralogist* **1967**, *52*.
12. Zicheng Pan, Hong Sun, Yi Zhang, and Changfeng Chen, Harder than Diamond: Superior Indentation Strength of Wurtzite BN and Lonsdaleite. *Phys. Rev. Lett.* **2009**, *102*, 055503.
13. P. Fraundorf, G. Fraundorf, T. Bernatowicz, R. Lewis and T. Ming, Stardust in the TEM. *Ultramicroscopy* **1989**, *27* (9): 401-412.

14. G. Balasubramanian, P. Neumann, D. Twitchen, M. Markham, R. Kolesov, N. Mizutani, J. Isoya, J. Achard, J. Beck, J. Tissler, V. Jacques, P. R. Hemmer, F. Jelezko, and J. Wrachtrup, Ultralong spin coherence time in isotopically engineered diamond. *Nat. Mater.* **2009**, *8*, 383–387.
15. P. Chrostoski, H. Sadeghpour, and D. Santamore, Electric Noise Spectra of a Near-Surface Nitrogen-Vacancy Center in Diamond with a Protective Layer, *Phys. Rev. Applied* **2018**, *10*, 064056.
16. P. Chrostoski, B. Barrios, and D. Santamore, Magnetic field noise analyses generated by the interactions between a nitrogen vacancy center diamond and surface and bulk impurities, *Physica B* **2021**, *605*, 412767.
17. P.R. Buseck, S.J. Tsipursky, and R. Hettich, Fullerenes from the Geological Environment. *Science* **1992**, *257* (5067): 215–217.
18. J. Cami, J. Bernard-Salas, E. Peeters, and S. E. Malek, Detection of C60 and C70 in a Young Planetary Nebula. *Science* **2010**, *329* (5996): 1180–1182.
19. S Iijima, Direct observation of the tetrahedral bonding in graphitized carbon black by high resolution electron microscopy. *Journal of Crystal Growth* **1980**, *50* (3): 675–683.
20. A. K. Geim and K. S. Novoselov. The rise of graphene. *Nature Materials* 2007 *6* (3): 183–191.
21. N. M. R. Peres and R. M. Ribeiro, Focus on Graphene. *New Journal of Physics* **2009**, *11* (9): 095002.
22. Zhilin Li, Lianlian Chen, Sheng Meng, Liwei Guo, Jiao Huang, Yu Liu, Wenjun Wang and Xiaolong Chen, Field and temperature dependence of intrinsic diamagnetism in graphene: Theory and experiment. *Phys. Rev. B.* **2015**, *91* (9): 094429.
23. A. Webster, Carbyne as a possible constituent of interstellar dust. *Mon. Not. R. Ast. Soc.* **1980**, *192*, p. 7-9.
24. W. A. Chalifoux and R. R. Tykwinski, Synthesis of extended polyynes: Toward carbyne. *Comptes Rendus Chimie.* **2009**, *12* (3–4): 341.
25. S. L. Johnson, P. A. Heimann, A. G. MacPhee, A. M. Lindenberg, O. R. Monteiro, Z. Chang, R. W. Lee, and R. W. Falcone, Bonding in Liquid Carbon Studied by Time-Resolved X-Ray Absorption Spectroscopy, *Phys. Rev. Lett* **2005**, *94*, 057407.
26. C. B. Cannella and N. Goldman, Carbyne Fiber Synthesis within Evaporating Metallic Liquid Carbon, *J. Phys. Chem. C* **2015**, *119*, 21605–21611.

27. J. M. Zazula, On Graphite Transformations at High Temperature and Pressure Induced By Absorption of the LHC Beam, *LHC-Project-Note-78* **1997**.
28. F.P. Bundy, W.A.Bassett, M.S.Weathers, R.J.Hemley, H.U.Mao, and A.F.Goncharov, The pressure-temperature phase and transformation diagram for carbon; updated through 1994, *Carbon* **1996**, *34* (2): 141-153.
29. G. Zhao, H. F. Mu, D. H. Wang, C. L. Yang, J. K. Wang, J. Y. Song, and Z. C. Shao, Structural and dynamical change of liquid carbon with pressure: ab initio molecular dynamics simulations, *Phys. Scr.* **2013**, *88*, 045601.
30. C.J. Hull, S.L. Raj and R.J. Saykally, The liquid state of carbon, *Chem. Phys. Lett.* **2020**, *749*, 137341.
31. A.L. Horvath, Critical temperature of elements and the periodic system, *Journal of Chemical Education* **1973**, *50* (5): 335.
32. C. J. Wu, J. N. Glosli, G. Galli, and F. H. Ree, Liquid-Liquid Phase Transition in Elemental Carbon: A First-Principles Investigation, *Phys. Rev. Lett.* **2002**, *89*, 135701.
33. W. Hujo, B. S. Jabes, V. K. Rana, C. Chakravarty, and V. Molinero, The Rise and Fall of Anomalies in Tetrahedral Liquids, *J. Stat. Phys.* **2011**, *145*, 293–312.
34. S. Sastry and C. A. Angell, Liquid–liquid phase transition in supercooled silicon, *Nature Mater.* **2003**, *2*, 739–743.
35. M. Beye, F. Sorgenfrei, W. F. Schlotter, W. Wurth, and A. Föhlisch, The liquid-liquid phase transition in silicon revealed by snapshots of valence electrons, *PNAS* **2010**, *107* (30): 16772-16776.
36. T. Morishita, Liquid-Liquid Phase Transitions of Phosphorus via Constant-Pressure First-Principles Molecular Dynamics Simulations, *Phys. Rev. Lett.* **2001**, *87*, 105701.
37. Y. Katayama, T. Mizutani, W. Utsumi, O. Shimomura, M. Yamakata & K. Funakoshi, A first-order liquid–liquid phase transition in phosphorus, *Nature* **2000**, *403*, 170–173.
38. J. C. Palmer, P. H. Poole, F. Sciortino, and P. G. Debenedetti, Advances in Computational Studies of the Liquid–Liquid Transition in Water and Water-Like Models, *Chem. Rev.* **2018**, *118* (18): 9129–9151.

39. R. S. Singh, J. W. Biddle, P. G. Debenedetti, and M. A. Anisimov, Two-state thermodynamics and the possibility of a liquid-liquid phase transition in supercooled TIP4P/2005 water, *J. Chem. Phys.* **2016**, *144*, 144504.
40. C. C. Yang and S. Li, Size-Dependent Temperature-Pressure Phase Diagram of Carbon, *J. Phys. Chem. C* **2008**, *112*, 1423-1426.
41. B. Fegley Jr., Practical Chemical Thermodynamics for Geoscientists, *Academic Press* **2013**.
42. F. Gorrini, M. Cazzanelli, N. Bazzanella, R. Edla, M. Gemmi, V. Cappello, J. David, C. Dorigoni, A. Bifone and A. Miotello, On the thermodynamic path enabling a room-temperature, laser-assisted graphite to nanodiamond transformation, *Sci. Rep.* **2016**, *6*, 35244.
43. P. Fraundorf, G. Fraundorf, T. Bernatowicz, and R. L. Tang Ming, Stardust in the TEM, *Ultramicroscopy* **1989**, *27* (4): 401-411.
44. P. R. Heck, J. Greer, L. Kööp, R. Trappitsch, F. Gyngard, H. Busemann, C. Maden, Janaína N. Ávila, A. M. Davis, and R. Wieler, Lifetimes of interstellar dust from cosmic ray exposure ages of presolar silicon carbide, *PNAS* **2020**, *117* (4): 1884-1889.
45. M. Lugaro, Stardust from Meteorites: An Introduction to Presolar Grains, *World Scientific* **2005**.
46. E. M. Burbidge, G. R. Burbidge, W. A. Fowler, and F. Hoyle, Synthesis of the Elements in Stars, *Rev. Mod. Phys.* **1957**, *29*, 547.
47. T. J. Bernatowicz and E. Zinner, Astrophysical Implications of the Laboratory Study of Presolar Materials, *AIP Conference Proceedings* **1996**, *402*, 450.
48. T. K. Croat, T. Bernatowicz, S. Amari, S. Messenger, and F. J. Stadermann, Structural, chemical, and isotopic microanalytical investigations of graphite from supernovae, *Geo. et Cosmo. Acta* **2003**, *67* (24): 4705-4725.
49. T. K. Croat, F. J. Stadermann, and T. J. Bernatowicz, Presolar Graphite from AGB Stars: Microstructure and s-Process Enrichment, *ApJ* **2005**, *631*, 976.
50. T. J. Bernatowicz, O. W. Akande, T. K. Croat, and R. Cowsik, Constraints on Grain Formation around Carbon Stars from Laboratory Studies of Presolar Graphite, *ApJ* **2005**, *631*, 988.
51. B. Wopenka, Y. C. Xub, E. Zinner, and S. Amari, Murchison presolar carbon grains of different density fractions: A Raman spectroscopic perspective, *Geo. et Cosmo. Acta* **2013**, *106*, 463-489.

52. E. Mandell, Electron beam characterization of carbon nanostructures, *University of Missouri – Rolla ProQuest Dissertations Publishing* **2007**, 3298489.
53. P. Fraundorf and M. Wackenhut, The Core Structure of Presolar Graphite Onions, *ApJ* **2002**, 578, L153.
54. P. Fraundorf, T. Hundley, and M. Lipp, Synthesis of unlayered graphene from carbon droplets: In stars and in the lab, *HAL-02238804* **2019**.
55. H. R. Pruppacher and J. D. Klett, Microphysics of Clouds and Precipitation, *Kluwer* **1997**.
56. R.P. Sear, Nucleation: theory and applications to protein solutions and colloidal suspensions, *J. Phys.: Condens. Matter* **2007** 19 (3): 033101.
57. R.P. Sear, Quantitative Studies of Crystal Nucleation at Constant Supersaturation: Experimental Data and Models, *Cryst Eng Comm.* **2014**, 16 (29): 6506–6522.
58. D. Turnbull and J. C. Fisher, *J. Chem. Phys.* **1949**, 17, 71.
59. S. Auer and D. Frenkel, Numerical prediction of absolute crystallization rates in hard-sphere colloids, *J. Chem. Phys.* **2004**, 120, 3015.
60. D. Duft and T. Leisner, Laboratory evidence for volume-dominated nucleation of ice in supercooled water microdroplets, *Atmos. Chem. Phys.* **2004**, 4, 1997–2000.
61. T. T. H. Nguyen, A. Khan, L. M. Bruce, C. Forbes, R. L. O’Leary, and C. J. Price, The Effect of Ultrasound on the Crystallisation of Paracetamol in the Presence of Structurally Similar Impurities, *Crystals* **2017**, 7(10), 294.
62. W. K. Burton and N. Cabrera, Crystal growth and surface structure. Part I, *Discuss. Faraday Soc.* **1949**, 5, 33-39.
63. N. Cabrera and W. K. Burton, Crystal growth and surface structure. Part II, *Discuss. Faraday Soc.* **1949**, 5, 40-48.
64. M. P. Allen and D. J. Tildesley, Computer Simulation of Liquids, *Oxford University Press*, **1989**.
65. A. V. Shapeev, Moment Tensor Potentials: A Class of Systematically Improvable Interatomic Potentials, *Multiscale Modeling & Simulation* **2016**, 14 (3): 1153–1173.
66. S. J. Plimpton, A. P. Thompson, Computational aspects of many-body potentials, *MRS Bull.* **2012**, 37 (5): 513–521.

67. J. E. Lennard-Jones, On the Determination of Molecular Fields, *Proc. R. Soc. Lond. A.* **1924**, *106* (738): 463–477.
68. P. M. Morse, Diatomic Molecules According to the Wave Mechanics. II. Vibrational Levels, *Physical Review* **1929**, *34*, 57.
69. L. A. Girifalco and V. G. Weizer, Application of the Morse Potential Function to Cubic Metals *Physical Review* **1959**, *114* (3): 687–690.
70. G. C. Abell, Empirical chemical pseudopotential theory of molecular and metallic bonding, *Phys. Rev. B.* **1985**, *31*: 6184.
71. M. Z. Bazant, E. Kaxiras, and J. F. Justo, Environment-dependent interatomic potential for bulk silicon, *Phys. Rev. B.* **1997**, *56* (14): 8542.
72. M. W. Finnis, A simple empirical N-body potential for transition metals, *Philos. Mag. A.* **1984**, *50* (1): 45.
73. A. C. T. van Duin, S. Dasgupta, F. Lorant, and W. A. Goddard III, ReaxFF: A Reactive Force Field for Hydrocarbons, *J. Phys. Chem. A*, **2001**, *105* (41), pp 9396–9409.
74. J. Tersoff, New empirical approach for the structure and energy of covalent systems, *Phys. Rev. B.* **1988**, *37*: 6991.
75. S. Munetoh, T. Motooka, K. Moriguchi, and A. Shintani, Interatomic potential for Si-O systems using Tersoff parameterization. *Computational Materials Science* **2007**, *39* (2), 334–339.
76. J. Tersoff, Empirical interatomic potential for carbon, with applications to amorphous carbon, *Phys. Rev. Lett.* **1988**, *61*:25, 2879-2882.
77. D. W. Brenner, Empirical potential for hydrocarbons for use in simulating the chemical vapor deposition of diamond films, *Phys. Rev. B.* **1990**, *42* (15): 9458–9471.
78. K. Nordlund and J. Keinonen, Formation of Ion Irradiation Induced Small-Scale Defects on Graphite Surfaces, *Phys. Rev. Lett.* **1996**, *77* (4): 0031.
79. J.T. Titantah, and D. Lamoen, sp^3/sp^2 characterization of carbon materials from first-principles calculations: X-ray photoelectron versus high energy electron energy-loss spectroscopy techniques, *Carbon* **2005**, *43*, 1311–1316.

80. G Rajasekaran, R. Kumar and A. Parashar, Tersoff potential with improved accuracy for simulating graphene in molecular dynamics environment, *Mater. Res. Express* **2016**, *3*, 035011.
81. H. A. Posch, Canonical dynamics of the Nosé oscillator: Stability, order, and chaos, *Phys. Rev. A* **1986**, *33* (6): 4253–4265.
82. H. J. C. Berendsen, J. P. M. Postma, W. F. van Gunsteren, A. DiNola, and J. R. Haak, Molecular-Dynamics with Coupling to an External Bath, *J. Chem. Phys.* **1984**, *81* (8): 3684–3690.
83. T. Schlick, Molecular Modeling and Simulation, *Springer* **2002**.
84. K. A. Dill, S. Bromberg, and D. Stigter, Molecular Driving Forces, *Garland Science* **2003**.
85. D. Frenkel and B Smit, Understanding Molecular Simulation, *Academic Press* **2002**.
86. R. H. Swendsen and J. S. Wang, Replica Monte Carlo simulation of spin glasses, *Phys. Rev. Lett.* **1986**, *57*: 2607–2609.
87. A. Warshel, Bicycle-pedal model for the first step in the vision process, *Nature* **1976**, *260* (5553): 679–683.
88. D. E. Shaw *et al.*, Atomic-Level Characterization of the Structural Dynamics of Proteins, *Science* **2010**, *330* (6002): 341–346.
89. A. F. J.H. Los, "Intrinsic long-range bond-order potential for carbon: performance in Monte Carlo simulations of graphitization," *Phys. Rev. B* **68** (2), 24107, 2003.
90. N. A. Marks, Generalizing the environment-dependent interaction potential for carbon, *Phys. Rev. B* **2000**, *63* (3): 0163-1829.
91. J.F. Justo, M.Z. Bazant, E. Kaxiras, V.V. Bulatov, and S. Yip, Interatomic potential for silicon defects and disordered phases, *Phys. Rev. B* **1998**, *58*, 2539.
92. N.A. Marks, D.R. McKenzie, and B.A. Pailthorpe, Molecular-dynamics study of compressive stress generation, *Phys. Rev. B* **1996**, *53*, 4117.
93. P. Mahon, B.A. Pailthorpe, and G.B. Bacskey, A quantum mechanical calculation of interatomic interactions in diamond, *Philos. Mag. B*, **1991**, *63*, 1419.
94. B.A. Pailthorpe, Molecular-dynamics simulations of atomic processes at the low-temperature diamond (111) surface, *J. Appl. Phys.* **1991**, *70*, 543.

95. S. Plimpton, Fast Parallel Algorithms for Short-Range Molecular Dynamics, *J. Comp. Phys* **1995**, *117*, 1-19.
96. E. Polak and G. Ribière, Note on the convergence of conjugate direction methods, *Rev. Française Informat Recherche Opérationelle* **1969**, *3* (1): 35–43.
97. D. S. Franzblau Computation of ring statistics for network models of solids, *Phys. Rev.* **1991**, *44*, 4925.
98. V. L. Deringer and G. Csányi, Machine learning based interatomic potential for amorphous carbon, *Phys. Rev. B* **2017**, *95*, 094203.
99. C. Silva, P. Chrostoski, and P. Fraundorf, DFT study of “unlayered graphene solid” formation, in liquid carbon droplets at low pressures, *MRS Advances* **2021**, *6* (7), 203-208.
100. C. Silva, DFT study of unlayered-graphene solid formation, in carbon droplets condensed in stellar atmospheres, *University of Missouri – Rolla ProQuest Dissertations Publishing* **2021**, 11923.
101. N. A. Marks, N. C. Cooper, D. R. McKenzie, D. G. McCulloch, P. Bath, and S. P. Russo, Comparison of density-functional, tight-binding, and empirical methods for the simulation of amorphous carbon, *Phys. Rev. B* **2002**, *65*, 075411.
102. J. R. Morris, C. Z. Wang, and K. M. Ho, Relationship between structure and conductivity in liquid carbon, *Phys. Rev. B* **1995**, *52*, 4138.
103. R. T. Rockafellar, Convex Analysis, *Princeton Mathematical Series* **1970**, *28*, Princeton University Press.
104. A. Donev, F. H. Stillinger, P. M. Chaikin, and S. Torquato, Unusually Dense Crystal Packings of Ellipsoids, *Phys. Rev. Lett.* **2004**, *92* (25): 255506.
105. C. F. Royse, An introduction to sediment analysis, *Arizona State University Press, Tempe* **1970**, 169.
106. Th. Zingg, Contribution to gravel analysis, *Swiss mineralogical and petrographic notices* **1935**, *15*, 39–140.
107. R. B. Corey and L. Pauling, Molecular models of amino acids, peptides, and proteins, *Rev. Sci. Instrum.* **1953**, *24* (8): 621–627.
108. B. E. Warren, X-ray diffraction, *Courier Corporation* **1990**.
109. P. Debye, X-ray scattering, *Ann. Physik* **1915**, *46*: 809.

110. B. E. Warren, X-ray diffraction in random layer lattices, *Phys. Rev.* **1941**, 59 (9), 693.
111. T. Bernatowicz, R. Cowsik, P. C. Gibbons, K. Lodders, B. F. Jr., S. Amari, and R. S. Lewis, Constraints on stellar grain formation from presolar graphite in the Murchison meteorite, *Astrophysical Journal* **1996**, 472, 760.
112. B. Fultz and J. M. Howe Transmission electron microscopy and diffractometry of materials, *Springer* **2001**.
113. E. Mandell, N. Hunton, and P. Fraundorf, Unlayered graphenes in red-giant starsmoke, *arXiv:cond-mat/0606093v1* **2006**.
114. T. Morishita, Fluctuation formulas in molecular-dynamics simulations with the weak coupling heat bath, *The Journal of Chemical Physics* **2000**, 113 (8): 2976–2982.
115. T. Schlick, Molecular Modeling and Simulation, *Springer* **2002**.
116. H. J. C. Berendsen, J. P. M. Postma, W. F. van Gunsteren, A. DiNola, and J. R. Haak, Molecular dynamics with coupling to an external bath, *J. Chem. Phys.* **1984**, 81(8): 3684-90.
117. W. Humphrey, A. Dalke, and K. Schulten, VMD - Visual Molecular Dynamics, *J. Molec. Graphics* **1996**, 14 (1), 33-38.
118. M. Togaya, Pressure Dependences of the Melting Temperature of Graphite and the Electrical Resistivity of Liquid Carbon, *Phys. Rev. Lett.* **1997**, 79 (13): 0031-9007.
119. F. P. Bundy, Melting of Graphite at Very High Pressure, *J. Chem. Phys.* **1963**, 38, 618.
120. N.D. Orekhov and V.V. Stegailov, Graphite melting: Atomistic kinetics bridges theory and experiment, *Carbon* **2015**, 87, 358–364.
121. J. H. Los, K. V. Zakharchenko, M. I. Katsnelson, and Annalisa Fasolino, Melting temperature of graphene, *Phys. Rev. B* **2015**, 91, 045415.
122. R. Becker and W. Döring, Kinetic treatment of the nucleation in supersaturated vapors, *Ann. Phys. (Leipzig)* **1935**, 24, 719.
123. W. D. Callister and D. G. Rethwisch, *Materials Science and Engineering: An Introduction* **2009**.

124. D. Turnbull, Formation of Crystal Nuclei in Liquid Metals, *J. Appl. Physics*, **1950**, *21*, 1022.
125. D. J. Evans and D. J. Searles, The Fluctuation Theorem, *Advances in Physics* **2002**, *51* (7): 1529-1585.
126. F. Colonna, J. H. Los, A. Fasolino, and E. J. Meijer, Properties of graphite at melting from multilayer thermodynamic integration, *Phys. Rev. B* **2009**, *80*, 134103.
127. K. Kelton and A. L. Greer, Nucleation in condensed matter: applications in materials and biology, *Elsevier* **2010**.
128. R. Kalyanaraman, Nucleation energetics during homogeneous solidification in elemental metallic liquids, *J. Appl. Phys.* **2008**, *104*, 033506.
129. L. Ratke, and P. W. Voorhees, Growth and Coarsening: Ostwald Ripening in Material Processing, *Springer* **2002**, 117-118.
130. A. Baldan, Review Progress in Ostwald ripening theories and their applications to nickel-base superalloys Part I: Ostwald ripening theories, *Journal of Materials Science* **2002**, *37*, 2171-2202.

VITA

Philip Chrostoski obtained his Bachelor of Science in Physics from Southern Illinois University – Edwardsville (SIUE) in 2016. While doing his undergraduate work, he worked as an undergraduate teaching assistant and tutor. His work had him awarded with the SIUE Physics Outstanding Teaching Assistant award for the years of 2015 and 2016. His senior assignment was also awarded with the SIUE Outstanding Senior Assignment award. Philip then moved on to Delaware State University (DSU) where he earned his Master of Science in Physics in 2018. During his time at DSU as a graduate research assistant, Philip was able to graduate with a 4.0 GPA earning him the DSU Graduate Studies and Research Certificate of Academic Excellence. Philip continued his studies by gaining a Dissertation Recruitment Fellowship for the joint Missouri University of Science and Technology (Missouri S&T) and University of Missouri – St. Louis (UMSL) Physics PhD program. Philip received his PhD in Physics jointly by Missouri S&T and UMSL in December 2021.

Philip has published as main author and co-author in multiple conference proceedings and main author in respected peer reviewed journals during his graduate level studies. He also presented work at conferences put together by different societies such as the American Physical Society, Materials Research Society, and the International Society for Optics and Photonics. Philip was also an invited speaker by the Southern Illinois University-Edwardsville physics department to talk about his graduate school studies and research.